Hydraulic performance of brushwood fences for mangrove replantation in the Mekong Delta

Dào, Hoàng Tùng

DOI
10.4233/uuid:0251e545-2b71-4eb9-b755-def24a3e0da6

Publication date
2021

Document Version
Final published version

Citation (APA)
Dào, H. T. (2021). *Hydraulic performance of brushwood fences for mangrove replantation in the Mekong Delta*. [Dissertation (TU Delft), Delft University of Technology]. https://doi.org/10.4233/uuid:0251e545-2b71-4eb9-b755-def24a3e0da6

HYDRAULIC PERFORMANCE OF BRUSHWOOD FENCES FOR MANGROVE REPLANTATION IN THE MEKONG DELTA

HYDRAULIC PERFORMANCE OF BRUSHWOOD FENCES FOR MANGROVE REPLANTATION IN THE MEKONG DELTA

Proefschrift

ter verkrijging van de graad van doctor
aan de Technische Universiteit Delft,
op gezag van de Rector Magnificus Prof.dr.ir. T.H.J.J. van der Hagen,
voorzitter van het College voor Promoties,
in het openbaar te verdedigen op
Donderdag 8 Juli om 12:30 uur

door

Hoàng Tùng DÀO

Master of Coastal Engineering,
Thuy Loi University, Vietnam
geboren te Hanoi, Vietnam.

Dit proefschrift is goedgekeurd door de promotoren

Samenstelling promotiecommissie bestaat uit:

Rector Magnificus	voorzitter
Prof.dr.ir. M.J.F. Stive	Technische Universiteit Delft, promotor
Dr.ir. B. Hofland	Technische Universiteit Delft, copromotor

Onafhankelijke leden:

Prof.dr.ir. S.G.J. Aarninkhof	Technische Universiteit Delft
Prof.dr.ir. W.S.J. Uijttewaal	Technische Universiteit Delft
Prof.dr.ir. A.J.H.M. Reniers	Technische Universiteit Delft
Prof. P.Q. Nhan	Hanoi U. of Natural Resources and Environment, Vietnam

Overig lid:

Dr.ir. T. Suzuki	Min. Overheid Vlaanderen, Belgium

The work presented in this thesis was performed at the Department of Hydraulic Engineering of the Faculty of Civil Engineering and Geosciences of Delft University of Technology. This research was funded by the Vietnam International Education Cooperation Department (VIED), the Ministry of Education and Training.

BỘ GIÁO DỤC VÀ ĐÀO TẠO
CỤC HỢP TÁC QUỐC TẾ
International Cooperation Department

TU Delft Delft University of Technology

Keywords: Brushwood fence, wooden fence, wave reduction, physical model, numerical model, Mekong Delta

Printed by: Hoàng Tùng Dào

Front & Back: Bamboo fences for replantation mangroves in Nha Mat, Bac Lieu, Vietnam. Photo courtesy of Hoàng Tùng Dào, 2016

ISBN 978-94-6366-431-8

An electronic version of this dissertation is available at
http://repository.tudelft.nl/.

For my dear father
and my dear mother

Contents

Summary

In the past decade the role of wooden fences, containing brushwood and branches, in efforts to restoring mangroves has been recognized since a vast reduction of mangroves occurred along the Mekong deltaic coast. This study aims to better understand the hydrodynamic performance related to the possible mechanism of wave reduction and the influence of wave characteristics on wave damping due to wooden fences and, in this study, brushwood fences in particular.

Essentially, the concept of 'volume average' for a porous structure made of irregular brushwood (e.g. bamboo cylinders) has been applied to formulate the friction terms under viscous and turbulent flow, as appearing in the constituent Darcy-Forchheimer equations. The results of model- and full-scale brushwood experiments show that the friction coefficients, as the bulk drag ($\overline{C_D}$) and Forchheimer (β) coefficients, are dependent on the Reynolds number (only $\overline{C_D}$), the space between and the diameters of the cylinders. It is found that the bulk drag coefficient decreases with the increase of Reynolds numbers and is stable at high turbulent flow. The lower values of friction coefficients are also found at larger gaps between cylinders and thus are linked to the low porosity. A distinct difference between homogeneous and inhomogeneous packing of the brushwood was found. Both bulk drag and Forchheimer coefficients at high turbulent flow follow similar trends. Thus, it is possible to link these coefficients by the expression $\overline{C_D} = \beta\pi/2n$.

The numerical application is essential for investigating the wave-fence interaction after obtaining the bulk drag coefficient of wooden fences. The non-hydrostatic free-surface model, SWASH, is firstly validated with the wave data from the 1D physical model conducted at Delft University of Technology. The good agreement results without any model calibration or fine-tuning indicate the crucial role of the bulk drag coefficient in further wave-fence simulations in the SWASH model. The wave-fence interactions for an emerged fence are then investigated with model- and full-scale wooden fences, which are expressed by the reflection, dissipation, and transmission coefficients. A scale effect of reflection and transmission coefficients takes place at the relative fence thickness (B/H_I) that are below 5.5, and decreases with the increase of fence thickness (B) and wave characteristics. Besides fence thickness, the wave reduction over wooden fences is also dependent on incoming wave height (H_I), water depth (d) as expressed by the dimensionless parameters, H_I/d and B/H_I, respectively. These parameters are most in-

fluential aspect for emerged fences. More wave damping is taking place with the increase of B/H_I and for an H_I/d larger than 0.4.

Furthermore, the hypothesis of the relation between the degree of wave non-linearity, quantified by the 'Ursell number', and wooden fence hydrodynamic characteristics has been stated and investigated in the SWASH model. The literature findings from measurement results along the Mekong deltaic coast indicate a large effect of the freeboard of a wooden fence on the transmission coefficient. However, the non-linear wave is damped more effectively, since the higher wave reduction is found at a higher Ursell number. The simulation results also conclude a higher wave reduction at a lower water depth that is related to the emerged condition of wooden fences.

Finally, the combined knowledge of fence resistance and wave-fence interaction was applied in the SWASH model for more realistic bathymetries, as found along the Mekong deltaic coast. The outcomes of the numerical model indicate several conclusions related to the effect of bottom slopes on wave dampings, such as the effects of high- and low-frequency waves, and the total drag force for which the wooden fences have to be designed. The seaward bathymetry is highly effective for the pre-dissipation of incoming waves before the damping by wooden fences. It is noticed that, the gentler a slope, the higher the pre-dissipation at the same water depth. The location of the wooden fence is also important in pre-dissipation, as it is shown that a fence located closer to the land leads to both a higher freeboard and a higher pre-dissipation. Moreover, the bottom slope strongly impacts the damping of both high- and low-frequency waves. The results also open a window for sediment transport through wooden fences, corresponding to high- and low-frequency waves. Furthermore, the total drag force of the wooden fence proportionally decreases with the pre-dissipation, which is strongly influenced by the bottom slopes and the fence locations. Last but not least, the consideration of vegetation behind the wooden fence is simulated. This result concludes that the wooden fence can reduce about half of the wave energy, resist a large amount of wave load for the front-line vegetation and create a favorable zone for restoring mangroves.

Despite an increased understanding introduced in the previous chapters of this thesis, knowledge gaps yet have to be recognized. The most challenging issue to improve the role of wooden fences in restoring mangroves in the Mekong Delta remains the question of the sediment transport through the wooden fence. This research provides some fundamental ideas for further studies.

Samenvatting

In het afgelopen decennium worden rijshouten dammen, houten hekwerken gemaakt van kreupelhout en takkenbosssen, meer en meer gebruikt als middel ter bevordering van het herstel van mangroven, na een enorme afname van de hoeveelheid mangroven langs de Mekong Deltakust. Deze studie heeft tot doel een beter inzicht te verkrijgen op het hydrodynamisch functioneren van deze rijshouten dammen, met name betreffende de golfreducerende werking en de invloed op de golfkarakteristieken.

Het concept van volumemiddeling wordt hier toegepast om de frictie door laminaire en turbulente stroming door het poreuze, onregelmatige kreupelhout (bv. bamboecilinders) te formuleren, zoals in de samengestelde Darcy-Forchheimer vergelijkingen wordt toegepast. Resultaten van de experimenten met kreupelhout op zowel model schaal als op werkelijke schaal, tonen aan dat de frictiecoëfficiënten, zoals de weerstandscoëfficiënt $\overline{C_D}$ en Forchheimer coëfficiënt (β), afhankelijk zijn van het Reynolds-getal (alleen $\overline{C_D}$), van de ruimte tussen én de diameters van de cilinders. Het blijkt dat de weerstandscoëfficiënt afneemt met de toename van Reynolds-getallen en dat deze stabiel is bij een zeer turbulente stroming. De lagere waarden van de weerstandscoëfficiënten zijn ook te vinden bij grotere openingen tussen cilinders en zijn dus gekoppeld aan een lage porositeit. Er werd een duidelijk verschil gevonden tussen een meer homogene en minder homogene stapeling van kreupelhout. Zowel de weerstandscoëfficiënt als Forchheimerweerstand volgen bij zeer turbulente stroming vergelijkbare trends. Het is dan dus mogelijk om deze coëfficiënten te koppelen aan de expressie $\overline{C_D} = \beta\pi/2n$.

Numerieke modellen zijn essentieel voor het onderzoek van de interactie tussen golven en dam (hierna,"golf-dam interacties") nadat de weerstandscoëfficiënt van de afscheidingen is verkregen. Het SWASH model is als eerste gevalideerd met de golfgegevens van het 1D-fysieke modelonderzoek dat werd uitgevoerd op de TU Delft. De goede en overeenkomende resultaten, die zonder modelkalibratie of fine-tuning werden verkregen, duiden op de cruciale rol van de weerstandscoëfficiënt in verdere golf-dam simulaties in het SWASH-model. De golf-dam interacties voor dammen met een boven water uitstekende kruin zijn vervolgens onderzocht op model- en werkelijke schaal, en worden uitgedrukt in de reflectie-, dissipatie- en transmissiecoëfficiënten. Een schaaleffect van reflectie- en transmissiecoëfficiënten vindt plaats bij de relatieve damdikte (B/H_I) die lager is dan 5,5, en welke afneemt met de toename van de damdikte (B) en golfkarakteristieken. Naast de dikte van de dam is de golfreductie over rijshouten dam-

men ook afhankelijk van inkomende golfhoogte (H_I) en waterdiepte (d), zoals uitgedrukt door de dimensieloze parameters, respectievelijk H_I/d en B/H_I. Deze parameters hebben de grootste invloed bij dammen met een boven water uitstekende kruin. Er vindt meer golfdemping plaats met de toename van B/H_I en voor H_I/d groter dan 0,4.

Bovendien is een hypothese over de relatie tussen de mate van niet-lineariteit van golven, gekwantificeerd door het 'Ursell-getal', en de hydrodynamische eigenschappen van de rijshouten dam geformuleerd en onderzocht met toepassing van het SWASH-model. De in de literatuur gesignaleerde resultaten van metingen langs de kust van de Mekong Delta, tonen een groot effect aan van het vrijboord van de rijshouten dam op de transmissiecoëfficiënt. Een niet-lineaire golf wordt echter effectiever gedempt, sinds een hogere golfreductie optreedt bij een hoger Ursell-getal. Uit de simulatieresultaten wordt geconcludeerd dat ook een hogere golfreductie plaatsvindt bij een lagere waterdiepte, welke verband houdt met de kruinhoogte van de boven water uitstekende dam.

Ten slotte werd de informatie over de weerstand van rijshouten dammen en golf-dam interactie toegepast in het SWASH-model om inzicht te verkrijgen in de toepassing van de rijshouten dammen op meer realistische bathymetrieën, zoals langs de kust van Mekong Delta aanwezig zijn. Uit de resultaten van het numerieke model kunnen verschillende conclusies worden getrokken met betrekking tot het effect van bodemhellingen op golfdemping, de effecten op hoog- en laagfrequente golven en de totale weerstandskracht waarvoor de houten hekwerken ontworpen dienen te worden. De zeewaartse bathymetrie is zeer effectief voor de pre-dissipatie van inkomende golven vóór de demping door de houten dam. Waarneembaar is dat hoe flauwer een helling, hoe hoger de pre-dissipatie op dezelfde waterdiepte. De locatie van de rijshouten dam is zodoende belangrijk bij pre-dissipatie. Aangetoond wordt dat een hek dichter bij land tot zowel een hoger vrijboord als tot een hogere pre-dissipatie leidt, van zowel hoog- als laagfrequente golven. De resultaten openen ook een mogelijkheid voor sedimenttransport door de houten dammen, gerelateerd aan de hoog- en laagfrequente golven. Bovendien neemt de totale sleepkracht op de houten dam proportioneel af met de pre-dissipatie, die sterk beïnvloed wordt door de bodemhelling en de locatie van de dam. Als laatste wordt de mogelijkheid van vegetatie achter de dam gesimuleerd. Dit resulteert in de uiteindelijke conclusie dat een rijshouten dam ongeveer de helft van de golfenergie kan verminderen, een groot deel van de golfbelasting op de meest zeewaartse vegetatie kan tegenhouden, en in staat is een gunstige zone te creëren voor het herstel van mangroven.

Ondanks dat in de vorige hoofdstukken van dit proefschrift een toegenomen inzicht werd verkregen, moeten kennislacunes nog steeds worden erkend. Het meest uitdagende vraagstuk voor de verbetering in functie van rijshouten dammen bij het herstel van mangroven in de Mekong Delta, blijft de kwestie van het sedimenttransport door de dammen. Dit onderzoek biedt enige fundamentele hydrodynamische basisconcepten voor verdere studies.

Chapter 1

Introduction

Some stories do not have a clear beginning, middle and end.

Gilda Radner

1

1.1 Research context

Coastal regions, that are historically the most densely populated areas in the world, benefit from access to the ocean, and provide inputs economic development, e.g., in navigation, coastal industries, tourism and recreation. Moreover, human settlements are more concentrated along the coast than elsewhere. However, coastal regions are increasingly threatened by sea-level rise and by coastal hazards, such as more intense storms or hurricanes. The fact is that sea levels have risen about 19 cm in the past century and are estimated to rise at least 28–34 cm in 2100 (Church and White, 2006). Along with sea-level rise, the threat from increased coastal hazards is noticeable with more than 66% of storm and hurricane events occurring in the 21^{st} century (ICCP, 2007). It is obvious that most of the low-lying land is vulnerable if these estimations are taken seriously. Thus, hard solutions to protect coastlines become prevalent in regions that are sensitive to sea-level rise and that depend on economic development. The implementation of coastal protection, including breakwaters, groynes, revetments and sea dikes (Schoonees et al., 2019) brings a certain level of safety for the inland from incidents of flooding during storm surges or increased sedimentation to a particular area.

However, the use of a "hard" solution is a form of human intervention that always interrupts the balance of natural coasts, including the implementation of coastal protection and economic development. In principle, the presence of coastal structures (permanent) changes the hydrodynamics of the coast, such as, wave regimes and flow dynamics (Dugan et al., 2011). The changes of hydrodynamics alter the gradients in sediment transport and depositional processes, leading to an imbalance of sediment and morphology changes, such as acceleration at the updrift side and erosion at the downdrift side of the structure (Schoonees et al., 2019). Additionally, coastal erosions can occur frequently at some coastal area and consequently eradicate local species and ecosystems. Moreover, economic activities occurring near or, especially, at the coast have threatened coastal ecosystems for many years in which industrial wastes, fertilisers and toxic chemicals have been dumped to the sea, leading to the vast destruction of salt marshes and, especially in regard to our study, coastal mangroves.

Mangroves, known as the natural coastal defences, are the coastal vegetation which usually lives in the intertidal areas, e.g., along shorelines, rivers, and estuaries (Duke and Schmitt, 2015). Mangroves mostly grow in tropical and sub-tropical areas where they can withstand the warm temperature (Alongi, 2009, 2008). Mangroves can be recognised by the complex system of their bodies, e.g., roots, stems, and canopies (Figure 1.1), and are able to adapt to the sinusoidal changes of the tidal water levels. In the intertidal zone, mangroves reduce wave energies, and the hydrodynamic loads during the high tide result in a platform which causes an increase in the rate of sediment trapping. Mangrove forests bring about increases in the sediment acceleration on the tidal flat and, consequently, expand the intertidal land (Alongi, 2008; Danielsen et al., 2005; Othman, 1994; Phan et al., 2014). This expansion, therefore, can contribute a vital role to the protection of the shoreline from storms in tropical areas, reduction of the erosion and, thus, the stability along the coastlines (Bouma et al., 2016; Cao et al., 2018).

Figure 1.1: Mangroves and the complex roots, stems and canopies of their system in the Mekong deltaic coasts, Vietnam – Courtesy Hoang Tung Dao in Nha Mat, Bac Lieu, Can Tho, Vietnam

Unfortunately, mangroves are extremely sensitive to surrounding environments, e.g., human activities for economic development, and especially the presence of coastal infrastructures. In the global sea-level rise era, this sensitivity causes mangroves forests to becomes the most vulnerable ecosystems in the world. Due to mangrove clearance for fish-farming and aquaculture, as well as disappearance due to coastal erosion, an estimation of about 2% of mangrove loss annually and about 40% of mangrove will be lost in next two decades (Gilman et al., 2008). Additionally, the arrival of coastal structures, such as sea dikes or sea walls, are considered as a fixed boundary between the mangroves and the intertidal land, which become an obstruction for a natural retreat of the mangroves when the sea level rises. This phenomenon combined with the erosion effect quickly increases the reduction of mangrove width along the coasts. For instance, in the period of 2009 to 2010 severe erosion occurred along about 30 km of coastline resulting in about 8 km of eroded earthen dikes in the Mekong Delta (Duke et al., 2010). Additionally, about 80 km of the total 744 km of the Mekong deltaic coastline was protected to prevent flooding and erosion with most of the structures being revetments and sea dikes, according to a report of SIWRR (2019). As a result, nearly 50% of mangrove forest vanished in the past decade (Christensen et al., 2008; Hong and San, 1993; Joffre and Schmitt, 2010; Nguyen et al., 2013). Figure 1.2 shows a common coastal complex of mangroves in front of sea dikes in the Mekong deltaic coastal areas. There is, in fact, a large reduction of mangroves in front of sea dikes (location 1 and 2) compared to mangroves in the more distant location (top-left, location 3), due to the side effects from coastal structures.

Witnessing the negative impact of hard solutions, many countries in the world obviously still protect the important land by using “grey” infrastructures, a combination of "hard" and "soft" solutions, which can be considered as beneficial solutions for the

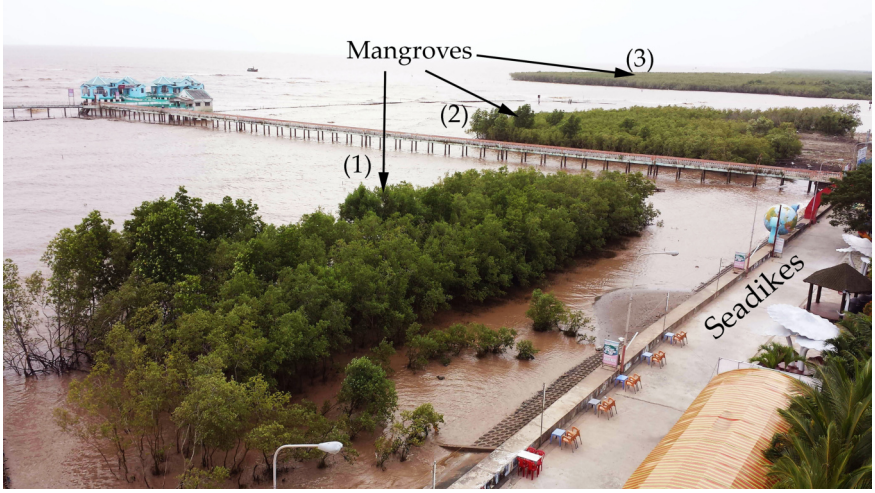

Figure 1.2: An example of coastal protection and mangrove losses in the Mekong deltaic coasts – Courtesy Tri Mai, 2016, Nha Mat, Bac Lieu, Can Tho, Vietnam.

economy (Schoonees et al., 2019). However, the detrimental effects of hard solutions, as mentioned previously, cannot always be avoided. To reduce these effects, civil engineering projects have gradually shifted from hard to soft solutions in the past decade. An example of this trend is the project "Building with Nature" in the Netherlands, which focuses more on safe economic development and sustainable infrastructures. Moreover, a nature-based adaptation can be considered to mitigate and reduce the effects of hard solutions.

Figure 1.3: An example of bamboo fences or soft structures for replantation mangroves in the Mekong deltaic coasts. Brushwood fences were installed in front of mangroves and young mangroves – Courtesy Hoang Tung Dao, 2016, Nha Mat, Bac Lieu, Can Tho, Vietnam.

In the Mekong deltaic situation, soft solutions, i.e., brushwood or bamboo fences applied as an integrating addition to hard structures, these soft solutions are intended to

increase the sedimentation inside the mangroves and, consequently, restore mangrove systems. The bamboo or brushwood structures have been recently applied for restoration planning at erosion sites along the Mekong deltaic coasts (Albers et al., 2013; Schmitt and Albers, 2014; Van Cuong et al., 2015; Winterwerp et al., 2013). The following study aims to provide the requirements for the morpho-dynamic conditions of mangroves in order to establish and guarantee the survival and increase of young mangrove trees. As a result, increased sedimentation inside the mangrove forest and restoration of lost mangroves at eroded sites. In Figure 1.3, an example of using brushwood/bamboo fences for restoring mangroves in the Mekong Delta is presented. The brushwood fences were installed in front of the mangrove belt to reduce wave energy and create a comfort zone for young mangroves grown. This approach is similar to the so-called Dutch "*kwelderwerken*", where a brushwood wall has been used to simulate sedimentation on the tidal flats fronting the marshes (Dijkema, 1983, 1987).

The wooden fence in Figure 1.3 is assembled with mostly natural materials, such as bamboo poles to store smaller bamboo, tree branches, and wooden materials. This specific orientation leads to an important process for wave energy dissipation caused by cylindrical structures forming the structure. The cylinders inside the structure generate drag and friction (resistances) forces on the water motions, resulting in the reduction of wave motions and energy losses. Many studies have carried out the resistance forces against waves and flows of an array of cylinders by mimicking vegetation area, i.e., Anderson and Smith (2014); Hu et al. (2014); Mendez and Losada (2004); Nepf (1999); Ozeren et al. (2013). However, in most case studies the application of the cylinders is in a vertical orientation, which is markedly different from wooden fences. Moreover, an inhomogeneous arrangement forms into a brushwood fence contains a complex configuration which is different from bamboo or tree cylinders and which are not completely smooth and straight. Even though the common resistance coefficient for both array cylinders and wooden fences can be hypothesised as the bulk drag coefficient, the inhomogeneous arrangement of the wooden fences even marks a challenge for indicating this coefficient. The hindered understanding of the resistance leads to a complex mechanism of the reduction waves and flows caused by wooden fences.

In the literature, very few studies investigated the effect of brushwood or bamboo fences on the hydro- and morpho-dynamics for/of mangroves. In the "Mangrove Project Suriname" for coastal management and mangroves rehabilitation (Çete et al., 2018), sediment trapping units using natural materials, i.e., wallaba poles (a local material) and bamboo as filling materials, were constructed similarly to brushwood fences in front of severe erosion areas. Unfortunately, the results of bed level and the sediment changes were only collected by interviews, but apparently the majority of the civilians found the use of brushwood fences justified. In the Mekong Delta, brushwood fences were applied to increase sedimentation and mangrove replantation. Previous studies by Albers et al. (2013); Schmitt and Albers (2014); Van Cuong et al. (2015) measured and observed wave height reductions and sedimentation behind the brushwood fences. Their observation results show a large reduction of wave heights, i.e., about 50% for both studies, and the significant increase of sedimentation inside the wooden fences areas. However, the hy-

draulic processes linked to sediment and nutrient exchanging through wooden fences were insufficiently observed.

In summary, the insufficient knowledge about using soft solutions in coastal management, i.e., brushwood fences, for the restoration of mangroves commands the challenge for a more successful approach. From an engineering perspective, the priority for applying a brushwood fence is to understand the physical mechanism. In fact, the physical processes that induce wave and flow reduction over brushwood/wooden fences have not been addressed, while the observations of sedimentation and bed levels were very limited. Several questions are stated, for instance: (1) What are the fundamental mechanisms of wave and flow reduction linked to sediment and nutrient patterns of brushwood/wooden fences; (2) How do mangroves benefit from soft solutions, i.e., brushwood/wooden fences; (3) What are the considerations for the present plan in the replantation of mangroves using brushwood/wooden fences; and (4) Which improvements can be made from the current plan for a soft solution in combination with original structures. Obviously, there are many other questions that should be stated, but these four questions (former issues) are the fundamental motivations for this study.

1.2 Research questions

The goal of this study is to increase the understanding of the hydraulic functioning of brushwood/wooden fences. Thus, there are scientific knowledge gaps in (1) understanding the mechanism of resistance forces based on the hydraulic force of wooden fences; (2) the fundamental wave-fence interaction, including reflection, dissipation, and transmission processes, for different scales of wooden fences; and (3) understanding the possible relationship between wave characteristics (presented by non-linearity of the wave) and thicknesses of wooden fences. Obviously, these knowledge gaps can be translated into research questions which allow the gaps to be cleared as much as possible.

The main research question can be stated as follows: “How do brushwood/wooden fences respond to hydrodynamic processes and reflect on the changes in survival conditions for mangroves?” In this question, the term hydrodynamic processes refer to the motion of the fluid relating to interaction processes between wave-flow and brushwood /wooden fences. The term “survival conditions” is related to the environment that contains low wave energy and a high rate of sedimentation for the restoration of mangroves. Based on the main research question, several key questions can be stated:

- **Key question 1**: How do brushwood/wooden fences resist the hydrodynamic forces? (Chapter 2)
- **Key question 2**: What are the wave-fence interactions in different scales and models? (Chapter 3)
- **Key question 3**: What are the relations between wooden fence characteristics and wave conditions in the mangrove coast? (Chapter 4)

- **Key question 4**: Which are the design considerations of wooden fence in the real bathymetry that influence on wave damping due to wooden fences? (Chapter 5)

1.3 Research methodology and outline

A variety of methods was used to collect, observe and analyse the data to answer the research questions.

As mentioned in the previous section, even though the wooden fence was mentioned in the literature as a relatively good solution for mangroves, the understanding of the mechanism for wave-flow reduction caused by the wooden fences became more challenging due to lacking knowledge. Therefore, an experiment that applied the hydraulic gradient over a fence sample, assembled with bamboo branches in model- and full-scale under stationary flow, was conducted. Then, the experimental data (hydraulic gradient and flow velocity) was collected and analysed to understand the flow resistance of wooden fences in Chapter 2.

In Chapter 3, a physical model mimicking the coastal mangrove in the Mekong Delta was used to study the wave-fence interaction which used directly from the hydraulic experiments. Then, the data (wave heights) was collected and analysed to indicate the capability of the numerical model in simulating wave-fence interaction processes.

With the confidence of validating the numerical model, the relations between wooden fence characteristics and wave conditions are introduced in Chapter 4. A hypothesis of the relationship between the non-linearity degree of the wave and the thicknesses of wooden fences was proposed by using the results of the numerical model.

The further investigation of the relation between bottom slopes and wave damping due to wooden fences is presented in Chapter 5. The validated numerical model is applied for/to the real-scale of bathymetry and wooden fences on the Mekong deltaic coasts. Finally, Chapter 6 presents the conclusions and recommendations for the application of wooden fences in the Mekong Delta.

1

References

Albers, T., San, D. C., and Schmitt, K. (2013). Shoreline Management Guidelines: Coastal Protection in the Lower Mekong Delta. *Deutsche Gesellschaft für Internationale Zusammenarbeit (GiZ) GmbH Management of Natural Resources in the Coastal Zone of Soc Trang Province*, 1:1–124.

Alongi, D. (2009). *The energetics of mangrove forests*. Springer Science & Business Media.

Alongi, D. M. (2008). Mangrove forests: resilience, protection from tsunamis, and responses to global climate change. *Estuarine, Coastal and Shelf Science*, 76(1):1–13.

Anderson, M. E. and Smith, J. M. (2014). Wave attenuation by flexible, idealized salt marsh vegetation. *Coastal Engineering*, 83:82–92.

Bouma, T. J., Van Belzen, J., Balke, T., Van Dalen, J., Klaassen, P., Hartog, A. M., Callaghan, D. P., Hu, Z., Stive, M. J. F., and Temmerman, S. (2016). Short-term mudflat dynamics drive long-term cyclic salt marsh dynamics. *Limnology and Oceanography*, 61(6):2261–2275.

Cao, H., Zhu, Z., Balke, T., Zhang, L., and Bouma, T. J. (2018). Effects of sediment disturbance regimes on Spartina seedling establishment: Implications for salt marsh creation and restoration. *Limnology and Oceanography*, 63(2):647–659.

Çete, C., Haage, S., Hardwarsing, V., Kalloe, S., and Ma-Ajong, A. (2018). Mangrove Project Suriname.

Christensen, S. M., Tarp, P., and Hjortso, C. N. (2008). Mangrove forest management planning in coastal buffer and conservation zones, Vietnam: A multimethodological approach incorporating multiple stakeholders. *Ocean and Coastal Management*, 51(10):712–726.

Church, J. A. and White, N. J. (2006). A 20th century acceleration in global sea-level rise. *Geophysical research letters*, 33(1).

Danielsen, F., Sorensen, M. K., Olwig, M. F., Selvam, V., Parish, F., Burgess, N. D., Hiraishi, T., Karunagaran, V. M., Rasmussen, M. S., and Hansen, L. B. (2005). The Asian tsunami: a protective role for coastal vegetation. *Science(Washington)*, 310(5748):643.

Dijkema, K. S. (1983). Use and management of mainland salt marshes and Halligen. *Flora and vegetation of the Wadden Sea islands and coastal areas. Balkema, Rotterdam*, pages 302–312.

Dijkema, K. S. (1987). Changes in salt-marsh area in the Netherlands Wadden Sea after 1600. In *Vegetation between land and sea*, pages 42–51. Springer.

Dugan, J. E., Airoldi, L., Chapman, M. G., Walker, S. J., Schlacher, T., Wolanski, E., and McLusky, D. (2011). 8.02-Estuarine and coastal structures: environmental effects, a focus on shore and nearshore structures. *Treatise on estuarine and coastal science*, 8:17–41.

Duke, N., Wilson, N., Mackenzie, J., Nguyen, H. H., and Puller, D. (2010). Assessment of Mangrove Forests, shoreline condition and feasibility for REDD in Kien Giang Province, Vietnam. *Deutsche Gesellschaft für Internationale Zusammenarbeit (GiZ) GmbH Management of Natural Resources in the Coastal Zone of Soc Trang Province*, pages 1–128.

Duke, N. C. and Schmitt, K. (2015). Mangroves: unusual forests at the seas edge. *Tropical forestry handbook. Pancel L., Kohl M.(ed), Springer*, page 24.

Gilman, E. L., Ellison, J., Duke, N. C., and Field, C. (2008). Threats to mangroves from climate change and adaptation options: a review. *Aquatic botany*, 89(2):237–250.

Hong, P. N. and San, H. T. (1993). *Mangroves of Vietnam*, volume 7. Iucn.

Hu, Z., Suzuki, T., Zitman, T., Uittewaal, W., and Stive, M. (2014). Laboratory study on wave dissipation by vegetation in combined current–wave flow. *Coastal Engineering*, 88:131–142.

ICCP (2007). The Fourth Assessment Report. Technical report, The Intergovernmental Panel on Climate Change.

Joffre, O. M. and Schmitt, K. (2010). Community livelihood and patterns of natural resources uses in the shrimp-farm impacted Mekong Delta. *Aquaculture Research*, 41(12):1855–1866.

Mendez, F. J. and Losada, I. J. (2004). An empirical model to estimate the propagation of random breaking and nonbreaking waves over vegetation fields. *Coastal Engineering*, 51(2):103–118.

Nepf, H. M. (1999). Drag, turbulence, and diffusion in flow through emergent vegetation. *Water resources research*, 35(2):479–489.

Nguyen, H.-H., McAlpine, C., Pullar, D., Johansen, K., and Duke, N. C. (2013). The relationship of spatial–temporal changes in fringe mangrove extent and adjacent land-use: Case study of Kien Giang coast, Vietnam. *Ocean & coastal management*, 76:12–22.

Othman, M. A. (1994). Value of mangroves in coastal protection. *Hydrobiologia*, 285(1-3):277–282.

Ozeren, Y., Wren, D. G., and Wu, W. (2013). Experimental investigation of wave attenuation through model and live vegetation. *Journal of Waterway, Port, Coastal, and Ocean Engineering*, 140(5):4014019.

Phan, L. K., van Thiel de Vries, J. S. M., and Stive, M. J. F. (2014). Coastal Mangrove Squeeze in the Mekong Delta. *Journal of Coastal Research*, pages 233–243.

Schmitt, K. and Albers, T. (2014). *Area Coastal Protection and the Use of Bamboo Breakwaters in the Mekong Delta*. Elsevier Inc.

Schoonees, T., Gijón Mancheño, A., Scheres, B., Bouma, T. J., Silva, R., Schlurmann, T., and Schüttrumpf, H. (2019). Hard Structures for Coastal Protection, Towards Greener Designs. *Estuaries and Coasts*, 42(7):1709–1729.

SIWRR (2019). Coastal Protection Status Assessment in the Mekong Delta (in Vietnamese). Technical report, Southern Institute of Water Resources Research.

Van Cuong, C., Brown, S., To, H. H., and Hockings, M. (2015). Using Melaleuca fences as soft coastal engineering for mangrove restoration in Kien Giang, Vietnam. *Ecological Engineering*, 81:256–265.

Winterwerp, J. C., Erftemeijer, P. L. A., Suryadiputra, N., van Eijk, P., and Zhang, L. (2013). Defining Eco-Morphodynamic Requirements for Rehabilitating Eroding Mangrove-Mud Coasts. *Wetlands*, 33(3):515–526.

Chapter 2

Experimental assessment of the flow resistance of coastal wooden fences

Nothing great in the world has ever been accomplished without passion.

Georg Wilhelm Friedrich Hegel

Wooden fences are applied as a nature-based solution to support mangrove restoration along mangrove coasts in general and the Mekong Delta coast in particular. The simple structure uses vertical bamboo poles as a frame to store horizontal bamboo and tree branches (brushwood). Fence resistance is quantitatively determined by the drag coefficient exerted by the fence material on the flow; however, the behaviour of drag is predictable only when the arrangement of the cylinders is homogeneous. Therefore, for more arbitrary arrangements, the Darcy–Forchheimer equations need to be considered. In this study, the law of fluid flow was applied by forcing a constant flow of water through the fence material and measuring the loss of hydraulic pressure over a fence thickness. Fences, mainly using bamboo sticks, were installed with model-scale and full-scale diameters applying two main arrangements, inhomogeneous and staggered. Our empirical findings led to several conclusions. The bulk drag coefficient $\overline{C_D}$ is influenced by the flow regime represented by Reynolds number. The drag coefficient decreases with the increase of the porosity, which strongly depends on fence arrangements. Finally, the Forchheimer coefficients can be linked to the drag coefficient through a related porosity parameter at high turbulent conditions. The staggered arrangement is well-predicted by the Ergun-relations for the Darcy–Forchheimer coefficients when an inhomogeneous arrangement with equal porosity and diameter leads to a large drag and flow resistance.

This chapter was published and chosen as "Editor's choice" in Water 2020, Volume 12, Issue 7, pages 1910–1927. Hoang Tung Dao, Bas Hofland, Marcel J.F. Stive, and Tri Mai (2020). Experimental Assessment of the Flow Resistance of Coastal Wooden Fences.

2.1 Introduction

Brushwood fences have been applied as an alternative porous supportive structure for mangrove restoration along the Mekong Delta coast. By using mainly natural materials, i.e., bamboo and tree branches, fences are considered as a nature-based solution for the protection of shorelines and mangrove forests. This low-cost structure has become more convenient for application on the extremely gentle coast of the Mekong Delta, whereas solid structures were intensively expensive and technically challenging. Installed in front of the mangrove belt to dissipate wave-current energy, the wooden fences in Figure 1 are assembled with a frame and an inner part (Albers et al., 2013; Albers and Von Lieberman, 2011; Schmitt et al., 2013). The frame with vertical bamboo poles has the role of damping a small amount of energy, but also keeping the inner part in place, which consists of bamboo and tree branches in a horizontal orientation (Albers et al., 2013; Albers and Von Lieberman, 2011; Dao et al., 2018; Schmitt and Albers, 2014; Schmitt et al., 2013; Van Cuong et al., 2015). Even though previous studies observed significant wave energy reduction through field measurements (Albers et al., 2013; Schmitt et al., 2013; Van Cuong et al., 2015) and simulation studies (Dao et al., 2018), none of the existing studies concludes that either the frame or the inner part played a significant role in wave energy reduction. Albers and Von Lieberman (2011) tested the effect of porosity on flow energy based on the configuration of bamboo fences. These authors only presented experimental results on vertical bamboo poles, while the vital role of the inner parts was neglected. Thus, it is reasonable to expect that the inner part attenuates energy more effectively than the frame because the structure of the inner part was highly dense compared to the frame as can be seen in Figure 2.1.

Figure 2.1: Wooden fences in the field. The construction includes the frame (two rows of 6–8 cm diameter bamboo poles) and the inner part (a bunch of branches of 1–2 cm diameter bamboo reeds). Reproduced with permission from Dao et al. (2018), Journal of Coastal Research; published by BioOne, 2018.

Many studies about the resistance of array cylinders mimicking vegetation and porous structure have been carried out by applying drag force. In general, the drag force on an array of cylinders is used to achieve the quantitative wave-current energy for a similar structure. The drag coefficient theoretically and empirically expresses the resistance of an array of cylinders, mimicking vegetation. The typical procedure for quantifying the drag coefficient analytically is to employ the Morison equation for drag force on circular

cylinders, as described in Anderson and Smith (2014); Mendez and Losada (2004); Ozeren et al. (2013). Additionally, the drag coefficient is often derived experimentally due to the high complexity of the flow-pole interaction (Hu et al., 2014).

However, for an aggregate of cylinders with irregular diameters, i.e., the inner part (Figure 2.1), the drag coefficient is challenging to obtain theoretically due to the complexity of the analytical process. In particular, the complex flow conditions inside the structure, including laminar and turbulent conditions, are often unpredictable. A feasible way of describing the drag force is to adopt the concept of the volume average (Hsu et al., 2002; Liu et al., 1999), resulting in a type of body force in the form of hydraulic gradient, I. The hydraulic gradient induced by the drag force was applied by Darcy (Darcy, 1856) for viscous flow ($I = au$) and Forchheimer (Forchheimer, 1901) for both viscous and turbulent flow ($I = au + bu^2$), where u (m/s) is flow velocity, a (s/m) and b (s^2/m^2) are commonly known to be the friction terms of the whole body of porous structure (Ergun, 1952; Van Gent, 1996).

For many years, the Darcy–Forchheimer equation has been commonly applied for porous structures made of granular material, e.g., gravel, coarse sand, or fine sand. This equation has been applied for permeable beds of spherical particles (de Castro and Radilla, 2017; Machač et al., 1998; Rao and Chhabra, 1993; Tiu et al., 1997), packed column with granular materials (de Castro and Radilla, 2017; Ergun, 1952), and porous rock structures (Jensen et al., 2014; Van Gent, 1993, 1996). For the inner part of the wooden fence, in particular, bamboo and tree branches with an irregular diameter ranging from 1.0 to 2.0 cm are not completely smooth and straight, leading to high porosity and wide-open spaces between the branches. The Darcy–Forchheimer equation is practically suited to obtaining both drag coefficient and friction factors to obtain friction terms of the inhomogeneous arrangement of cylinders.

In the literature, the characteristics of the material are usually influenced by the drag and the Forchheimer coefficient of porous structures or wooden fences, which include the mean diameter of the material, the density, porosity of the structure, and the distance between cylinders. Additionally, the specific surface area—the total fluid–solid contact area of porous media—is an important parameter commonly applied in physics and chemistry in order to determine the effectiveness of filters (Kantzas et al., 2012). The effects of porosity and specific surface area on the wave energy damping of a vertical cylinder array are described in Arnaud et al. (2017), suggesting that greater specific surface area led to greater wave dissipation.

In this study, the values of the constants in the flow resistance equations that can be used to determine the wave damping potential of brushwood fences at both small and large scale were determined. To achieve this goal, experiments were conducted in which a constant flow was forced through the fence material and characterized in terms of the drag coefficient and the Forchheimer friction coefficient. Several hypotheses are posed and tested: (1) the bulk drag coefficient $\overline{C_D}$ and friction terms are influenced by the flow regime, represented by the Reynolds number; (2) the drag coefficient decreases

with increasing porosity, strongly depending on the type of fence arrangements; (3) the Forchheimer coefficients can be linked to the drag coefficient by means of a parameter under high-turbulence conditions.

The contents are presented in five sections. Section 1 is the introduction. The methodology, which provides descriptions of the formula of resistances, the experiment, and the wooden fences, is presented in Section 2. Sections 3 and 4 present the experimental results and discussion, respectively. Finally, Section 5 presents the conclusions of this study.

2.2 Methodology

2.2.1 Formula of Resistance

he drag coefficient of an immersed cylinder array can be used to derive the drag force on an array of cylinders (Dalrymple et al., 1984):

$$F_D = \frac{1}{2}\rho D N \overline{C_D} u^2 (N/m^3) \tag{2.1}$$

where D (m) and N (m^{-2}) are the diameter and the number of cylinders per volume of a porous media, respectively; u (m/s) is the flow velocity, and ρ (kg/m^3) is the fluid density. The bulk drag coefficient ($\overline{C_D}$) is affected by the cylinder characteristic, such as roughness, cross-sectional shape, flow turbulence and cylinder arrangement, and is a function of cylinder density (Nepf, 1999; Sumer, 2006). The bulk drag coefficient is also affected by flow regimes around the cylinder depending on Reynolds number ($Re = uD/\nu$, with ν (m^2/s) is the kinematic viscosity).

For a single cylinder, the flow is laminar until $Re \approx 200$, even though the laminar vortexes appear relatively early at $Re \approx 40$ (Williamson, 1992). However, at $Re > 200$, the vortices transition to turbulence when the wakes become unstable. Schewe (1983) measured a reduction of the drag coefficient (C_D) of a circular cylinder repetitious from 100 to 1 associated with the increase of Re, up to 10^3. In this stage, the vortexes are generated from laminar conditions at $Re < 40$ (Williamson, 1992) to turbulent conditions at $Re > 200$, causing a rapid decrease of C_D. The C_D value is practically constant at around 1.2 at $10^4 < Re < 10^5$. Within a cylinder array, the vortex shedding starts at Re from 150 to 200 (Nepf, 1999), which might start late, similarly to an isolated cylinder when the porosity of the array increases, leading to a high drag coefficient at this flow stage.

The bulk drag coefficient of array cylinders is also influenced by the wake of the upstream cylinder (Blevins and Scanlan, 1977; Bokaian and Geoola, 1984) and by the distance and position between neighbouring cylinders (Luo et al., 1996). These phenomena are important for randomly arranged cylinders (inhomogeneous arrangement), because spacing and distance are randomly related. When the upstream flow reaches the front cylinders, a velocity reduction in the wake is caused at the downstream cylinder,

resulting in a high value of C_D. Under high turbulence conditions, the wake is completely turbulent, resulting in the occurrence of a vortex that influences the rear cylinder, and also leading to a lower pressure on the downstream cylinders (Luo et al., 1996; Žukauskas, 1972). Depending on the streamwise spacing (s) between cylinders, the vortex at the upstream cylinder may cover the downstream cylinder. For example, a single vortex covers the downstream cylinder when $s/D < 1.0$, while two vortices appear when $3.0 \leq s/D < 6.0$ (Zdravkovich, 1977). Thus, the value of C_D can be set at the nearest to the upstream neighbor when $s/D < 1.0$, with the strongest wake or vortex interaction (Nepf, 1999), while the value of C_D decreases when $s/D > 3.0$ (Bokaian and Geoola, 1984; Nepf, 1999).

In principle, porous media resistance forces can be separated into two types, which are the frictional and pressure forces from drag, and the surface friction of individual elements. For a wooden fence with a high Reynolds number flow, it is assumed that the cylinder roughness is small enough to neglect the friction forces; then the pressure forces are only from drag forces (F_D), and become the main resistance forces. In this case, the Darcy–Forchheimer equation is applicable, and it includes linear and non-linear forces due to the effects of laminar and turbulent friction, respectively:

$$F_D = a\alpha + b\rho|u|\,u \tag{2.2}$$

where a (s/m) and b (s^2/m^2) are the friction factors, which represent viscosity and turbulence dominance, respectively. These factors are related to the porosity (n), the cylinder diameter and the viscosity (v) for a steady-state flow, given as (Ergun, 1952; Van Gent, 1993, 1996):

$$a = \alpha \frac{(1-n)^2}{n^3} \frac{v}{gD^2} \tag{2.3}$$

$$b = \beta \frac{(1-n)}{n^3} \frac{1}{gD} \tag{2.4}$$

where α and β are the dimensionless parameters representing friction terms, which are assumed to change with the geometry of the wooden fence, including bamboo characteristics. The specific surface area—the total fluid–solid contact area of the objects in a porous medium—is sometimes also used to describe the flow resistance, e.g., Arnaud et al. (2017). The specific surface scales with D, and it can be seen above that the laminar and turbulent friction terms have a SSA^2 and SSA dependency, respectively.

From here, two options are available that can describe the fence resistances, i.e., the dimensional friction factor a and b, or the drag coefficient C_D; their relationship is presented in Section 2.3 (Experiment Results). Here, the hydraulic gradient of the incompressible fluid over a fence thickness (Darcy, 1856) is applied to obtain the drag force:

$$I = -\frac{1}{g\rho} \frac{\delta p}{\delta x} \tag{2.5}$$

where I is the pressure gradient generated from pressure difference δp ($kg.m^{-1}.s^{-2}$), over the fence width δx. Thus, two expressions of drag force can be yielded from com-

bining Eq. 2.1 and Eq. 2.2 with Eq. 2.5:

$$I = \frac{DN\overline{C_D}u^2}{2g} \tag{2.6}$$

$$I = au + b|u|u \tag{2.7}$$

2.2.2 Experimental description

The hydraulic gradient experiments were carried out in the Hydraulic Engineering Laboratory at the Delft University of Technology. The bamboo fence was installed inside a square tube with a cross-sectional area A (26 × 26 cm) that was placed inside the outer chamber (Figure 2.2). A hydraulic pump provided a constant flow discharge (Q m/s^3) through the fence with a thickness (B), indicated as a dashed line in Figure 2.2. The hydraulic pump forced the discharge to the open space near the main tube before moving into the fence. The water level was kept above the fence in order to avoid direct pressure on the fence material and to avoid air bubbles inside the pressure sensors (Figure 2.2). Four pressure sensors (with a range of up to 5 PSI) were used to measure pressure head at the top ($H_{p,t}$, pressure sensors PS1 and PS2) and pressure head at the bottom ($H_{p,b}$, pressure sensors PS3 and PS4) of the fence. The difference in pressure head between the top and bottom of the fence can subsequently be estimated by $\Delta H_p = |H_{p,b} - H_{p,t}|$. The Water level Gauges (WGs) were installed to measure the initial water level outside the main tube (H_0) ranging from 0.95 to 1.0 m. This water level was to create the submerged condition for up to the largest thickness of the wooden fence, which was relative to the basin floor for every test.

Fence samples with several thicknesses were tested in each series of flow discharges (see Table 2.1). The tested thicknesses in Table 2.1 were chosen from the smallest (B = 0.30 m) to the largest (B = 0.60 m), depending on the material's thicknesses and based on a minimum thickness of fences in the field corresponding to 0.60 m (Albers et al., 2013; Schmitt et al., 2013). When the fence samples were set, a set of discharge (Q) ranging from 3×10^{-3} to 26×10^{-3} m^3/s was imposed through the material. Those discharge quantities were selected based on the expected flow velocities of waves at real fences, on the order of 0.05 to 2.5 m/s. The discharge per total unit area (pores plus solids), or Darcy velocity (u, m/s) and the pore-flow velocity (u_n, m/s, where n indicates the porosity) were considered to be the characteristic velocities inside porous media (Burcharth and Andersen, 1995; Jensen et al., 2014). These are calculated as

$$u = \frac{Q}{A}; u_n = \frac{u}{n} \tag{2.8}$$

where A (m^2) is the cross-sectional area. Hereafter, a fixed discharge was maintained until a steady H_p was reached. The output of all PSs and WGs was recorded in voltage with a sampling frequency of 100 Hz, which could be converted into the corresponding hydraulic heads (H_p) by means of linear regression relations. The pressure loss over the fence thickness was derived as

$$I_* = \frac{\Delta H_p}{B} \tag{2.9}$$

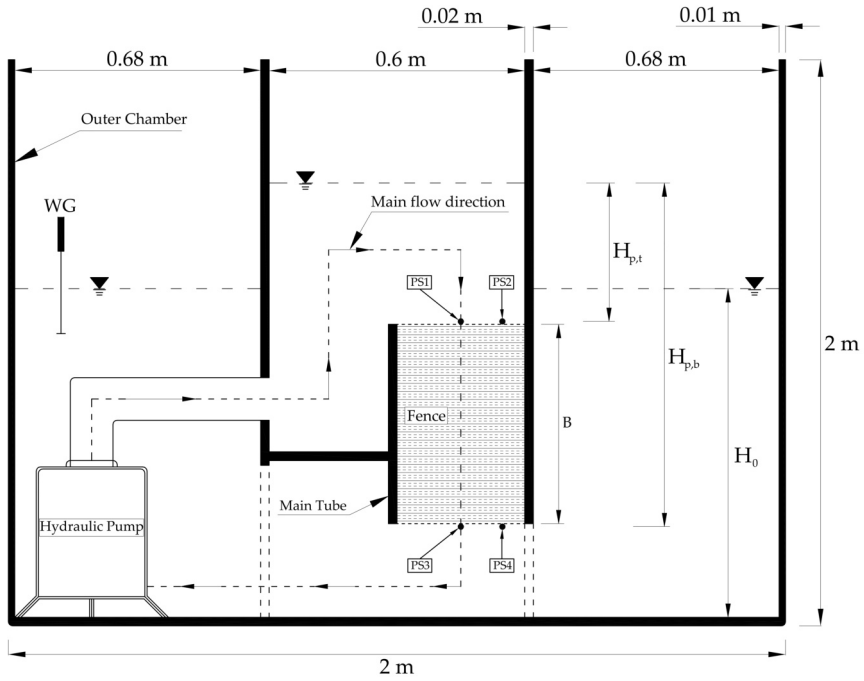

Figure 2.2: Experimental setup. The outer chamber covers the main tube, inside of which fences are installed. During a test, a constant flow discharge, provided by the hydraulic pump, goes through the fence. The different pressures measured by the pressure sensors (PS) are given as ΔH_p.

where the subscription "*" indicates each case described in the next section.

In Figure 2.3, the fence materials were kept in place by two steel meshes with a thickness of 1.0 mm and with one opening per 1.0 cm. To investigate the effect of steel meshes on the measured pressure heads during the experiment, two steel meshes were installed inside the tube without the bamboo fence. Consequently, the different pressure head (ΔH_p) is similar to one of the tests without the meshes and bamboo fence. Therefore, the effects of two steel meshes could be neglected during the tests. Additionally, all pressure devices had been waterproofed by their manufacturer with the exception of the sensors in the centre of the device (Figure 2.3c). When pressure sensors were under water, small bubbles were created by the difference in pressure between atmosphere and the water at the entrance of a pressure sensor (Figure 2.3c), causing extra pressures in the recorded data. By injecting water to fill up the entrance, the pressure sensor could record the required water pressure. This step was only done once for PS3 and PS4 after water surface reached the initial level (H_0), because these devices were always underwater. However, this step was repeated each time the fence thickness was changed for both PS1 and PS2.

The uncertainties related to water level and pressure head measurements were calculated as $\pm\sigma_*$, where σ is the standard deviation and the subscript "*" denotes the spe-

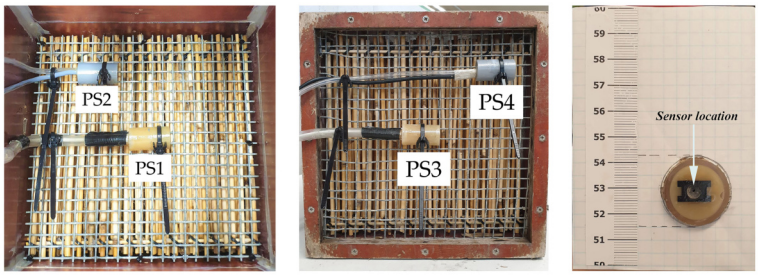

Figure 2.3: Pressure sensors were placed at the top (a), and the bottom (b) of the main tube. The sample of the 5 PSI pressure sensor used in the experiments (c).

cific measurements. Table 2.1 presents the uncertainty of these measurements in two selected flow discharges, Q = 0.0 and Q = 23 10^{-3} m^3/s, for the greatest thickness in each case. It should be noted that the uncertainty of each measurement could be calculated in a time series of data. The output of flow discharge was recorded as a voltage, which was converted into m^3/s on the basis of linear regression relations. The calibration of flow discharge was done once before tests were started.

Table 2.1: The uncertainty related to measurements during tests.

Q (m^3/s)	H_0 (m)	$H_{p,1}$ (m)	$H_{p,2}$ (m)	$H_{p,3}$ (m)	$H_{p,4}$ (m)
0.00	0.98 $\pm 2.10^{-2}$	8.1 10^{-2} $\pm 4.10^{-3}$	7.7 10^{-2} $\pm 6.10^{-3}$	0.63 $\pm 2.10^{-2}$	0.63 $\pm 6.10^{-3}$
23 10^{-3}	0.96 ± 1.5	0.58 $\pm 2.10^{-2}$	0.57 $\pm 3.10^{-2}$	0.65 $\pm 4.10^{-2}$	0.65 $\pm 2.10^{-2}$

For the two discharges included in Table 2.1, the uncertainty in the production of measured pressure head and the water level outside the main tube was acceptable. Additionally, it should be noted that the water level outside decreased because the flow was kept inside the main tube by the fences at high flow discharge.

2.2.3 Wooden fence descriptions

In this study, bamboo poles with a diameter of about 0.02 m were chosen as a large-scale model based on the real fences in the field. The model-scale diameter was chosen by applying a length scale of 5.0 ($L_s = D_p/D_m$), which was available from the supplier. To compare the resistance of small- and real-scale brushwood fences, two sizes of model brushwood were tested using stiff plants, bamboo piles and reeds. Bamboo piles with a mean diameter of 2.1 cm were modelled in real scale, while bamboo reeds of 4.0 mm diameter were employed for small-scale modelling. These natural materials were used as they have natural variations in diameter and length between branches. The small-scale brushwood, used in a wave model with irregular waves, was used to determine possible scale effects. Bamboo diameters were chosen from a statistical analysis of 630 samples

with the small diameter and 100 samples for the larger diameter, representing the model and full scale (prototype), respectively. In Figure 2.4, model diameters are shown to have a wide range of diameters from 2.6 to 4.5 mm in two thirds of the total samples (Figure 2.4a), while the majority of the prototype diameters range from 2.1 to 2.3 cm in half of the total samples (Figure 2.4b). The mean diameter, D_m of 4.0 mm and D_p of 2.1 cm, was chosen to characterize the brushwood diameter. The subscripts "m" and "p" refer to the model and the prototype, respectively.

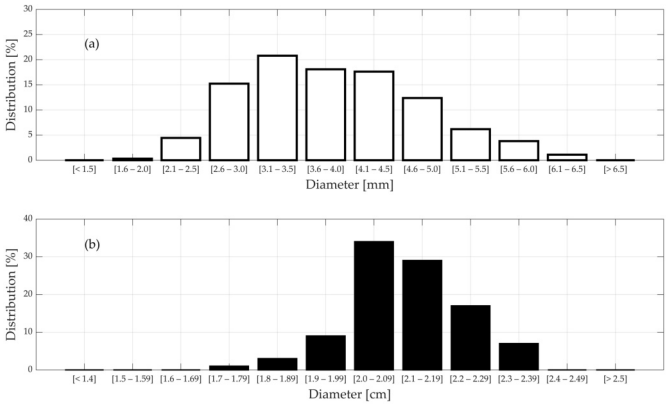

Figure 2.4: Bamboo diameter distribution for (a) model scale and (b) prototype.

Illustrations of inhomogeneous and staggered configurations are presented in Figure 2.5. While the inhomogeneous arrangement is indicated to be a regular arrangement in Figure 2.5a, the diameter and the spanwise spacing had a random character in the experiment. With respect to the inhomogeneous arrangements, mats formed by parallel bamboo reeds connected by steel wire were rolled around a ring in order to generate a large spacing similar to tree branches in the field (Figure 2.5a), while each case of staggered arrangements contains several reeds per layer (Figure 2.5b). Specifically, 14 bamboo sticks of diameter D_m were rolled around a 3.0-cm-diameter ring and connected by steel cables in the inhomogeneous case, resulting in an outer diameter of each branch of about 3.5 cm. The distance between each branch (h_b) was about 3.0 cm. For the staggered arrangement, case 2 and case 3 (Table 2.2) contained 20 and 34 sticks of D_m per layer, respectively. Case 4 and case 5 (Table 2.2) contained 04 and 08 piles of D_p per layer, respectively. The ratio s/D of every configuration corresponds to the smallest distance that generates the highest turbulence conditions. It should be noted that a smaller s/D leads to higher density. However, there is a similar s/D between case 1 and 3, resulting in a different porosity. This difference is caused by the vertical spacing of case 1 ($h_b = 3.0cm$), which is significantly larger than case 3 (roughly 3 mm).

In addition to the s/D, the specific surface area (SSA) can influence the process of porous flow and the adsorption capacity through/of wooden fences. The SSA factor can be calculated by the ratio of the solid interface area to bulk volume of a wooden fence

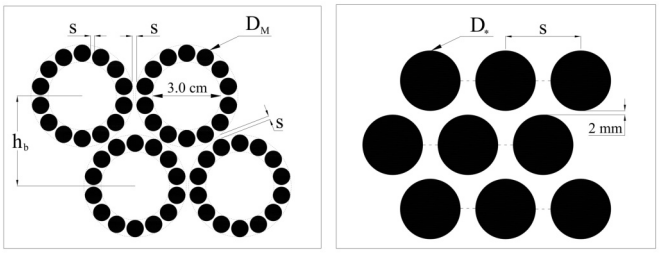

(a) (b)

Figure 2.5: The configuration of the wooden fence using in this study, *i.e.* the Inhomogeneous arrangement (a) and the staggered arrangement (b). The "*" is denoted for the model and real scale, D_m and D_p, respectively.

(Tosco et al., 2013):

$$SSA = \frac{\pi DNL}{Bulkvolume}(1/m) \tag{2.10}$$

where L is the bamboo length, which is equal to 1.0 m, and the bulk volume is 1.0 m^3. The results of density, porosity, SSA, and s_*/D, where the subscript "*" is indicated for each case, are presented in Table 2.2.

Table 2.2: Samples of bamboo fences in experiments.

Case	Sample	Arrangement	D (mm)	B (cm)	Density Sticks/m^2	n	s_*/D (-)	SSA (1/m)
Case 1		Inhomogeneous	4.00	26.5; 34.5; 39.0; 45.5; 58.0	8011	0.90	1.00	100.8
Case 2		Staggered	4.00	25.5; 33.0; 42.0; 53.5	8547	0.89	1.25	107.5
Case 3		Staggered	4.00	29.0; 39.5; 47.0; 54.5	13,077	0.80	1.00	164.5
Case 4		Staggered	20.00	26.5; 36.5; 46.0	603	0.80	1.36	38.1
Case 5		Staggered	20.00	26.5; 36.5; 46.0	1207	0.62	0.23	76.2

2.3 Experiment Results

Firstly, the relationship between the pressure gradient and the Darcy velocity was investigated. The pressure gradient was determined as the ratio of the hydraulic head loss to the fence thickness B. Then, the effect of Reynolds number on the mean flow drag coefficient was derived.

2.3.1 Observation of Pressure Gradient

For flow through a porous medium, pressure losses can be represented by the summation of the contribution of laminar flow and turbulent flow, which are proportional to the velocity (u) and the quadratic velocity (u^2), respectively (Ergun, 1952; Van Gent, 1996). Figure 2.6 presents the relationship between the pressure gradient ($I = \Delta H/B$) and the velocity (u) for all cases. The Darcy–Forchheimer term in Equation (2.7), $au + bu^2$, is a 2^{nd}-order polynomial fit observed at all states of flow.

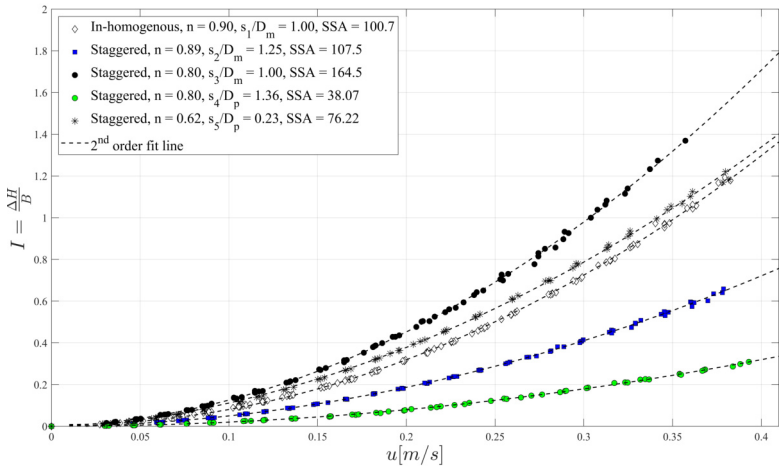

Figure 2.6: Pressure gradient (I) plots against pore velocity (u) of all cases.

As can be observed in Figure 2.6, the hydraulic gradients (I) increase with the increase of velocity in every case. At low velocity, $u < 0.05$ m/s, all of the hydraulic gradients are similar due to the viscosity effect. However, the hydraulic gradient starts to increase quickly when $u > 0.05$ m/s, and the quantity of I_*, again, with the subscript "*" denoting cases 1 to 5, is different between each case. The differences in I between each case increase with increasing velocity, which is to be expected for the quadratic law, due to the different minimum spacing, s_*/D_m and s_*/D_p. For the same porosity of 80%, I_3 (black circles) and I_4 (green circles) are observed to have a large difference. This is the result of the higher capacity of absorption through the SSA_4 of 38.07 (s_4/D_p of 1.36) than SSA_3 of 164.5 (s_3/D_m of 1.00). Additionally, in Figure 2.6, the decrease of s/D leads to larger differences of I during the increase of velocity, especially at the highest velocity. For example, I_5 (black asterisks) is larger than I_2 (blue squares), corresponding to larger

s_2/D_m than s_5/D_p. However, there is an exception for inhomogeneous cases (white diamonds). Even though the spacing s_1/D_m is relatively larger than s_5/D_p (Table 2.2), I_1 is slightly similar to I_5 (black asterisks). The explanation is that the local u of case 5 is much higher than the local u in case 1, but the energy loss of case 1, which is proportional to u^2, is roughly faster than the energy loss in case 5. In particular, the permeability of case 1 increases due to the large space inside each branch, leading to great energy loss as a result of the thickness. However, the specific surface area of case 5 leads to a similar energy loss to that in case 1.

If the hydraulic gradient is divided by u^2, the ratio I/u^2 will represent the turbulence contribution to the flow resistance. If this ratio is constant for varying u, the viscosity contribution to flow resistance is negligible. The relationship of the ratio I/u^2 and the velocity (u) is presented in Figure 2.7. It is shown that the viscosity contribution at the low velocity ($u < 0.1$ m/s) occurs for most of the small-scale cases, while the turbulence contribution for large-scale cases appears at every stage of the flow. For example, I/u^2 decreases slightly in cases 2 (blue squares) and 4 (green circles) at the highest velocity, while the I/u^2 value starts to decrease at velocity $u > 0.1$ m/s in case 1 (white diamonds). The turbulence effects might occur even later in case 3 (black circles) and case 5 (black asterisks).

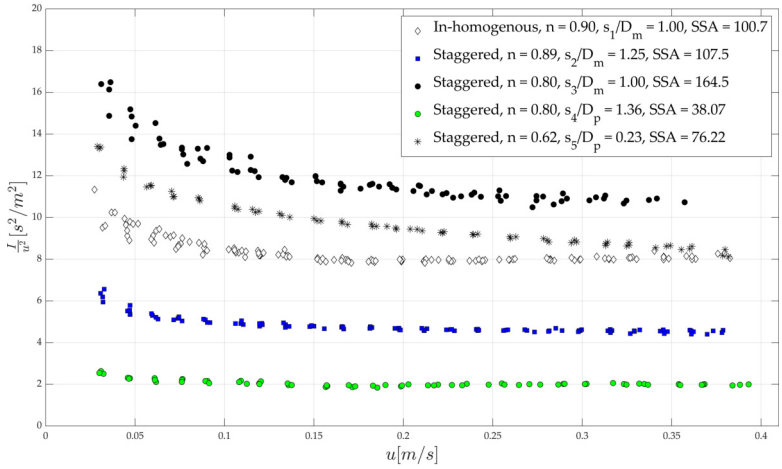

Figure 2.7: Relationship between pressure gradient (I) and (u^2) of all cases.

2.3.2 Effect of Reynolds Number on Drag Coefficient

The effect of flow regime, represented by the influence of the Reynold's number ($Re_n = uD/nv$) on the bulk drag coefficient ($\overline{C_D}$) is obtained from Eq. 2.6 as:

$$\overline{C_D} = \frac{2gI}{DNu_n^2} \tag{2.11}$$

where the hydraulic gradient I (kg/m), gravity acceleration g (m/s^2), pore flow velocity u_n (m/s) and fence characteristics depend on a number of cylinders per m^2 and a bamboo diameter D [m].

Figure 2.8 shows the relationship between the bulk drag coefficient and Reynolds number. As can be observed from Figure 2.8, at $Re_n \approx 150$ the wake of all upstream cylinders causes a decrease in velocity at the downstream cylinders, resulting in a high value of $\overline{C_D}$ of 3.0–6.0 related to the model cases (blue squares, white diamonds and black circles), while $\overline{C_D}$ is 2.5–4.0 in the prototype cases (green circles and black asterisks) at $Re_n \approx 1000$. For the model cases, $\overline{C_D}$ gradually decreases with increasing $Re_n \approx 150$-1000 (under turbulent conditions). For example, $\overline{C_D}$ decreases to 3.87, 2.0, and 1.99 for cases 1, 2 and 3, respectively. For full-scale cases, $\overline{C_D}$ decreases to nearly 1.98 and 0.9 at $Re_n > 1000$ for cases 4 and 5, respectively. Moreover, $\overline{C_D}$ of cases 3 and 4 is overlapping at $Re_n > 1000$, due to a similar porosity of 80%, even though pressure gradients differ greatly between them (Figure 2.6). It should be noted that $\overline{C_D}$ depends on fence characteristics, e.g., diameter, porosity and arrangements. Thus, the hydraulic behaviour of the flow inside the two cases might be similar.

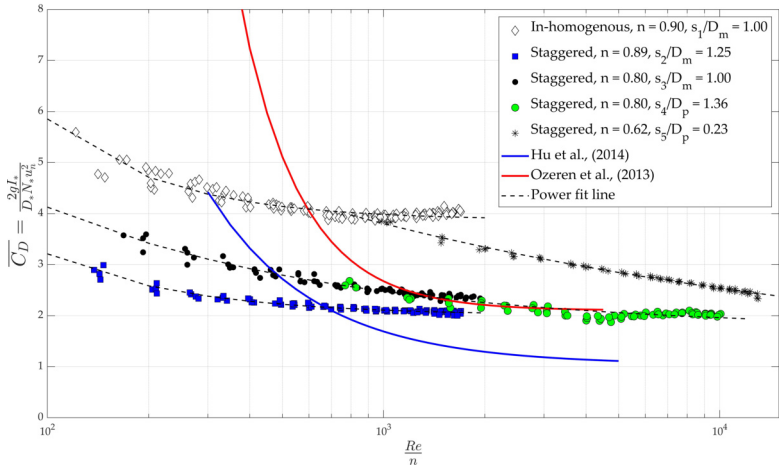

Figure 2.8: Relationship between Reynold number (Re_n) and the bulk of drag coefficient $\overline{C_D}$.

For a large Reynolds number ($Re_n \geq 150$), $\overline{C_D}$ becomes nearly constant, and is a function of fence characteristics, except for case 5. $\overline{C_D}$ decreases due to the increase of incoming velocity through the narrow entrance between cylinders that generates the vortex oscillation of upstream cylinders. For case 1 to case 4, the downstream cylinders are affected within the vortex streets of the upstream cylinders resulting in high $\overline{C_D}$. However, $\overline{C_D}$ of case 5 is relatively small at high Reynolds numbers, which is reflected by its having the strongest vortex interactions at the upstream cylinders. Moreover, $\overline{C_D}$ between the various cases is/are different, which can be explained by the ratio s/D. Lower s/D leads to a higher $\overline{C_D}$. This trend occurs both in the full-scale cases (4 and 5) and in

the model cases (2 and 3). For example, $\overline{C_D}$ (1.98) is higher than $\overline{C_D}$ (0.92) due to the greater ratio of s_4/D_p (1.35) than s_3/D_p (0.23) (see Table 2.2). Moreover, $\overline{C_{D,2}}$ and $\overline{C_{D,3}}$ have a similar value of 2.0, even though s/D is different, with values of 1.25 and 1.0, respectively. Interestingly, the inhomogeneous arrangement exhibits the highest $\overline{C_D}$ value. This may be due to the more widely spaced branches, reducing the shielding effect of upstream branches, as is confirmed by Nepf (1999). Moreover, an explanation for this phenomenon is an extra reduction when the upstream flow goes through the upstream bamboo reeds and reaches the wide space branches.

In this study, the formulation of the power regression between $\overline{C_D}$ and Re_n determined the best fit to be R^2 >0.88. The formulation is separated into inhomogeneous (case 1), staggered with 89% porosity (case 2), staggered with 80% porosity (cases 3, 4), and staggered with 62% porosity (case 5), as presented in Table 2.3.

Table 2.3: $\overline{C_D}$ and Re_n Relation formulas

$\overline{C_D}$ and Re_n relations	Best fit (R^2)	Arrangements	D [mm]	n	s_*/D	Note
$\overline{C_{D,1}} = 3.87 + (\frac{177.2}{Re_n})^{1.23}$	0.88	Inhomogenous	4.00	0.90	1.00	This study
$\overline{C_{D,2}} = 2.00 + (\frac{121.2}{Re_n})^{1.05}$	0.96	Staggered	4.00	0.89	1.25	This study
$\overline{C_{D,3}} = 1.99 + (\frac{326}{Re_n})^{0.65}$	0.96	Staggered	4.00	0.80	1.00	This study
$\overline{C_{D,4}} = 1.98 + (\frac{586}{Re_n})^{1.39}$	0.84	Staggered	20.0	0.80	1.36	This study
$\overline{C_{D,5}} = 0.98 + (\frac{65536}{Re_n})^{0.25}$	0.99	Staggered	20.0	0.62	1.00	This study
$\overline{C_D} = 1.04 + (\frac{730}{Re_n})^{1.37}$	0.72	Staggered	10.0	0.96	unknown	Hu et al. (2014)
$\overline{C_D} = 2.10 + (\frac{793}{Re_n})^{2.39}$	0.89	Staggered	9.40	0.96	unknown	Ozeren et al. (2013)

Figure 2.8 also describes a comparison of the relationship between $\overline{C_D}$ and Re_n to/with the previous studies, i.e., the authors of Hu et al. (2014); Ozeren et al. (2013) found the formula of $\overline{C_D}$ relating to Re_n, from experimental results of wave and current interaction with vegetation. It can be shown from the results of all cases that the $\overline{C_D}$ value follows the same pattern of decreasing at relatively low Re_n and becomes nearly stable at relatively high Re_n. In Figure 2.8, the $\overline{C_D}$ of all is relatively higher than that found in Hu et al. (2014), whereas the $\overline{C_D}$ of cases 2, 3, and 4 are very similar to the value found in Ozeren et al. (2013) at $Re_n > 1000$. This difference could be due to characteristics that are uniquely different between fences and vegetation. The narrow distances between cylinders of wooden fences (s/D) were below 1.3, and this is lower than that of 3.0 (Hu et al., 2014) and 4.7 (Ozeren et al., 2013). As mentioned, the vortex formation around the upstream cylinder less effectively influenced the downstream one when s/D was larger than 3.0, causing a decrease of C_D values (Bokaian and Geoola, 1984; Nepf, 1999). Additionally, the C_D under wave conditions increased as a result of the effects of vortex formation from the upstream and downstream cylinders in a wave cycle that was found

in both previous studies (Hu et al., 2014; Ozeren et al., 2013). When a steady current was involved, the vortices shifted to the downstream side, resulting in a decrease of C_D (Hu et al., 2014).

2.3.3 Forchheimer Coefficient of Fences

As mentioned in the previous section, the pressure gradient (I) is related to the quadratic of Darcy velocity (u^2) at most flow rates (Figure 2.6). It should be noted that stationary flows were applied to every test. Therefore, the turbulence effect could play a major role in the resistance of wooden fences in comparison to the viscosity effect. This means that the linear term (a|u|) in the Forchheimer equation, as shown in Equation (2.7), can be neglected, yielding $I = bu|u|$. The expression of coefficient b is included in parameter β, which should be constant.

From Equations (2.3), (2.4), and (2.7), the full Forchheimer equation is yielded as follows:

$$I = \alpha \frac{(1-n)^2}{n^3} \frac{\nu}{gD^2} u + \beta \frac{(1-n)}{n^3} \frac{1}{gD} u^2 \tag{2.12}$$

Next, two new forms of Eq. 2.12 can be expressed:

$$\frac{I}{u} \frac{gD^2 n^3}{\nu(1-n)^2} = \alpha + \beta \frac{uD}{(1-n)\nu} = f_\nu \tag{2.13}$$

$$\frac{I}{u^2} \frac{gDn^3}{(1-n)} = \alpha \left[\frac{uD}{(1-n)\nu} \right]^{-1} + \beta = f_t \tag{2.14}$$

The left sides of Equation (2.13) and (2.14) are the ratio of pressure losses to the viscous term (viscosity friction, f_ν) and the turbulence term (turbulent friction, f_t).

The dimensionless coefficients α and β for each case were obtained from the linear relation between f_ν and $Re/(1-n)$ supporting in Figure 2.9, with a coefficient of determination of over 90%. The α and β values of each case are also presented in Table 2.4. The experimental results presented in Table 2.4 show the dependency of the β value on the porosity of the fence. The lower the porosity, the lower the β value. For example, β from 1.02 to 1.13 corresponds to $n = 0.8$ and 0.9, while this value is 0.87 at $n = 0.62$ for the same staggered arrangements. However, there is an exception in the case with a similar porosity, illustrated by case 1 (n = 0.90, β = 2.23, SSA = 100.7) and case 2 (n = 0.89, β = 1.13, SSA = 107.5), where the β value of case 1 is about two times larger than case 2, which can be explained by the difference of cylinder configuration.

In Figure 2.10, the power relation between f_t, representing the β value and $Re/(1-n)$, is similar to the power plot between $\overline{C_D}$ and Re_n. As can be seen, the turbulent friction of/in inhomogeneous cases, i.e., f_ν = 2.0, is higher than in the staggered cases, f_t = 1.0 at $Re_n > 1000$. This relationship is also more convergent than the relationship of $\overline{C_D}$, as shown in Figure 2.8, especially for all staggered cases.

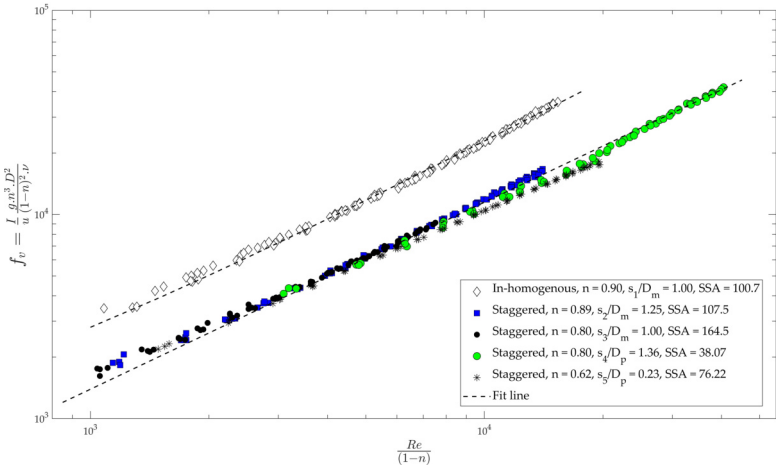

Figure 2.9: Relationship between f_v and $Re/(1-n)$.

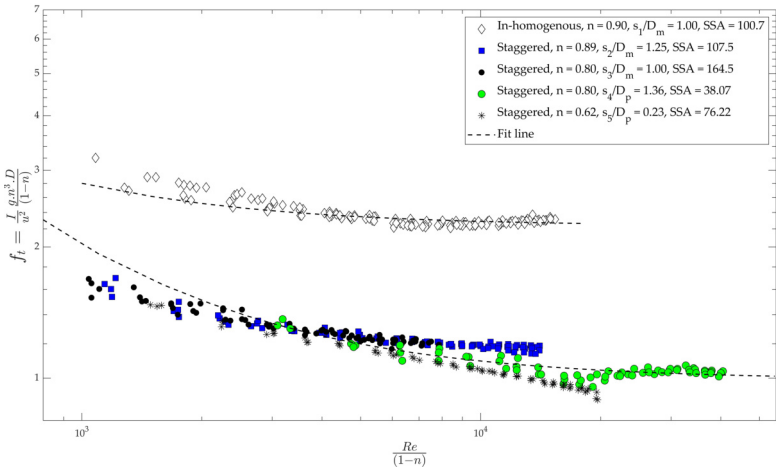

Figure 2.10: Relationship between f_t and $Re/(1-n)$.

2.4 Discussion

2.4.1 Pressure loss between fence widths

It is hypothesized that hydraulic gradients of all thicknesses were quantitatively similar for the same cases. However, an extra pressure loss at the in- and out-flow, especially at high flow rates, might occur when the thickness was increased from thin to thick. The extra pressure loss can be explained by the increase of possible obstructions, leading to flow reduction at the in- and out-flow entrance. However, the extra pressure loss was not easy to obtain from measurements. Therefore, the correction of I between the thinnest

and thickest fences should be dealt with using the following formula:

$$I = \frac{\Delta H_2 - \Delta H_1}{B_1 - B_2} \tag{2.15}$$

where the subscript "1" and "2" represent thinner and thicker thicknesses, respectively. It should be noted that other parameters, such as wall effects, wall friction, and extra thicknesses from steel meshes, could influence the measured signals. Fortunately, these effects play a minor role in a different pressure loss between two thicknesses. Comparison of I between two fence thicknesses and the correction I of cases 3 and 4 are plotted against velocity in Figure 2.11. For case 3, the hydraulic gradient I of two thicknesses was higher than the correction I at $u > 0.2$ m/s. This trend might be caused by the increase of obstruction and possibly random diameter of small-scale bamboo reeds when thicknesses were changed. Interestingly, the correction I and hydraulic gradient of case 4 were closely matched. One possible explanation for this is the stable flow condition at the in- and out-flow entrance.

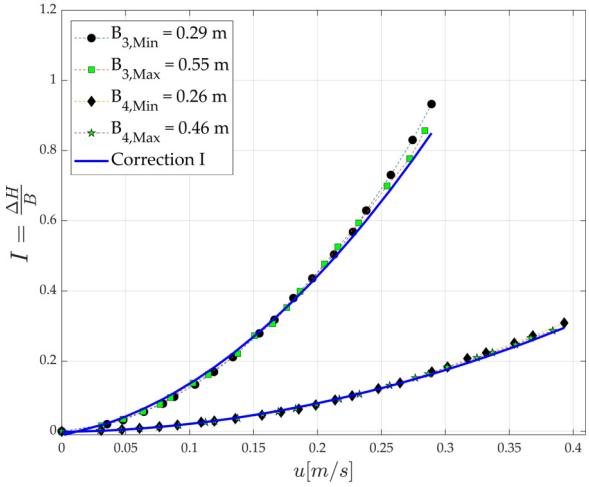

Figure 2.11: Pressure losses difference between two fence width without and with correction.

2.4.2 Effects of Specific Surface Area

The specific surface area (SSA), the total fluid–solid contact area of the wooden fence, is proportional to the diameter of the bamboo cylinders. In Table 2.2, SSA also increases with the decrease of both porosity and s/D, except for inhomogeneous cases. Forchheimer parameters might be based on the specific surface area, which is dependent on the characteristics of the wooden fence, i.e., bamboo diameter and porosity. The laminar and turbulent friction terms have SSA^2 and SSA dependency, as described in Equation (2.13) and (2.14), respectively. The value the laminar and turbulent friction terms is inversely proportional to the order of the SSA magnitudes. The friction terms of cases with

lower SSA, i.e., case 2 (blue square, $SSA = 107.5$) and case 4 (green circle, $SSA = 38.1$), are greater than the high SSA cases in the same scale (see Figure 2.9 and 2.10). However, the high friction of inhomogeneous cases was caused by the extra magnitude of both laminar and turbulent friction due to the wide space inside each branch. Additionally, the laminar drag or friction might cause extra flow reduction even if the flow is in turbulent condition.

For the bulk drag coefficient, the laminar drag caused high flow reduction, resulting in a decrease in the value of $\overline{C_D}$ with the increase of flow rate. Additionally, the phenomena associated with $\overline{C_D}$, i.e., the wake and vortex oscillation of array cylinders, became greater in proportion to SSA, leading to higher values of $\overline{C_D}$ compared to existing studies. However, SSA was less influenced by turbulent drags when $Re_n > 150$ for the model cases. In particular, the values of $\overline{C_D}$ for cases 2 and 3 were similar at 2.0, even when SSA significantly increased from 107.5 to 164.5. For large-scale cases, the SSA effect might still influence the laminar drag at high Re_n, especially in case 4 with a high $SSA = 76.2$.

2.4.3 The link between the drag coefficients and Forchheimer parameter

The experimental results also point out two relationships between resistance factors, the drags $\overline{C_D}$, and the turbulent friction (β) coefficients throughout the two different methods. In particular, the expression of these coefficients can be emphasized by the vortex of upstream cylinders increasing the velocity reduction after each layer of branches and mats under high-turbulence conditions. However, according to Equation (2.14), β values are more related to flow over solid volume ($Re/(1-n)$) than $\overline{C_D}$ values, which are dependent on flows over porous volume (Re/n). This theory can be supported by Figures 2.7 and 2.9, when the β values of all staggered cases were more convergent into a fitted line of power than $\overline{C_D}$. Thus, there should be a link between friction and bulk drag coefficients, because both coefficients were linearly related to a quadratic component of flow velocity. Hereafter, the link between these two coefficients can be described as:

$$\beta = \frac{2n}{\pi}\overline{C_D} \tag{2.16}$$

This link is obtained from combining Equations (2.11) and (2.12). It is noted that porosity is $n = 1 - N\pi D^2/4$. This relationship strongly depends on the porosity of a fence, and can be applied to cylinders, as presented in Table 2.4.

Moreover, Ergun (1952) applied the law of fluid flow through packed columns with small particle materials to introduce the viscosity and kinetic energy losses corresponding to Equation (2.13) and (2.14) in this study. In Ergun's study, the values for parameters α_E and β_E, with the subscript "E" used for Ergun's study, were 150 and 1.75, respectively. Comparing these parameters in Table 2.4, α_E was much smaller than all tested cases due to high laminar friction at the low flow rate. Interestingly, β_E was larger than most of the staggered cases, while it was smaller than the inhomogeneous case. It can be explained that the fence characteristics exert an influence on both in terms of viscosity and turbulent energy loss. For case 1, the wide space inside each branch could cause a velocity

reduction from upstream and downstream cylinders resulting in an additional energy loss into both the friction factors a and b. In contrast, most of the staggered cases have a narrow space between cylinders, leading to lower friction compared to Ergun's study. Additionally, the specific surface area in Ergun's study might have less effect on laminar and turbulent friction than this study due to different material characteristics.

Table 2.4: α and β value from linear relation between f_v and $Re/(1-n)$.

Case	D (mm)	n	α_*	β_*	α	β	$\overline{C_D}$
1	4.0	0.90	566.6	2.234	566.6	2.234	3.89
2	4.0	0.89	569.7	1.128			1.98
3	4.0	0.80	580.9	1.125	978.1	0.912	2.00
4	20.0	0.80	516.3	1.016			1.99
5	20.0	0.62	1444	0.872			0.92

The subscript "*" is denoted for each case.

2.5 Conclusion

The resistance of a brushwood fence was investigated by determining the hydraulic gradient over a fence sample under stationary flow. Fence samples were installed in both a model- and a full-scale setup with inhomogeneous and staggered configurations with porosities varying from 62% to about 90%. Based on the experiment results, the $\overline{C_D}$ was strongly dependent on the fence's porosity, the minimum spacing ratio (s/D) configuration, and the Reynolds number. With decreasing $\overline{C_D}$ values, Re_n increased from 150 to 1000 and became stable at $Re_n > 1000$. The $\overline{C_D}$ value also decreased when the ratio s/D was reduced in all full-scale tests. This ratio can be linked directly to the fence's porosity, which supports the result indicating that the lowest porosity case has the smallest $\overline{C_D}$.

Moreover, the application of Forchheimer's law and Ergun's equation resulted in a new method for predicting the bulk drag coefficient of wooden fences in the field. Specifically, the inner parts of a wooden fence in the field also have an inhomogeneous arrangement (Albers et al., 2013; Albers and Von Lieberman, 2011; Dao et al., 2018; Schmitt and Albers, 2014; Schmitt et al., 2013; Van Cuong et al., 2015), usually causing the space between bamboo branches to be irregular. It is reasonable for the flow reduction to be somewhat unpredictable. The specific surface area can explain the resistance of wooden fences, which is dependent on diameter and porosity. Greater SSA leads to higher laminar drag, which causes higher $\overline{C_D}$ at the low Re_n. The decrease of SSA also leads to an increase in both the laminar and turbulent friction of wooden fences. Our findings for $\overline{C_D}$ and β of inhomogeneous cases may predict this coefficient in the field. The link between $\overline{C_D}$ and the Forchheimer coefficient β for a high Reynolds flow was determined to be $\overline{C_D} = \beta\pi/2n$.

References

Albers, T., San, D. C., and Schmitt, K. (2013). Shoreline Management Guidelines: Coastal Protection in the Lower Mekong Delta. *Deutsche Gesellschaft für Internationale Zusammenarbeit (GiZ) GmbH Management of Natural Resources in the Coastal Zone of Soc Trang Province*, 1:1–124.

Albers, T. and Von Lieberman, N. (2011). Current and Erosion Modelling Survey. *Deutsche Gesellschaft für Internationale Zusammenarbeit (GiZ) GmbH Management of Natural Resources in the Coastal Zone of Soc Trang Province*, 1:1–61.

Anderson, M. E. and Smith, J. M. (2014). Wave attenuation by flexible, idealized salt marsh vegetation. *Coastal Engineering*, 83:82–92.

Arnaud, G., Rey, V., Touboul, J., Sous, D., Molin, B., and Gouaud, F. (2017). Wave propagation through dense vertical cylinder arrays: Interference process and specific surface effects on damping. *Applied Ocean Research*, 65:229–237.

Blevins, R. D. and Scanlan, R. H. (1977). Flow-induced vibration.

Bokaian, A. and Geoola, F. (1984). Wake-induced galloping of two interfering circular cylinders. *Journal of Fluid Mechanics*, 146:383–415.

Burcharth, H. F. and Andersen, O. K. (1995). On the one-dimensional steady and unsteady porous flow equations. *Coastal engineering*, 24(3-4):233–257.

Dalrymple, R. A., Kirby, J. T., and Hwang, P. A. (1984). Wave diffraction due to areas of energy dissipation. *Journal of Waterway, Port, Coastal, and Ocean Engineering*, 110(1):67–79.

Dao, T., Stive, M. J. F., Hofland, B., and Mai, T. (2018). Wave Damping due to Wooden Fences along Mangrove Coasts. *Journal of Coastal Research*, 34:1317–1327.

Darcy, H. P. G. (1856). *Les Fontaines publiques de la ville de Dijon. Exposition et application des principes à suivre et des formules à employer dans les questions de distribution d'eau, etc.* Victor Dalamont, Paris.

de Castro, A. R. and Radilla, G. (2017). Non-Darcian flow of shear-thinning fluids through packed beads: Experiments and predictions using Forchheimer's law and Ergun's equation. *Advances in water resources*, 100:35–47.

Ergun, S. (1952). Fluid flow through packed columns. *Chem. Eng. Prog.*, 48:89–94.

Forchheimer, P. (1901). Wasserbewegung durch boden. *Z. Ver. Deutsch, Ing.*, 45:1782–1788.

Hsu, T.-J., Sakakiyama, T., and Liu, P. L.-F. (2002). A numerical model for wave motions and turbulence flows in front of a composite breakwater. *Coastal Engineering*, 46(1):25–50.

Hu, Z., Suzuki, T., Zitman, T., Uittewaal, W., and Stive, M. (2014). Laboratory study on wave dissipation by vegetation in combined current–wave flow. *Coastal Engineering*, 88:131–142.

Jensen, B., Gjøl, N., and Damgaard, E. (2014). Investigations on the porous media equations and resistance coef fi cients for coastal structures. *Coastal Engineering*, 84:56–72.

Kantzas, A., Bryan, J., and Taheri, S. (2012). Fundamentals of fluid flow in porous media. *Pore size distribution*, 1:1–336.

Liu, P. L.-F., Lin, P., Chang, K.-A., and Sakakiyama, T. (1999). Numerical modeling of wave interaction with porous structures. *Journal of waterway, port, coastal, and ocean engineering*, 125(6):322–330.

Luo, S. C., Gan, T. L., and Chew, Y. T. (1996). Uniform flow past one (or two in tandem) finite length circular cylinder (s). *Journal of wind engineering and industrial aerodynamics*, 59(1):69–93.

Machač, I., Cakl, J., Comiti, J., and Sabiri, N. E. (1998). Flow of non-Newtonian fluids through fixed beds of particles: comparison of two models. *Chemical Engineering and Processing: Process Intensification*, 37(2):169–176.

Mendez, F. J. and Losada, I. J. (2004). An empirical model to estimate the propagation of random breaking and nonbreaking waves over vegetation fields. *Coastal Engineering*, 51(2):103–118.

Nepf, H. M. (1999). Drag, turbulence, and diffusion in flow through emergent vegetation. *Water resources research*, 35(2):479–489.

Ozeren, Y., Wren, D. G., and Wu, W. (2013). Experimental investigation of wave attenuation through model and live vegetation. *Journal of Waterway, Port, Coastal, and Ocean Engineering*, 140(5):4014019.

Rao, P. T. and Chhabra, R. P. (1993). Viscous non-Newtonian flow in packed beds: Effects of column walls and particle size distribution. *Powder technology*, 77(2):171–176.

Schewe, G. (1983). On the force fluctuations acting on a circular cylinder in crossflow from subcritical up to transcritical Reynolds numbers. *Journal of fluid mechanics*, 133:265–285.

Schmitt, K. and Albers, T. (2014). *Area Coastal Protection and the Use of Bamboo Breakwaters in the Mekong Delta*. Elsevier Inc.

Schmitt, K., Albers, T., Pham, T. T., and Dinh, S. C. (2013). Site-specific and integrated adaptation to climate change in the coastal mangrove zone of Soc Trang Province, Viet Nam. *Journal of Coastal Conservation*, 17(3):545–558.

Sumer, B. M. (2006). *Hydrodynamics around cylindrical strucures*, volume 26. World scientific, Singapore.

Tiu, C., Zhou, J. Z. Q., Nicolae, G., Fang, T., and Chhabra, R. P. (1997). Flow of viscoelastic polymer solutions in mixed beds of particles. *The Canadian Journal of Chemical Engineering*, 75(5):843–850.

Tosco, T., Marchisio, D. L., Lince, F., and Sethi, R. (2013). Extension of the Darcy–Forchheimer law for shear-thinning fluids and validation via pore-scale flow simulations. *Transport in porous media*, 96(1):1–20.

Van Cuong, C., Brown, S., To, H. H., and Hockings, M. (2015). Using Melaleuca fences as soft coastal engineering for mangrove restoration in Kien Giang, Vietnam. *Ecological Engineering*, 81:256–265.

Van Gent, M. R. A. (1993). Stationary and oscillatory flow through coarse porous media. *Communications on hydraulic and geotechnical engineering, No. 1993-09*, 1:1–139.

Van Gent, M. R. A. (1996). Wave interaction with permeable coastal structures. In *International Journal of Rock Mechanics and Mining Sciences and Geomechanics Abstracts*, volume 6, page 277A.

Williamson, C. H. K. (1992). The natural and forced formation of spot-like 'vortex dislocations' in the transition of a wake. *Journal of Fluid Mechanics*, 243:393–441.

Zdravkovich, M. M. (1977). Review of flow interference between two circular cylinders in various arrangements. *Journal of fluids engineering*, 99(4):618–633.

Žukauskas, A. (1972). Heat transfer from tubes in crossflow. In *Advances in heat transfer*, volume 8, pages 93–160. Elsevier.

Chapter 3

Numerical and small-scale physical modelling of wave transmission by wooden fences

Ever tried. Ever failed. No matter. Try Again. Fail again. Fail better.

Samuel Beckett

Mangrove forests, that often act as natural coastal defences, enormously suffered due to ongoing climate change and human disturbances. Thus, it is necessary to have a countermeasure to mitigate the loss of mangroves. Wooden fences are becoming a viable nature-based solution to protect vulnerable replanted mangrove forests. However, the wooden fence's hydraulic characteristics are not yet fully understood due to the complication of branches arrangement. In the present study, a small-scale fence was tested in a wave flume to investigate the wave damping by wooden fences. The inner branches of the fence had the same inhomogeneous arrangement as used in earlier flow-resistance experiments. The physical model results indicate that the wooden fence is highly effective on wave transmission and that the effectiveness in wave reduction depends on the relative fence thickness, B/H_I. To understand the scale effect on wave transmission further, the numerical model SWASH was used with the laboratory wave data. By applying the prior experiments' drag coefficient on steady flow, the un-calibrated numerical model gave a good agreement with the wave model results, with a root-mean-square error for the total transmitted wave heights of 4.7%. After validation, potential scale effects for small scale tests were determined from scaling simulations at both full scales and the applied 1:5 model scale. These simulations were performed for a fence porosity of 0.81, and different fence thicknesses to

This chapter was published in Journal of Coastal and Hydraulic Structures, Volume 1 (2021). The published paper had some changes compared to this version based on the reviewer comments. Hoang Tung Dao, Bas Hofland, Tomohiro Suzuki, Marcel J.F. Stive, Tri Mai and Le Xuan Tuan (2021). Numerical and small-scale physical modelling of wave transmission by wooden fences

understand scale effects between model- and full-scale. Both wave reflection and transmission at model-scale are about 5% higher than full-scale results due to the increased drag coefficient and viscous effects. The effects of fence thickness and porosity were the same in large and small scale, and much larger than the error due to scale effects. Hence testing fence efficiency at physical small scale is still regarded as a useful tool, together with numerical modelling.

3.1 Introduction

Mangrove forests play a significant role as coastal defences by dissipating wave and current energies and opening an opportunity to protect the shore and expand the coast (Del Valle et al., 2020). However, mangrove forests have been facing severe degradation due to ongoing climate change and human disturbances. Hard structures, such as sea dikes and revetments, are usually used to protect the coastlines from erosion under design conditions but ultimately may cause mangrove squeeze (Phan, van Thiel de Vries and Stive, 2014). To restore mangroves nature-based solutions, such as wooden fences, might well be a better choice that can be installed temporarily in front of newly replanted mangrove forests. In Figure 3.1a, a wooden fence is shown that was constructed from mainly natural materials. The assembly consists of two (Figure 3.1a) to three (Figure 3.1b) lines of vertical bamboo poles, with forwarding-oriented poles that cover the horizontal branches (brushwood bundles) of the inner parts (Albers, San and Schmitt, 2013; Gijón Mancheño et al., 2017; Ngo, Mai and Mai, 2018; Schmitt and Albers, 2014; Schmitt et al., 2013; Thieu Quang and Mai Trong, 2020; Van Cuong et al., 2015).

Figure 3.1: Type of bamboo fences in the Mekong Delta. Courtesy Hoang Tung Dao, 2016 (a) and Le Xuan Tuan, 2020 (b)

Studies of wave reduction due to brushwood fences with a similar structure have been carried out in physical and numerical models. Sayah and Schleiss (2006) investigated wave-fence interaction in a physical scale model, which pointed out the dominant role of wave steepness and porosity and concluded that wave reduction depended on dominant wave steepness in response to the density of the structure. Mai (1999) also

investigated wave transmission through prototype-scale brushwood fences, which appeared to be strongly dependent on the wave period. Interestingly, both studies suggested that the main parameter influenced wave transmission was the relative freeboard (R_c/H_I), with R_c is the freeboard defining the difference of fence crest and water surface. Recently, Thieu Quang and Mai Trong (2020) numerically examined the existing field data of wave damping due to bamboo fences in the Lower Mekong Delta (Albers, San and Schmitt, 2013; Schmitt et al., 2013). With numerical results, an empirical formulation of wave transmission by wooden fences was consequently derived from field data, a function of the relative freeboard, fence thickness and porosity. Dao et al. (2018) numerically studied wave reduction due to a wooden fence as vertical cylinders to mimic the fence. This study suggested that the wave damping increases with the increase of both wave nonlinearity, as indicated by the Ursell number, and the thickness of wooden fences. Moreover, field experiments of wave reduction due to wooden fences were carried out along Mekong Delta coasts which wave and current energies were significantly reduced by wooden fences (Albers, San and Schmitt, 2013; Schmitt et al., 2013; Van Cuong et al., 2015). The above studies only point out the relationship between wave transmission and the geometrical parameter of wooden fences, i.e., freeboard and thickness.

To estimate wave reduction by an array of cylinders, most often used to mimic a vegetation area, both energy-balance (phase-averaged) models and the momentum-balance (phase-resolved) models are applied. These models use the effect of drag forces exerted on rigid cylinders, as expressed by the Morison equations (Morison, Johnson and Schaaf, 1950), to determine the wave energy loss due to cylinders. Due to the increased simulated resolution, the phase-resolved models consume more computation time than the phase-averaged models. Dalrymple, Kirby and Hwang (1984) modified the energy-conservation models by adding the effect of wave breaking and irregular waves (Mendez and Losada, 2004) that was further developed by including wave dissipation in the vertical direction on horizontal cylinders that is absent for vertical cylinders (Suzuki et al., 2019). In the newest model, the process of wave reduction due to an array of cylinders can be quantified in detail by the characteristics of the cylinder array, i.e., diameter (D_v, m), density (N_v, cylinders/m^2) and the bulk drag coefficient ($\overline{C_D}$).

Additionally, the description of flow and wave resistance of wooden fences and vegetation are comparable, as both are essentially caused by the drag forces on an array of cylinders. From this perspective, the bulk drag coefficient, therefore, is an important parameter to characterize the flow and wave resistance by vegetation. The bulk drag coefficient is an important parameter to characterize the flow and wave resistance by vegetation. The bulk coefficient was generally investigated by the physical model, which used only for vertical cylinders mimicking vegetated areas (Anderson and Smith, 2014; Chen et al., 2018; Hu et al., 2014; Ozeren, Wren and Wu, 2013; Tanino and Nepf, 2008). Because of the effects of shielding and blockage around vertical cylinders with a high density, the bulk drag coefficient inside an area of cylinders is often higher than its value for a single-cylinder in an open flow (Hu et al., 2014; Ozeren, Wren and Wu, 2013). However, for the complex orientation of vegetation in the field where mangrove roots have an inhomogeneous orientation, i.e., schematically vertical, and horizontal orientations,

the bulk drag coefficient is usually underestimated. Dao et al. (2020) carried out a series of experiments to investigate bamboo fences' flow resistance by assessing the bulk drag forces under stationary flow. The bulk drag coefficient of inhomogeneous and staggered arrangements was obtained in both a model- and full-scale experiment, strongly influenced by the porosity, random arrangement, and Reynolds number.

In this study, a 2D physical model was built to generate a validation data set for wave damping due to wooden fences in model-scale. In this physical model, the brushwood branches with an inhomogeneous arrangement were used to mimic the irregular configuration applied in the real wooden fences (Figure 3.1). Next, this 2D model was reproduced in a numerical model to validate the momentum balance model which was applied in the time-domain wave-model SWASH (Simulation Wave till Shore) (Zijlema, Stelling and Smit, 2011). SWASH is a general-purpose numerical model to simulate non-hydrostatic and free-surface flow phenomena in the coastal water (Phan et al., 2019; Reis et al., 2020). The bulk drag coefficient is typically used as a calibration parameter such that a pure validation is not possible. Therefore, the bulk drag coefficient, separately obtained in another experimental set-up for model- and full-scale fences by Dao et al. (2020), was applied to run the numerical model for the validation (Table 3.3). In the next step, the bulk drag coefficient for full-scale fences, that was also obtained in Dao et al. (2020), was applied to repeat the calculation at full-scale. Based on the bulk drag coefficient results in the full-scale SWASH model, the scale effects of wave damping due to wooden fences could be estimated while, the applied model set-up was still validated by empirical observation.

This study is organized as follows. In section 2, the methodology is presented in several subsections, describing the interaction processes between wave and wooden fence, the scale consideration, the physical and numerical model descriptions. The validation of the numerical model is presented, and the scaling simulations results are illustrated in section 3. The discussion is presented in Section 4. Finally, the conclusions are provided in Section 5.

3.2 Methodology

In this section, first, the wave-fence interactions are introduced, including wave reflection, wave dissipation, and wave transmission processes. Next, several scaling considerations are presented to choose the scaling factor for scaling wooden fence characteristics and wave conditions. Next, the physical model of wave-fence interactions of the model-scale is described. Finally, the numerical model reconstructs the physical model used to validate the physical data and its uses for scaling the computations.

3.2.1 Wave-Fence interaction

Three main processes often characterize the interaction between wave and wooden fences, i.e., wave reflection in front and wave dissipation inside, resulting in wave transmission

behind the wooden fence. In some conditions overtopping and breaking waves influence these processes, depending on water depth, inhomogeneous structures, and incoming wave height. The common expression for wave-fence interactions that was proposed for wave-porous structures by Thornton and Calhoun (1972) can be described as

$$K_R^2 + K_D^2 + K_T^2 = 1 \tag{3.1}$$

where K_D is the dissipation coefficients; K_R and K_T are the reflection and transmission coefficients, respectively, which is indicated as:

$$K_R = \frac{H_R}{H_I} \tag{3.2}$$

$$K_T = \frac{H_T}{H_I} \tag{3.3}$$

where H_I, H_R and H_T correspond to the incident, reflected, and transmitted (significant) wave heights. The definition of these wave heights is indicated further in the Physical model section (section 3.2.3).

The degree of dissipation is influenced by the fill material inside the structure. As mentioned, a wooden fence is mainly constructed by bamboo branches which create the dissipation caused by drag and friction. The drag and friction by cylinders are strongly dependent on the flow regime around the cylinders. The hydrodynamic quantities of oscillatory flow in a porous medium can be described by both the Keulegan-Carpenter number (KC number) with $KC = uT/D$ and Reynolds number (Re) with $Re = uD/\nu$ where T is the wave period, ν (m^2/s) is the kinematic viscosity, u (m/s) is the flow velocity for a steady flow or orbital velocity for an oscillation flow, and D (m) is cylinder diameter. The relationship between the drag coefficient for a single cylinder (C_D) and KC number has been reported by Keulegan and Carpenter (1958) for wave-cylinder interaction and by Chen et al. (2018); Mendez and Losada (2004); Ozeren, Wren and Wu (2013) for wave-vegetation interaction. The relationship between bulk coefficient ($\overline{C_D}$) and Reynold numbers for wave-vegetation interaction has been suggested by, amongst others, Hu et al. (2014). The $\overline{C_D}$ values were even more complicated due to the inhomogeneous arrangement as well as to the high density for wooden fences, which were discussed for flow-fence interaction in Dao et al. (2020). Dao et al. (2020) tested the different arrangements of the inner parts (i.e., the inhomogeneous and staggered configuration) in 1:5 model-scale (D_m) and full-scale diameters (D_p). It is noted that subscript "m" and "p" are denoted for respectively small and full scales. The bulk drag coefficient with the formulation $Re - \overline{C_D}$ is shown in Table 3.1.

3.2.2 Scaling considerations

A down-scaled model often represents the real-world prototype used to indicate the technical and economic solutions of hydraulic engineering problems (Novák and Čábelka, 1981). In hydraulic engineering, Froude scaling is often used to up-scale physical

Table 3.1: Drag coefficient formulas

Number	Formulas	Arrangement	Porosity (n)	Diameter (mm)	Filter velocity (m/s)	Scale
1	$\overline{C_{D,m1}} = 3.87 + (\frac{177.2}{Re_n})^{1.23}$	Inhomogeneous	0.90	4.0	0.0 - 0.4	1 : 5
2	$\overline{C_{D,m2}} = 1.99 + (\frac{326}{Re_n})^{0.65}$	Staggered	0.81	4.0	0.0 - 0.4	1 : 5
3	$\overline{C_{D,p1}} = 1.98 + (\frac{586}{Re_n})^{1.39}$	Staggered	0.81	20.0	0.0 - 0.4	Full

model results (Heller, 2011). The scale models reproduce aspects like non-linear waveforms and multi-scale turbulence phenomena rather well if the scale model is not too small. However, as a result of the different scales, scale effects occur due to a lack of ability to keep each relevant force ratio constant between small- and full-scale models (Heller, 2011; Hughes, 1993). Generally, the scale effect for a specific phenomenon increases with the length scales which is the ratio of characteristic length of real-world to model length. Thus, the scale effect increases with the decreasing size of the model. In numerical models, the effects that lead to scale effects at the small scale can be switched on or off, for example, the effects of kinematic viscosity that increase the drag on cylinders, bed friction, or surface tension.

To scale wave conditions in this study, the Froude time scale (Hughes, 1993) is applied as $N_T = \sqrt{N_L}$, where $N_L = D_p/D_m$ is the length scale. As mentioned, the inner parts of the wooden fence were tested for flow resistances with two main arrangements (Dao et al., 2020): (1) the inhomogeneous mimicking the field arrangement for model scale, and (2) the staggered arrangement for both model scale and full scale. The tested diameters of the horizontal branches were chosen as 4.0 mm (D_p) and 20.0 mm (D_m) for the model- and full-scale fences, respectively. As a result, the length and time scales are $N_L = 5.0$ and $N_T = 2.2$, respectively.

The hydraulic test conditions are chosen to resemble those of the east side of the Mekong Delta coast. For the wave conditions, at a distance of 100 km from the shore of the Mekong Delta coast, the water depth reaches nearly 30 m, where the highest significant wave height and wave period in a return period of 100 years are about 10.5 m and 11.5 s, respectively (Hoang and Nguyen, 2006). Near the shore, the coast is a gently sloping foreshore with a slope from 1 : 500 to 1 : 1000 Thieu Quang and Mai Trong (2020). The water depth for these slopes is about 2.0 m (Ngo, Mai and Mai, 2018; Thieu Quang and Mai Trong, 2020) under the semi-diurnal tide with an amplitude of 2.5 m to 3.8 m (Gagliano and McIntire, 1968; Nguyen, Ta and Tateishi, 2000; Ta et al., 2002; Wolanski et al., 1996). A combination of the low water depth and the gently sloping foreshore can generate a strong environmental dissipation for waves. Thus, the primary wind waves will quickly lose their energy in the transmission process. As a result, wave heights, before reaching the foreshore, were reported below 0.8 m and wave periods ranged from 4.0 to 7.5 s at a water depth of nearly 2.0 m (Thieu Quang and Mai Trong, 2020). Moreover, the characteristics of wooden fences in the Mekong Delta coast were reported in Albers,

San and Schmitt (2013); Ngo, Mai and Mai (2018); Schmitt et al. (2013); Thieu Quang and Mai Trong (2020). The typical characteristics of the fences include a maximum thickness of 1.2 m, and a height of 1.6 m at a water depth of 2.0 m during high tide and under submerged conditions. In this study, characteristics of wooden fences and wave conditions were scaled down based on the maximum values, and they are presented in Table 3.2.

Table 3.2: Characteristic of wave conditions and wooden fences in full and model-scale

Characteristic values	Full-scale	Model-scale (1 : 5)
Fence height (m)	1.6	0.32
Fence thickness (m)	1.2	0.24
Water depth (m)	2.0	0.40
Significant wave height (m)	1.0	0.20
Peak wave period (s)	7.5	3.40

3.2.3 Physical model

In the Mekong Delta, the very gentle foreshore slopes (order 1/10,000) create a significantly attenuated environment for waves (Phan, van Thiel de Vries and Stive, 2014) before interacting with wooden fences. The gentle slopes generally cause an increase in the longwave energies after dissipating mostly short wave energies so that these energies are of the same order-of-magnitude and their negative correlation changes into a positive one at the entrance of the shallow zone to the brushwood fence location (Roelvink and Stive, 1989). It is nearly impossible to scale such extremely gentle slopes of Mekong Delta in a wave flume, such as the wave flume in Delft University of Technology. Therefore, the generation of free-long waves from forcing a wave train with bound-long waves to break at a steep slope (Buckley et al., 2015; Tsai et al., 2005) is applied to mimic the slope needed.

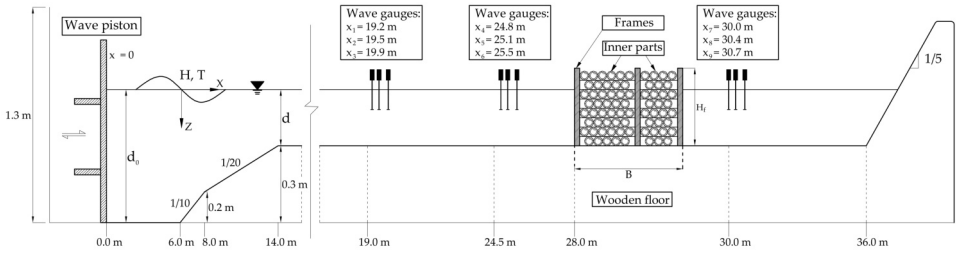

Figure 3.2: Schematization profile used in physical and SWASH model

Physical tests of wave interaction with wooden fences were conducted in the wave flume in the Hydraulic Engineering Laboratory at Delft University of Technology. The wave flume measures 38 × 0.8 × 1.0 m. The applied set-up is shown in Figure 3.2 and

represents the Mekong Delta cross-shore profile in a schematic and truncated fashion. The deep and shallow zone are connected by a composite slope of 1/10 and 1/20, where the offshore waves adapt to the shallow part by shoaling and breaking. At the left side of the flume, the wave generator (wave piston) is equipped with both Active Reflection Compensation (*ARC*) and second-order wave steering. At the downstream side, an impermeable smooth dike with a slope of 1/5 was installed to mimic the real dike along the foreshore of the Mekong Delta coast. In the shallow zone, nine Wave-Gauges (*WGs*) were installed in front and behind the wooden fence at $x = 28.0$ m (Figure 3.2).

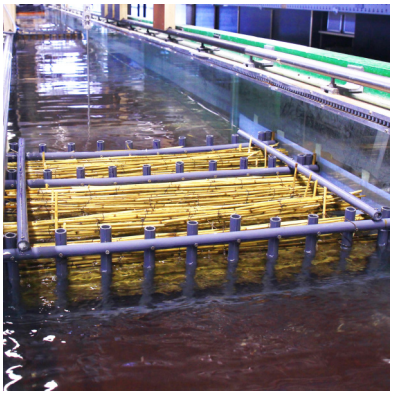

Figure 3.3: Model wooden fences in the physical tests.

The model wooden fence (Figure 3.3) included a frame and the inner parts. The inner parts mimicked the configuration of a fence in the field, as shown in Figure 3.1. According to Schmitt and Albers (2014), three rows of vertical bamboo piles created the largest thickness ($B = 1.2$ m, see Table 3.2) and two layers of piles for smaller thicknesses. The increase of vertical rows increases the structural stability for larger thicknesses. The same structure was also successfully used in another place along the Mekong Delta coast, as corroborated by Ngo, Mai and Mai (2018). In the present physical test, the construction with three vertical rows was applied for the largest thickness. The top-view of this fence set-up is presented in Figure 3.4a. Three thicknesses were used in this physical test, including $B = 0.28$ m; 0.40 m; and 0.66 m, while only one fence height, $H_f = 0.3$ m, was used in all tests.

The wooden fence frames used bamboo poles with a diameter of 0.08 to 0.10 m each, which is the mean diameter in the field (Albers, San and Schmitt, 2013; Ngo, Mai and Mai, 2018; Schmitt et al., 2013). In this study, PVC piles with a diameter of 0.02 m were used as bamboo poles that scaled-down with a length scale of 5.0. The PVC piles are designed with a smooth surface and completely straight, leading to slightly less wave dissipation by these vertical poles. For the case with inner parts, the role of the PVC frames in wave damping could be neglected, but the design is conjectured to be closer to reality. Following the same construct of the field-frames, the frames were constructed from ten vertical piles over the flume width, producing an 8.7 cm distance between two piles

(Figure 3.4a). The inner part contained inhomogeneous bamboo branches with a mean diameter of 0.004 m and consisted of the same material used for the steady flow experiments by Dao et al. (2020) (Figure 3.4b). Because brushwood fences were assembled from cylindrical PVC piles and bamboo sticks, the porosity could be calculated in a relatively straightforward fashion. The density of the inner parts was about 8705 piles/m^2 corresponding to the mentioned thicknesses above. The porosity was 0.90 for all thicknesses.

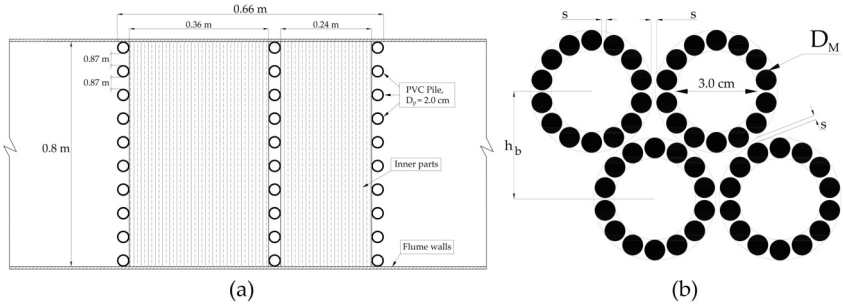

Figure 3.4: (a): the view from the top of a wooden fence, (b): Inhomogeneous arrangement of inner parts (Dao et al., 2020).

All Wave Gauges (WGs) had a sampling rate of 100 Hz. The measurements lasted at least 500 waves so that the gathering of representative statistical data could be collected. The error of WGs is given as 0.5% of the measuring range that was set as 0.1 m (Deltares). Two groups of gauges (WG1 to WG6) measured times series elevation used to extract incident and reflection waves in front of the wooden fence. The method of Zelt and Skjelbreia (1993) was applied to split the incident and the reflected wave signals. Then, the reflected and incident wave heights were calculated by the significant wave height, $H_{m0} = 4\sqrt{m_0}$ with m_0 is the zeroth-order moment of the water surface elevation. In particular, the incident wave signals of WGs1-3 were used as input boundaries of the numerical model. In contrast, wave elevations of WGs4-6 near the brushwood fence were used for calculating the incident and reflected waves (Figure 3.2). To calculate reflection and transmission coefficients following Equation 3.2 and 3.3, the incident ($H_{I,m0}$) and reflected wave heights ($H_{R,m0}$) were exacted from WGs4-6 signals at the location near the front face of the fence. It is noted that the method to extract incident and reflected wave heights are based on linear wave theory that can be applied for wave signals in front of the fence. However, transmitted wave heights are relatively small after damping by the fences leading to an increase of finite amplitude effects. As a result, errors in calculating incident and reflection for transmitted wave heights are inevitable (Zelt and Skjelbreia, 1993). Therefore, the transmitted wave heights ($H_{T,m0}$) were calculated as the average of total wave heights measured by WGs7-9 signals behind the fence.

Based on the small-scale wave conditions in Table 3.2, tests were performed for three shallow water depths (d_m) that varied from 0.15 m to 0.25 m. It should be noted that the

wooden fence was tested only in an emerged condition due to the limited dimensions of the wave flume. Peak periods ($T_{p,m}$) from 1.1 s to 2.7 s were used. For each water depth three fence thicknesses varying from 0.28 m to 0.66 m were applied (Table 3.4). The fence thicknesses were extended from a scaled value of B_m = 0.24 m (Table 3.2). This extension was aimed at testing the dependency of wave damping on fence thickness. For each combination of peak period, depth and fence thickness, three scaled significant wave heights ($H_{s,m}$) varying from 0.03 m to 0.075 m were imported in wave generator at deep water (Figure 3.2). As a result, there were a total of 27 tests performed in the wave flume. All tests were performed with irregular waves using the JONSWAP spectrum with peak enhancement factor γ = 3.3. Wave conditions were named from Val.01 to Val.09, as presented in Table 3.3.

Table 3.3: Characteristics of wave and wooden fence for the physical (Val cases) and numerical (Val and Sca cases) models

Cases	Model scale				Prototype scale			
	B_m (m)	d_m (m)	$T_{p,m}$ (s)	$H_{s,m}$ (m) (*)	B_p (m)	d_p (m)	$T_{p,p}$ (s)	$H_{s,p}$ (m) (*)
Val.01	0.28	0.15	1.1	0.035; 0.055; 0.075	-	-	-	-
Val.02	0.28	0.15	1.2	0.030; 0.050; 0.070	-	-	-	-
Val.03	0.28	0.15	1.4	0.030; 0.050; 0.070	-	-	-	-
Val.04	0.40	0.20	1.3	0.030; 0.055; 0.070	-	-	-	-
Val.05	0.40	0.20	1.6	0.030; 0.050; 0.070	-	-	-	-
Val.06	0.40	0.20	1.8	0.030; 0.050; 0.070	-	-	-	-
Val.07	0.66	0.25	2.7	0.030; 0.045; 0.055	-	-	-	-
Val.08	0.66	0.25	2.4	0.030; 0.050; 0.070	-	-	-	-
Val.09	0.66	0.25	2.1	0.030; 0.055; 0.070	-	-	-	-
Sca.01	0.28; 0.40; 0.66; 0.92	0.15	2.1	0.06	1.4; 2.0; 3.3; 4.6	0.75	4.7	0.32
Sca.02	0.28; 0.40; 0.66; 0.92	0.25	2.1	0.11	1.4; 2.0; 3.3; 4.6	1.25	4.7	0.53
Sca.03	0.28; 0.40; 0.66; 0.92	0.30	2.1	0.14	1.4; 2.0; 3.3; 4.6	1.50	4.7	0.64
Sca.04	0.28; 0.40; 0.66; 0.92	0.35	2.1	0.15	1.4; 2.0; 3.3; 4.6	1.75	4.7	0.74
Sca.05	0.28; 0.40; 0.66; 0.92	0.45	2.1	0.19	1.4; 2.0; 3.3; 4.6	2.25	4.7	0.95
Sca.06	0.28; 0.40; 0.66; 0.92	0.55	2.1	0.23	1.4; 2.0; 3.3; 4.6	2.75	4.7	1.16
Sca.07	0.28; 0.40; 0.66; 0.92	0.15	2.4	0.06	1.4; 2.0; 3.3; 4.6	0.75	5.4	0.32
Sca.08	0.28; 0.40; 0.66; 0.92	0.25	2.4	0.11	1.4; 2.0; 3.3; 4.6	1.25	5.4	0.53
Sca.09	0.28; 0.40; 0.66; 0.92	0.30	2.4	0.14	1.4; 2.0; 3.3; 4.6	1.50	5.4	0.64
Sca.10	0.28; 0.40; 0.66; 0.92	0.35	2.4	0.15	1.4; 2.0; 3.3; 4.6	1.75	5.4	0.74
Sca.11	0.28; 0.40; 0.66; 0.92	0.45	2.4	0.19	1.4; 2.0; 3.3; 4.6	2.25	5.4	0.95
Sca.12	0.28; 0.40; 0.66; 0.92	0.55	2.4	0.23	1.4; 2.0; 3.3; 4.6	2.75	5.4	1.16

(*) Target wave height inputs at the offshore positions.

3.2.4 Numerical model

The SWASH model is applied to run the validation and scaling tests in this study. It is a time-domain model for simulating non-hydrostatic free-surface flow based on the non-linear shallow water equations, including the non-hydrostatic term (Zijlema, Stelling and Smit, 2011). It can also accurately account for wave attenuation and wave breaking processes in the near-shore (Smit, Zijlema and Stelling, 2013). In this study, the numer-

ical model was set up based on the physical model, such that its results can exactly be compared to those of the physical model results. Next, the numerical models for scaling the simulations are presented, which are constructed similar to the physical model in the model-scale and the full-scale. Thus, the results can investigate the scale effects and wave-fence interactions.

The settings of the model- and full-scale runs are as follows. A spatial resolution (Δx) about 1/100 of a peak wavelength (L_P) was applied as 0.01 m for all model calculations and 0.05 m for full-scale calculations resulting in 4000 grid points along with the profile, i.e., 40 m long for small-scale and 200 m for the large-scale model. The wave boundary for all tests was installed on the left side of the profile (Figure 3.2). For validation calculations, the wave boundary was set at x = 19.0 m (Figure 3.2), where the time series of incident surface elevation was imposed. The initial water level was set to zero. An initial time step of 0.001 s was employed for every simulation. Two vertical layers were applied for every numerical run to increase the accuracy of the validation runs.

Next, the validated wave model is used to quantify the scale effects in the 1:5 scale physical model and to determine the origin of scale effects. Wave conditions for scaling runs and their validation were presented in Table 3.3. For the validation runs, the same wave conditions were imposed as in the physical model tests, named Val.01 to Val.09. For scaling runs naming Sca.01 to Sca.12 in Table 3, each wave height was tested for one water depth corresponding to the ratio $H_{s,i}/d$ of roughly 0.42. Two wave periods were chosen as 2.1 and 2.4 s for small-scale tests corresponding to 4.7 and 5.4 s for full-scale simulations. For each wave condition, i.e., several peak wave periods, significant wave heights, and water depths, fence thicknesses were tested, as presented in Table 3.4. Besides the properties of the wooden fence for validation tests, the characteristics of the fence with a porosity of 0.81 used for the scaling, calculations are given.

Table 3.4: Characteristic of wave conditions and wooden fences in full and model-scale

Characteristics	Model scale		Full scale
Thickness, B (m)	0.28; 0.40; 0.66	0.28; 0.40; 0.66; 0.92	1.4; 2.0; 3.3; 4.6
Height, H_f (m)	0.30	0.30	1.50
Cylinder diameter, D (m)	0.004	0.004	0.02
Density, N_c (Cylinders/m^2)	8705	13077	603
Porosity, n (-)	0.90	0.81	0.81
Fence location (m)	28.0	28.0	140.0
Arrangement	Inhomogeneous	Staggered	Staggered
Test	Validation	Scaling	Scaling

The physical conditions that influence wave dissipation processes in this study include viscosity and bed friction. For model-scale tests, the vertical turbulence viscosity was set to 3×10^{-4} m^2/s, and Manning's roughness as bed friction coefficients were deployed as a default factor as 0.019 ($m^{-1/3}s$) (Zijlema, Stelling and Smit, 2011). For the larger-scale runs, it is assumed that the flume was set with the same bed materials;

therefore, bed friction should remain the same as at the small-scale tests. The inertia force was included with the added mass coefficient set for all tests as $C_m = 1$. It should be noted that only characteristics of the inner part were described in every simulation test. Further boundary conditions are described in Zijlema, Stelling and Smit (2011).

The main concern is the settings of wooden fences that are influenced by the drag coefficient in this study. In the version of the SWASH model (version 6.01), the vegetation model that can simulate wave reduction due to an array of stiff cylinders was applied to mimic wooden fences. The full description of the implementation of vegetation in SWASH, including horizontal cylinders, is given in Suzuki et al. (2019). In this model, the effects of the cylinder arrangement on the flow/waves are represented by the cylinder diameter, (and) the density of cylinders, and the bulk drag coefficient. The bulk drag coefficient for the present arrangement was obtained from experiments (e.g., Dao et al. (2020) at both the model- and the full-scale. The formulas of $Re_n - \overline{C_D}$ are presented in Table 3.1, and in this study, the Reynolds number is described as Re_n:

$$Re_n = \frac{U_{max} D}{n\nu} \tag{3.4}$$

where n is the porosity and U_{max} (m/s) is the maximum amplitude of the horizontal wave orbital velocity based on the linear wave theory for a wave with significant heights (H_{m0}).

The application of the $Re_n - \overline{C_D}$ relation in the wave simulations is not straightforward, as Re_n changes over the thickness and height of the fence. A representative bulk drag coefficient should be applied. The orbital wave velocity strongly depends on the wave height magnitude during the wave propagation progress. A reduction of wave height and decrease of wave velocity occur with the frontal contact along with the thickness. Indeed, Figure 3.5 illustrates wave heights (Figure 3.5a) and the maximum wave velocity at mid-water depth (Figure 3.5b) over the thickness of the wooden fence for the case with H_{m0} = 0.07 m; T_p = 2.1 s; d = 0.25 m; B = 0.66 m; and $\overline{C_D}$ = 4.2. It is shown that the wave height reduces along with the 0.66 m thickness from about 0.09 m to 0.04 m. As a result, the wave velocities and Re_n follow a similar trend. According to the measured relation between Re_n and $\overline{C_D}$ in prior experiments (Dao et al., 2020), the bulk drag coefficient increases with the decrease of wave velocity, and it reaches the highest value at the end of the wooden fence. However, most wave dissipation occurs at the upstream side of the fence. Therefore, a location at the upstream side just inside the wooden fence (x = 28.05 m) was chosen to obtain the bulk drag coefficient. However, the $\overline{C_D}$ value cannot be achieved in a single run for validating the transmitted wave height, as the chosen value for $\overline{C_D}$ influences the velocity inside the fence. Thus, it is necessary to have an iterative computation to achieve an acceptable value of $\overline{C_D}$. With an initial value for $\overline{C_D}$ of one case, e.g., inhomogeneous and staggered case, one iteration was sufficient to obtain a converged value for K_T.

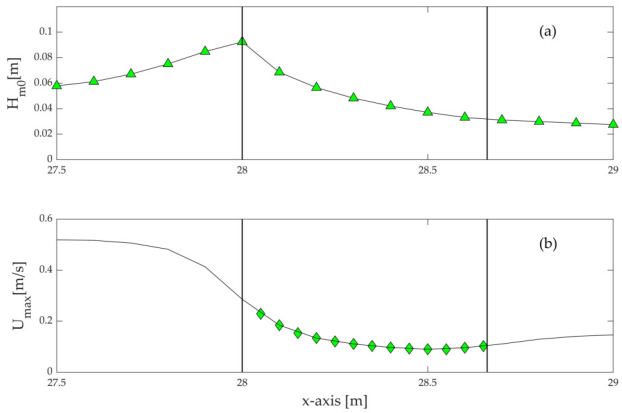

Figure 3.5: Wave heights (a) and maximum velocity (b) for the case with H_{m0}=0.07 m; T_p=2.1 s; d=0.25 m; and B=0.66 m

After choosing a suitable location for the bulk drag coefficient, the relationship between the $\overline{C_D}$, that was applied in the last iteration run and the Re_n, that was obtained with the $\overline{C_D}$, should follow the relation between the two parameters, as given in Table 3.1. Hence these combinations are plotted for all tested cases, including validation and scaling runs, in Figure 3.6 to control sequence together with the relations from Table 3.1. The good correspondence shows that one iteration applied was sufficient. It should be noted that one wave condition shown in Table 3.3 to control sequence can obtain one value of $\overline{C_D}$ even with the larger thickness fence. Therefore, a total of 27 values of $\overline{C_D}$ for validation runs and a total of 12 values of $\overline{C_D}$ for scaling runs are presented in Figure 3.6. All staggered cases can fit in one line due to the same porosity and configuration but different Reynolds numbers.

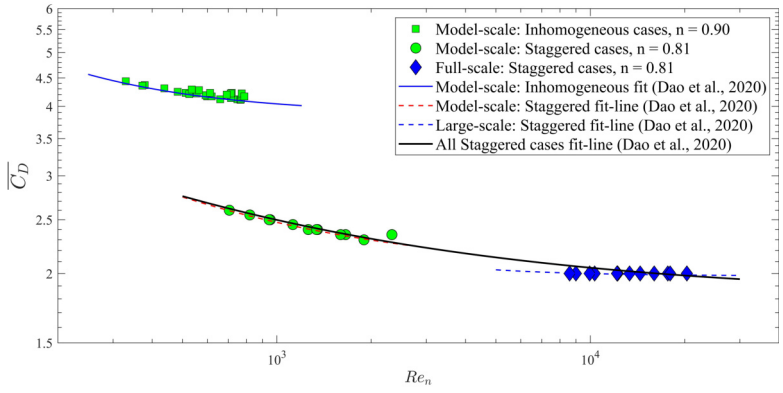

Figure 3.6: Drag coefficient and Reynolds number.

3.3 Results

In this section, the validation results are presented, in which the SWASH model is validated with the physical model results. The inspected parameters are the significant wave heights, and the surface elevation at wave gauges in front and behind wooden fences. Next, the scale differences between the two scales are presented. Finally, the interaction between waves and wooden fences is then presented, assessed by the reflection, dissipation, and transmission processes.

3.3.1 Validation results

The highest significant wave heights of case Val.01 to Val.09 (Table 3.3) are chosen to present wave transformation through wooden fences. The computed (blue line) and observed (green diamond) total significant wave heights are compared for the selected cases in Figure 3.7. Note that the observed wave heights at the measurement locations were within 10% of the target values. In general, the SWASH model results correspond well to the observed wave height variations. Especially for longer wave cases (Figure 3.7g, 3.7h, and 3.7i), the calculated node and anti-node standing wave pattern explain the wave height variation measured by the gauges in the physical model. Behind the fences, the SWASH results indicated that the measured significant wave height behind the fence is outside the standing wave pattern induced by the reflection from the slope at the end of the profile.

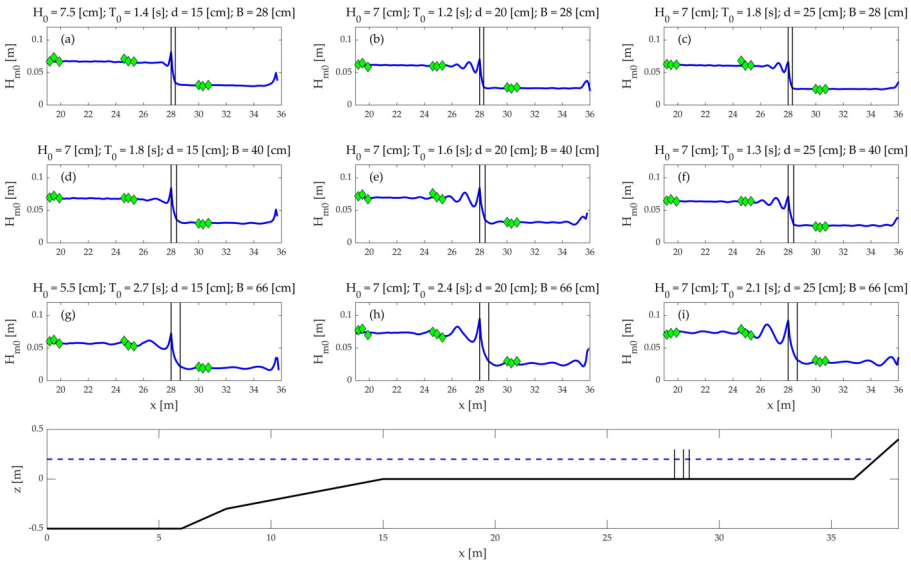

Figure 3.7: Comparing total significant wave heights between physical model (green diamond) and numerical model (blue line). Vertical lines at $x = 28.0$ m present for wooden fences.

Figure 3.8 compares the computed and recorded time series of the surface elevation

for case Val.07 (Table 3.3) at three locations at the beginning of the foreshore (WG3, x = 19.9 m), in front of the wooden fence (WG6, x = 25.5 m), and behind the fence (WG7, x = 30.0 m). Generally, the comparison shows a good agreement between SWASH and the physical model results, especially at locations near the wooden fence. When the wave boundary for SWASH was located near 19.0 m, which is very close to the wave gauge 3, the surface signals were captured very well. At a location closer to the fence, gauge 6, the elevations between two models still agree well. The comparison at gauge 7 (between the wooden fence and dike) is not as good as those in front of the fence. The larger waves still seem to correspond well between experiment and simulation, but the phases of the higher frequency waves seem to be misrepresented.

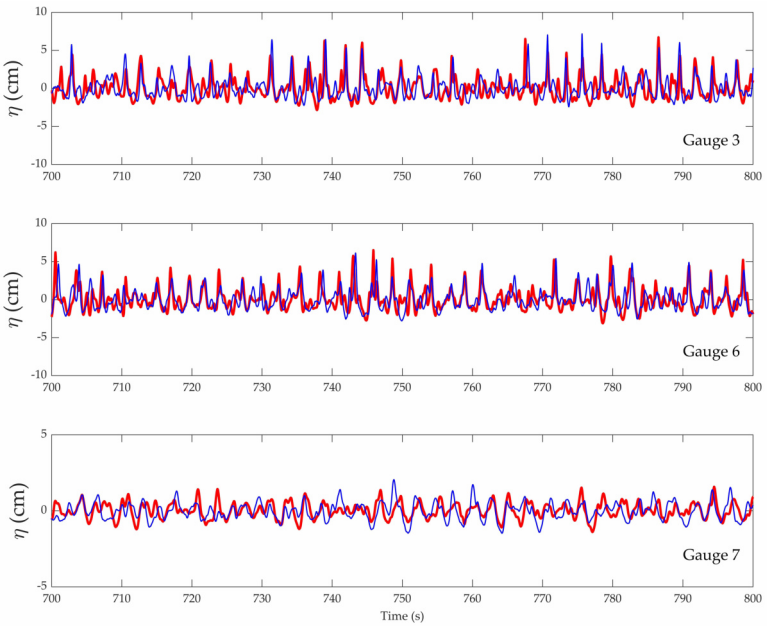

Figure 3.8: Comparison of water elevation between computation (thick red line) and observation (blue line): Top panel: at the beginning of the foreshore (WG3, x = 19.9 m); Middle panel: in front of the fence (WG6, x = 25.5 m); and Bottom panel: behind the fence (WG7, x = 30.0 m).

The corresponding wave spectral densities are derived by applying the Fast Fourier Transform (FFT) to water elevation data in Figure 3.8, as presented in Figure 3.9. A good agreement of total wave spectral densities between the computation (red dash line) and observation (solid blue line) for the mentioned cases is shown. The two spectra of the locations upstream of the fence show two peaks caused by the strong decrease in-depth (Beji and Battjes, 1993). The reproduction had a small mismatch at a peak at about 0.75 Hz and below 0.25 Hz at the beginning of the foreshore (WG3; x = 19.9 m, Figure 3.9a). At the location near the fence, WG6 (x = 25.5 m), the SWASH model reproduced the wave spectral density in comparison to the experimental one very well (Figure 3.9b). Behind the fence, SWASH might produce two peaks of the spectrum, while only one

peak appeared from the measurement (Figure 3.9c). It is noted that in Figure 3.9c, the low-frequency spectrum was missed by the SWASH model compared to the observations. This mismatch might be due to the fact that the low-frequency waves are not being produced well after being filtered by the wooden fence. Moreover, the low frequencies (< 0.25 Hz) are not well resolved due to the limited duration of both the computation and the experiment, and contain little energy. Hence it is difficult to draw firm conclusions about it.

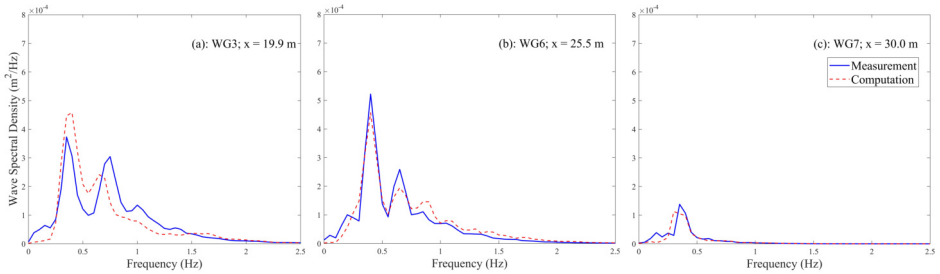

Figure 3.9: Comparison of wave spectral density between computation (red dash line) and observation (thick blue line) at the beginning of the foreshore (Gauge 3), in front of the fence (Gauge 5) and behind the fence (Gauge 7).

Furthermore, the predictive skill of SWASH was calculated applying the bias, and the scatter index SI, which is defined as:

$$bias = \frac{1}{N}\sum_{i=1}^{N}(\varphi^{i}_{comp} - \varphi^{i}_{obs}) \tag{3.5}$$

$$SI = \frac{\sqrt{\frac{1}{N}\sum_{i=1}^{N}(\varphi^{i}_{comp} - \varphi^{i}_{obs})^2}}{\frac{1}{N}\sum_{i=1}^{N}(\varphi^{i}_{obs})} \tag{3.6}$$

where φ_{comp} and φ_{comp} are the corresponding values for the statistical wave parameters that were measured and computed by SWASH, respectively, and N is the total number of data points in the considered data set (Zijlema, 2012).

Figure 3.10 indicates a good comparison of observation and computation of significant wave heights in front of and behind the wooden fence. In Figure 3.10a, the incident wave heights of WGs1-3 (green circle) and WGs4-6 (blue diamond) were generated with an acceptable level as the SI and BIAS are relatively low. For instance, the SI and BIAS of WGs1-3 are 2.4% and 0.3 mm, while these values of WGs4-6 are 3.8% and -1.0 mm, respectively. Figure 3.10a also shows that the reproduction of the significant incident wave heights from WGs4-6 was more accurate than WGs1-3. However, the errors are still relatively small compared to typical significant wave heights from 3.0 to 7.5 cm. It should be noted that there were no input values in the deep part of the computed domain. Thus, further calibration at the deep-water was not done. Comparison of the average significant wave heights of WGs7-9 for the measurement and computation are presented in

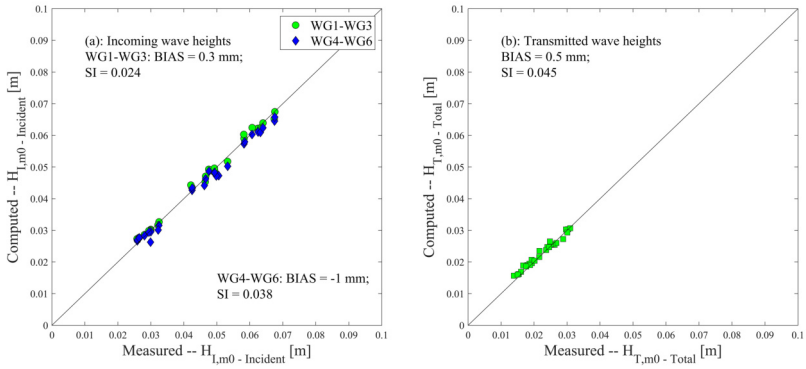

Figure 3.10: Comparison of wave heights between measurement and computation; (a): the incident wave heights, $H_{I,m0}$; (b): the transmitted wave heights, $H_{T,m0}$

Figure 3.10b. The average SI and BIAS of the transmitted significant wave heights are 4.5% and 0.5 mm.

3.3.2 Scaling differences of numerical simulations

The SWASH model has been validated with the physical model data using the bulk drag coefficient derived from separate experiments, as shown in the previous section. The result indicates that the numerical model can be used with confidence to simulate further scenarios for both model- and full-scale with the drag coefficients obtained from the separate experiments (Dao et al., 2020). Processes at the two scales that do not follow the Froude scaling law and, hence, can lead to scale effects are bed friction and bulk drag coefficient. The bulk drag coefficient for the fence was measured at both scales.

The wave propagation processes are first presented. Figure 3.11 shows the significant wave heights over the entire model domain for cases Sca.07 (Figure 3.11a, b), Sca.10 (Figure 3.11c, d), and Sca.12 (Figure 3.11e, f) of small-scale (scaled up with $N_L = 5$, dash line) and full-scale cases (blue line). Wave-fence interactions between the two scales were very similar when the wave height was significantly reduced due to the appearance of wooden fences at 140.0 m (vertical dash-dot line). Figures 3.11a and 3.11b indicate that small-scale waves are dissipated more than large-scale waves for the shallowest water depth ($d_m = 0.15$ m and $d_p = 0.75$ m) of case Sca.07 in front of the wooden fence. This difference might be caused by the model effect occurring at small wave conditions, even though the same bottom friction coefficient and fluid viscosity were applied for all runs in both small- and large-scale wave experiments. It is noticed that the difference between the two scales is narrowed when water depths increase for case Sca.10 ($d_m = 0.35$ m and $d_p = 1.75$ m) and case Sca.12 ($d_m = 0.55$ m and $d_p = 2.75$ m), as shown in Figure 3.11b and Figure 3.11c, respectively. Moreover, the small-scale wave dissipation might depend more on bottom friction than the larger-scale waves at a shallow water depth. The wave dissipation might then also be less affected by the bottom friction as the dis-

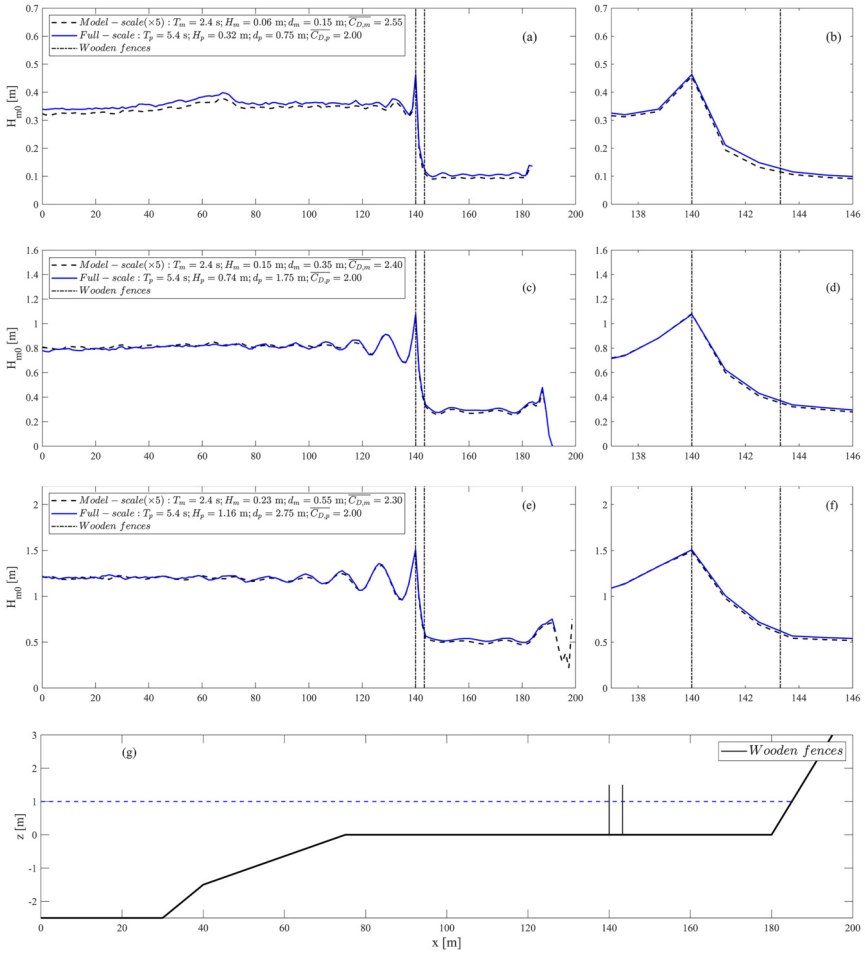

Figure 3.11: Wave transformation through wooden fences (dash-dot line) for upscaled small-scale (dash line) and full-scale cases (blue line). Waves transform in the entire domain and inside the wooden fence for case Sca.07 (a, b), case Sca.10 (c, d), and case Sca.12 (e, f). The foreshore bathymetry is given as reference (g).

persion rate of the wave orbital at water depths increases.

3.3.3 Wave-fence interaction

The interactions between waves and wooden fences are mentioned in the previous sections and are expressed by the reflection (K_R), transmission (K_T), and dissipation (K_D) coefficients in Equations 3.1, 3.2, and 3.3. To show the relationship between fence characteristics, such as characteristics of the brushwood branches, freeboard and thickness, and wave damping, these coefficients are plotted against relative fence thickness (B/H_I) and and relative freeboard (R_C/H_I) for numerical results. The numerical results are used

to explore the influence on the wave reducing properties of several important parameters that can be altered in the design of the fence.

Figure 3.12 presents the relationship between transmission coefficient and the relative freeboard for all cases, Val.01 to Val.09 and Sca.01 to Sca.12 (see Table 3.3). The influence of the freeboard on wave damping can be seen when the K_T values decease with the increase of R_C/H_I and is nearly constant for the $R_C/H_I > 0$. For the same range of R_C/H_I from -1.5 to 0.0, the K_T values of all staggered case (blue circle and green diamond) reduce from 0.35 to about 0.25 for most small wave cases, while the K_T values for largest wave cases (see Table 3.3) decrease 0.65 to 0.45. For most of cases water level under the fence crest, the K_T values are around 0.45 for inhomogeneous cases (black asterisk) and each staggered cases. It is noticed that the data points of all staggered cases are vertically scattered. This seems to be due to a different damping by different fence widths for the same freeboard.

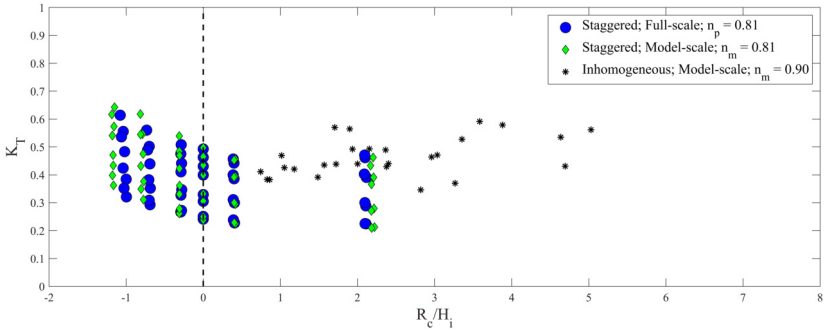

Figure 3.12: Plots of transmission coefficients against R_C/H_I.

As validated the numerical model in the previous section, the incoming and transmission waves are relatively matched resulting in a similarity of the expression of wave-fence interaction between the physical and numerical models. The relationship between wave-fence aspects of all full-fence cases Val.01 to Val.09 (Table 3.3) and the B/H_I is plotted in Figure 3.13. In the range of B/H_I from 3.0 to 25, a relatively small reflection in front of the wooden fence as K_R values around 0.4 (blue and green left-triangle), and a low wave transmission as K_T values range from 0.4 to 0.65 (blue and green hexagram) are indicated. Also, the efficiency of the wooden fence is therefore quantified by the dissipation coefficient, which increases from 0.8 to 0.9, occurs with the increase of B/H_I from 3 to 15, and keeps at about 0.9 until B/H_I increasing to 25 (blue and green diamond). The K_T values are about 0.4 to 0.55, which occur for H_I/d within 0.25 to 0.30 (blue hexagram). Meanwhile, the higher K_T values, the lower wave reduction, are about 0.60 to 0.70 occurs with $H_I/d < 0.25$ (green hexagram). The reduction occurs due to small waves that are more damped by a wooden fence than larger waves. It is noticed that the wave reflection coefficient is less dependent on fence thickness. In both groups of H_I/d, the K_R value are about 0.2 to 0.3 with the increase of B/H_I (blue and green left-triangle). It should be noted that this transmission coefficient is based on the total wave height cal-

culated from wave gauges at the downstream of the fence. Thereby, it is prone to some uncertainty discussed further in section Discussion.

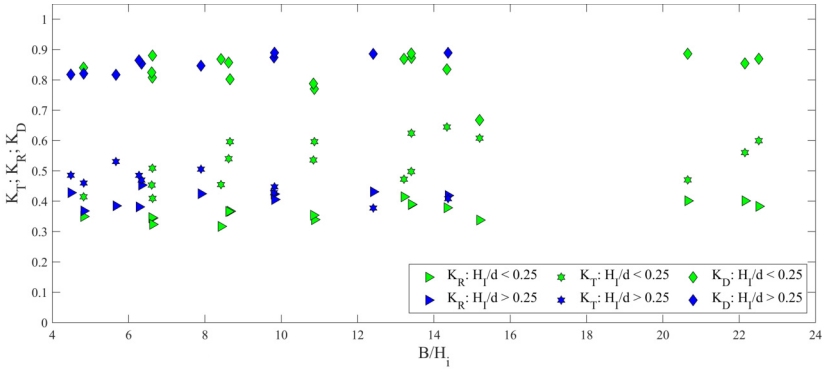

Figure 3.13: Plots of reflection, transmission, and dissipation coefficients against B/H_I for the physical model.

The relationships between B/H_I and reflection, transmission, and dissipation coefficient for all numerical runs, i.e., case Val.01 to Val.09 and Sca.01 to Sca.12 (see Table 3.3), are presented in Figure 3.14. For the case Sca.01 to Sca.12 with the same porosity (n = 0.81), the variation of these coefficients with the increase of B/H_I between the model-scale (green diamond) and the full-scale (blue circle) cases are quite similar. However, there is a small difference between the two scales, which is probably due to scale effects, as discussed in section 3.3.2. Particularly, the reflection and transmission of full-scale runs are slightly greater than the model-scale, as shown in Figures 3.14a and 3.14b, respectively. For instance, the K_R value of the full-scale model (blue circle) ranges from 0.40 to 0.55 while this value for the model-scale (green diamond) is from 0.35 to 0.45 in the same range of B/H_I from 1.0 to 15. The difference in K_T values between the two cases is about 0.05 within B/H_I from 1.0 to 5.0. In Figure 3.14c, the wave dissipation inside the wooden fence is interestingly matched for all inhomogeneous and staggered cases and increases from 0.7 to about 0.95 with an increase of B/H_I from 1.0 to 8.0. The results of these coefficients also indicate the dependency of wave reduction and reflection on fence thickness. The larger the thickness, the more wave damping.

However, data points of this case for relations K_R and $K_T - B/H_I$ are more scattered than the staggered cases for B/H_I from 8 to 16. This is because these relations are in different group of H_I/d. Note that the H_I/d is larger than 0.40 for all scaling cases (Sca.01 to Sca.12) and is below 0.3 for all validation cases (Val.01 to Val.09). In Figure 3.14b, about 40% damping of small waves in $H_I/d < 0.25$ have occurred in inhomogeneous cases (see Figure 3.13), while waves in $H_I/d > 0.25$ for inhomogeneous cases and $H_I/d > 0.42$ for staggered cases are damped with more than 50%. Within the same range of B/H_I from 8 to 16, the K_T values of inhomogeneous cases are significantly higher than staggered cases, e.g., about 0.5 compared to 0.2, respectively. In Figure 3.14c, the dissipation coefficients of all cases seem to be independent of porosity, as result points to converging

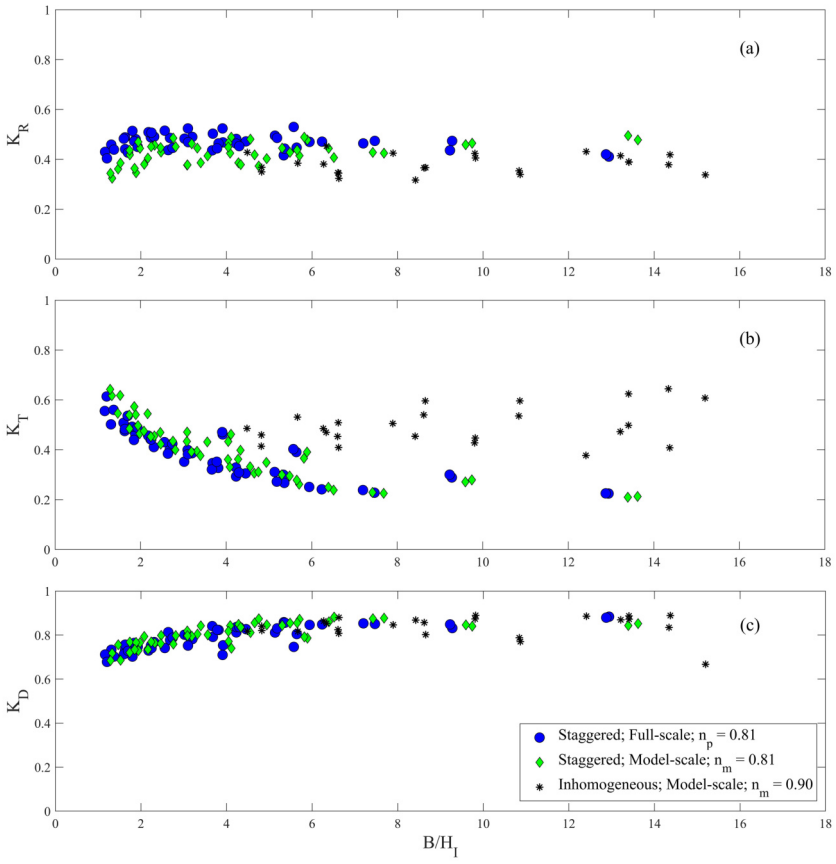

Figure 3.14: Plots of reflection, transmission, and dissipation coefficients against B/H_I.

within the range of B/H_I. The range of a transmission coefficient (K_T) from 0.2 to 0.7 is similar to the previous findings, i.e., Albers, San and Schmitt (2013); Schmitt et al. (2013). The reflection coefficients (K_T) from 0.2 to 0.4 only can be compared with the finding of Thieu Quang and Mai Trong (2020). The merged transmission coefficient in Figure 3.14b might indicate the dependency of K_T on H_I/d beside the B/H_I.

3.4 Discussion

In the SWASH model, it is impossible to explicitly represent the configuration of branches (cylinders), usually characterized by an inhomogeneous arrangement in the field. The inhomogeneous parts have varying space between the branches, which also have different shapes and sizes. This configuration influences the drag forces corresponding to wave damping inside the structure (Dao et al., 2020). The $\overline{C_D}$ value is normally high in the laminar flow regime, $Re_n < 1000$, and lower in the turbulent flow, $Re_n > 1000$ (Dao

et al., 2020). Thus, the amount of wave damping by the drag is parameterized by the bulk drag coefficient $\overline{C_D}$. This is a simple input parameter. Moreover, the cylinder diameter (D), and number of cylinders per area (N_c) should also be precisely defined, as in nature the branches gave a distribution of different sizes. Thus, with a careful definition of the characteristic value of the diameter, the drag coefficient is the main element for wave damping to parameterize the different arrangements of the cylinders of the inner parts.

The bulk drag coefficient is influenced by the scale effects of wooden fences when the laminar and turbulent effects occur for different sizes of materials and arrangements of a wooden fence. Under the laminar condition, normally $Re_n < 1000$, $\overline{C_D}$ values are high due to the high reduction of flow velocity at the upstream cylinders (Dao et al., 2020). If the model is scaled up, wave-flow conditions might become turbulent. In Figure 3.6, $\overline{C_D}$ is about 2.6 at $Re_n < 1200$ for small scale (red circles), while $\overline{C_D}$ is about 2.0 at $Re_n > 10^4$ for full scale (blue diamond). Due to the similar wave reduction, as was presented in Figure 3.14b, the scale effects were considered through the use of a Reynolds-dependent $\overline{C_D}$ value.

Scale effects come from aspects of resistance scaling which represent the resistance of fluid, for instance, the viscosity of the fluid and the bed friction. In theory, the influence of both viscosity and bed friction in the small-scale model is normally higher than that in the large-scale model. Therefore, by keeping the viscosity value the same in the full-scale model as in the laboratory condition in the physical model, its relative influence decreases if scaling up, as the momentum in the waves increases significantly. The bed-friction value should be theoretically increased with a factor of $N_L^{1/6}$ and could be increased up to the maximum geometrical similarity ratio N_L (the length-scale) due to scaling up the model if including the viscosity of the fluid (Hughes, 1993). Also, Hughes (1993) states that the effects of bed friction on wave propagation processes could play a major role if the N_L is much larger than 40. The unchanged viscosity might lead to the decrease of the bed friction for full-scale runs with a factor of $N_L^{1/6}$ which resulted in about 0.0145. In this study, the viscosity of fluid and bed friction were accounted for in all numerical simulations, which are based on laboratory conditions (see section 3.2.4). In the numerical results shown in Figures 3.11a and 3.11b, wave heights of full-scale are slightly greater than small-scales results, particularly in the shallowest water depth. This difference indicates a dependency of small-scale wave dissipation on bed friction rather than full-scale waves. Thus, the scale effects might be greater than the bed friction effects for the shallowest water depth.

To investigate the scale effects, the power regressions of two scales between K_R, K_T, and K_D and B/H_I of all staggered cases (Sca.01 to Sca.12, Table 3.3) with the best fits $R^2 > 0.80$ are plotted in Figure 3.15. As can be seen, a small difference in K_T between two cases with 0.81 porosity for model-scale (black line) and full-scale (blue line). An average 5% difference of K_T for the model-scale is higher than the full-scale cases at $B/H_I < 5.5$. However, this difference becomes smaller and consequently merges at $B/H_I > 10$. This result indicates the scale effect might occur for the larger wave height compared to a fence thickness when models are scaled up. If the scale factor is larger, this difference

should be greater.

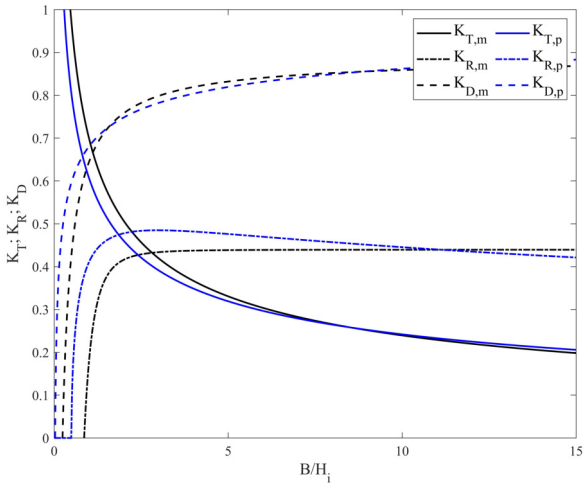

Figure 3.15: Comparison of power fits between scaling cases.

The appearance of a dike at the end of the profile (see Figure 3.2) can generate wave reflection in front of it. After a wooden fence damps the incoming waves, the transmitted wave heights can be calculated as the incident- and total-transmitted heights. However, as mentioned in section 3.2.3, the method used to calculate incident and reflection for transmitted waves is unavailable due to limited wave gauges. In the physical model, the unavailability of data leads to uncertainty if choosing the only incident transmitted wave heights to calculate the transmission coefficient. In the numerical model, this issue can be solved by neglecting the dike at the end of the profile to achieve an appropriate transmission coefficient. From an engineering perspective, even though the incident wave heights might be a correct way to calculate transmission coefficient, the total wave heights are more applicable for this study, including validation and scaling simulations.

3.5 Conclusions

In this study, the interaction between wooden fences and waves is investigated by applying the numerical model SWASH. The SWASH model used for simulating wave damping by wooden fences was firstly validated by using the bulk drag coefficient obtained from Dao et al. (2020) and the data from physical model results. The wooden fence used in the physical model contains horizontal inhomogeneous brushwood that also used in experiments by Dao et al. (2020). The needed wave data for validation, including incoming and transmission wave heights, was also obtained. Additionally, the physical results indicated the dominant influence of the inner parts and the negligible influence of the frames on wave reduction. The validation results had a good agreement with the physical results without any model tuning or calibration, indicating the bulk drag coefficient was

the key element to simulate wave reduction by the wooden fence in the SWASH model.

Furthermore, the scaling calculations were run with staggered fences that are also tested in Dao et al. (2020) for both model- and full-scale. Even though the Froude scale factor of 5.0 used in this study is significantly smaller than the literature suggested (Hughes, 1993), the scale effect has still occurred. Both reflection and transmission of model-scale waves are about 10% lower than a full-scale wave in which the difference between two scales is about 0.05 with $B/H_I < 5.5$. The scale effects are largest for the thin fence thickness and small waves. The water depth (d_m) and incoming wave heights ($H_{s,m}$) should be larger than 0.3 m and 0.15 m, respectively, to have the negligible effects of bed friction and viscosity effects inside the fence even though model effects might still have occurred.

The further scaling simulations together with the initial results of validation processes demonstrate the more the damping, the larger the wave that presented by the dimensionless parameter, H_I/d and B/H_I. This is proven by the fact that the range of about more than 70% of incoming waves are damped for cases with $H_I/d > 0.25$ for inhomogeneous fences and $H_I/d > 0.4$ for staggered fences. Moreover, the transmission coefficient is dependent on the B/H_I indicated by the reduction of this coefficient with the increase of B/H_I for all cases with $H_I/d > 0.4$. Even though, the role of relative freeboard is clearly seen, especially when water level is around the crest or lower, the effect of thickness can be more important. Meanwhile, the reflection coefficient is independent on H_I/d and B/H_I that is around 0.4 to 0.5 for all group of H_I/d and B/H_I from 3 to 16. For all scaling results, both K_T and K_R from the numerical model are also in the same range as observed in the field.

Even though the bulk drag coefficient is the most important input parameter for the numerical model, there are still several uncertainties in choosing the acceptable value for the field's wooden fence. For example, the highly irregular shape of bamboo branches and their arrangements in the field (Figure 3.1) might lead to a higher value of the bulk drag coefficient for further numerical application. For this part, future research needs to continue and contribute to this study of importance to the healthy and sustained environment of mangroves.

References

Albers, T.; San, D.C. and Schmitt, K., 2013. Shoreline Management Guidelines: Coastal Protection in the Lower Mekong Delta. *Deutsche Gesellschaft für Internationale Zusammenarbeit (GiZ) GmbH Management of Natural Resources in the Coastal Zone of Soc Trang Province*, 1, 1–124.

Anderson, M.E. and Smith, J.M., 2014. Wave attenuation by flexible, idealized salt marsh vegetation. *Coastal Engineering*, 83, 82–92. ISSN 0378-3839.

Beji, S. and Battjes, J.A., 1993. Experimental investigation of wave propagation over a bar. *Coastal Engineering*, 19(1-2), 151–162. ISSN 03783839. doi:10.1016/0378-3839(93)90022-Z.

Buckley, M.L.; Lowe, R.J.; Hansen, J.E. and Van Dongeren, A.R., 2015. Dynamics of wave setup over a steeply sloping fringing reef. *Journal of Physical Oceanography*, 45(12), 3005–3023. ISSN 0022-3670.

Chen, H.; Ni, Y.; Li, Y.; Liu, F.; Ou, S.; Su, M.; Peng, Y.; Hu, Z.; Uijttewaal, W. and Suzuki, T., 2018. Deriving vegetation drag coefficients in combined wave-current flows by calibration and direct measurement methods. *Advances in water resources*, 122, 217–227. ISSN 0309-1708.

Dalrymple, R.A.; Kirby, J.T. and Hwang, P.A., 1984. Wave diffraction due to areas of energy dissipation. *Journal of Waterway, Port, Coastal, and Ocean Engineering*, 110(1), 67–79. ISSN 0733-950X.

Dao, H.T.; Hofland, B.; Stive, M.J.F. and Mai, T., 2020. Experimental Assessment of the Flow Resistance of Coastal Wooden Fences. doi:10.3390/w12071910.

Dao, T.; Stive, M.J.F.; Hofland, B. and Mai, T., 2018. Wave Damping due to Wooden Fences along Mangrove Coasts. *Journal of Coastal Research*, pp. 1317–1327. ISSN 0749-0208. doi:10.2112/JCOASTRES-D-18-00015.1.

Del Valle, A.; Eriksson, M.; Ishizawa, O.A. and Miranda, J.J., 2020. Mangroves protect coastal economic activity from hurricanes. *Proceedings of the National Academy of Sciences*, 117(1), 265–270. ISSN 0027-8424.

Deltares, . Wave height meter. *Technical report*, Deltares, Delft.

Gagliano, S.M. and McIntire, W.G., 1968. REPORTS ON THE MEKONG RIVER DELTA. *Technical report*.

Gijón Mancheño, A.; Tas, S.A.J.; Herman, P.M.J.; Reniers, A.; Uijttewaal, W.S.J. and Winterwerp, J.C., 2017. Wave attenuation by brushwood dams in a mud-mangrove coast. *INTERCOH 2017*.

Heller, V., 2011. Scale effects in physical hydraulic engineering models. *Journal of Hydraulic Research*, 49(3), 293–306. ISSN 0022-1686.

Hoang, V.H. and Nguyen, H.N., 2006. Result on study of wave field on Dong Nai, Sai Gon estuaries and suggestion of sea bank and river mouth protection methods. *In: Vietnam-Japan Estuary Workshop in collaboration between Tohoku University and Water Resources University*. pp. 140–150.

Hu, Z.; Suzuki, T.; Zitman, T.; Uittewaal, W. and Stive, M., 2014. Laboratory study on wave dissipation by vegetation in combined current–wave flow. *Coastal Engineering*, 88, 131–142. ISSN 0378-3839.

Hughes, S.A., 1993. *Physical models and laboratory techniques in coastal engineering*, volume 7. World Scientific.

Keulegan, G.H. and Carpenter, L.H., 1958. Forces on Cylinders and Plates in an Oscillating Fluid. 60(5).

Mai, S., 1999. Interaction of Foreland Structures with Waves. *In: XXVIII IAHR Congress, Graz*. pp. 1–7.

Mendez, F.J. and Losada, I.J., 2004. An empirical model to estimate the propagation of random breaking and nonbreaking waves over vegetation fields. *Coastal Engineering*, 51(2), 103–118. ISSN 0378-3839.

Morison, J.R.; Johnson, J.W. and Schaaf, S.A., 1950. The Force Exerted by Surface Waves on Piles. *Journal of Petroleum Technology*, 2(05), 149–154. ISSN 0149-2136. doi:10.2118/950149-G.

Ngo, A.; Mai, T. and Mai, C., 2018. Wave reduction by a bamboo fence. *In: International Symposium on Lowland Technology (ISLT 2018)*. Hanoi, Vietnam.

Nguyen, V.L.; Ta, T.K.O. and Tateishi, M., 2000. Late Holocene depositional environments and coastal evolution of the Mekong River Delta, Southern Vietnam. *Journal of Asian Earth Sciences*, 18(4), 427–439. ISSN 1367-9120.

Novák, P. and Čábelka, J., 1981. *Models in hydraulic engineering: Physical principles and design applications*, volume 4. Pitman Publishing.

Ozeren, Y.; Wren, D.G. and Wu, W., 2013. Experimental investigation of wave attenuation through model and live vegetation. *Journal of Waterway, Port, Coastal, and Ocean Engineering*, 140(5), 4014019. ISSN 0733-950X.

Phan, K.L.; Stive, M.J.F.; Zijlema, M.; Truong, H.S. and Aarninkhof, S.G.J., 2019. The effects of wave non-linearity on wave attenuation by vegetation. *Coastal Engineering*, 147, 63–74. ISSN 0378-3839.

Phan, L.K.; van Thiel de Vries, J.S.M. and Stive, M.J.F., 2014. Coastal Mangrove Squeeze in the Mekong Delta. *Journal of Coastal Research*, pp. 233–243. ISSN 0749-0208. doi:10.2112/JCOASTRES-D-14-00049.1.

Reis, R.A.; Pires-Silva, A.A.; Fortes, C.J. and Suzuki, T., 2020. Experiences with SWASH on modelling wave propagation over vegetation. *Journal of Integrated Coastal Zone Management; Vol 20 No 2 (2020): Coastal Zones Volume I.*

Roelvink, J.A. and Stive, M.J.F., 1989. Bar-generating cross-shore flow mechanisms on a beach. *Journal of Geophysical Research: Oceans*, 94(C4), 4785–4800. ISSN 2156-2202.

Sayah, S. and Schleiss, A., 2006. Efficiency of brushwood fences in shore protection against wind-wave induced erosion. *Technical report*.

Schmitt, K. and Albers, T., 2014. *Area Coastal Protection and the Use of Bamboo Breakwaters in the Mekong Delta*. Elsevier Inc. doi:10.1016/B978-0-12-800007-6.00005-8.

Schmitt, K.; Albers, T.; Pham, T.T. and Dinh, S.C., 2013. Site-specific and integrated adaptation to climate change in the coastal mangrove zone of Soc Trang Province, Viet Nam. *Journal of Coastal Conservation*, 17(3), 545–558. ISSN 1400-0350.

Smit, P.; Zijlema, M. and Stelling, G., 2013. Depth-induced wave breaking in a non-hydrostatic, near-shore wave model. *Coastal Engineering*, 76, 1–16. ISSN 03783839. doi:10.1016/j.coastaleng.2013.01.008.

Suzuki, T.; Hu, Z.; Kumada, K.; Phan, L.K. and Zijlema, M., 2019. Non-hydrostatic modeling of drag, inertia and porous effects in wave propagation over dense vegetation fields. *Coastal Engineering*. ISSN 0378-3839.

Ta, T.K.O.; Nguyen, V.L.; Tateishi, M.; Kobayashi, I.; Saito, Y. and Nakamura, T., 2002. Sediment facies and Late Holocene progradation of the Mekong River Delta in Bentre Province, southern Vietnam: an example of evolution from a tide-dominated to a tide- and wave-dominated delta. *Sedimentary Geology*, 152(3), 313–325. ISSN 0037-0738.

Tanino, Y. and Nepf, H.M., 2008. Laboratory investigation of mean drag in a random array of rigid, emergent cylinders. *Journal of Hydraulic Engineering*, 134(1), 34–41. ISSN 0733-9429.

Thieu Quang, T. and Mai Trong, L., 2020. Monsoon wave transmission at bamboo fences protecting mangroves in the lower mekong delta. *Applied Ocean Research*, 101, 102259. ISSN 0141-1187. doi:https://doi.org/10.1016/j.apor.2020.102259.

Thornton, E.B. and Calhoun, R.J., 1972. Spectral resolution of breakwater reflected waves. *Journal of Waterways, Harbors & Coast Eng Div*, 98(9318 Proceeding).

Tsai, C.P.; Chen, H.B.; Hwung, H.H. and Huang, M.J., 2005. Examination of empirical formulas for wave shoaling and breaking on steep slopes. *Ocean Engineering*, 32(3-4), 469–483. ISSN 0029-8018.

Van Cuong, C.; Brown, S.; To, H.H. and Hockings, M., 2015. Using Melaleuca fences as soft coastal engineering for mangrove restoration in Kien Giang, Vietnam. *Ecological Engineering*, 81, 256–265. ISSN 09258574. doi:10.1016/j.ecoleng.2015.04.031.

Wolanski, E.; Huan, N.N.; Nhan, N.H. and Thuy, N.N., 1996. Fine-sediment dynamics in the Mekong River estuary, Vietnam. *Estuarine, Coastal and Shelf Science*, 43(5), 565–582. ISSN 0272-7714.

Zelt, J.A. and Skjelbreia, J.E., 1993. Estimating incident and reflected wave fields using an arbitrary number of wave gauges. *In: Coastal Engineering 1992*, pp. 777–789.

Zijlema, M., 2012. Modelling wave transformation across a fringing reef using SWASH. *In: ICCE 2012: Proceedings of the 33rd International Conference on Coastal Engineering, Santander, Spain, 1-6 July 2012*. Coastal Engineering Research Council.

Zijlema, M.; Stelling, G. and Smit, P., 2011. SWASH: An operational public domain code for simulating wave fields and rapidly varied flows in coastal waters. *Coastal Engineering*, 58(10), 992–1012. ISSN 0378-3839.

Chapter 4

Wave damping due to wooden fences along mangrove coasts

Success in management requires learning as fast as the world is changing.

Warren Bennis

In the Mekong Delta, as in many other mangrove settings, wooden fences are considered as beneficial coastal structures to provide sheltering for mangrove re-plantation efforts by reducing waves and currents and promoting sedimentation. One of the most quantitative previous studies on fence-induced wave reduction offered a first understanding of relevant process parameters. The present application of the advanced numerical time-domain wave model SWASH increases this understanding substantially and explains previously unexplained phenomena that were encountered in this earlier study. The findings reveal that wave damping increases with increasing fence thickness and with increasing density of the woody material in the fences. It further shows that the transmitted wave height (represented by the transmission coefficient) is inversely proportional to the Ursell number, implying that nonlinear waves are damped more effectively.

This chapter was published in Journal of Coastal Research, Volume 34, Issue 6, pages 1317–1327. Tung Dao, Marcel J.F. Stive, Bas Hofland, and Tri Mai (2018). Wave damping due to wooden fences along mangrove coasts.

4.1 Introduction

The Mekong River runs through five countries before reaching Vietnam, where it eventually bifurcates into nine river outlets, although presently only eight are left. It not only covers an area of 39,000 km^2 but also is home to nearly 17 million inhabitants in Southern Vietnam. Because erosion phenomena and mangrove losses have occurred at various locations along the Mekong Delta coast for the past few decades, many coastal structures, as well as coastal integrated management plans have been built to provide coastal protection. Examples of coastal defences along the coast are illustrated in Figure 4.1B.

Mangrove forests play a major role as coastal defenses given their capacity to dissipate waves and currents and to trap sediments and nutrients. The relevant hydrodynamic processes that are often described in the literature are waves and tidal flow. The capacity of mangrove forests to dissipate wave energy from storm surges and tsunamis is widely reported, e.g., Alongi (2008); Danielsen et al. (2005); Othman (1994); Phan et al. (2014). The roots, trunks and submerged canopies obstruct the orbital motion of the water particles hindering the penetration of wave energy in the mangroves forests. Thus, a denser mangrove forest provides, a larger wave energy attenuation. The high friction generated by a mangrove fringe also causes a reduction of alongshore tidal flows, resulting in a net input of sediment inside a mangrove fringe , e.g., Truong et al. (2017); Wattayakorn et al. (1990).

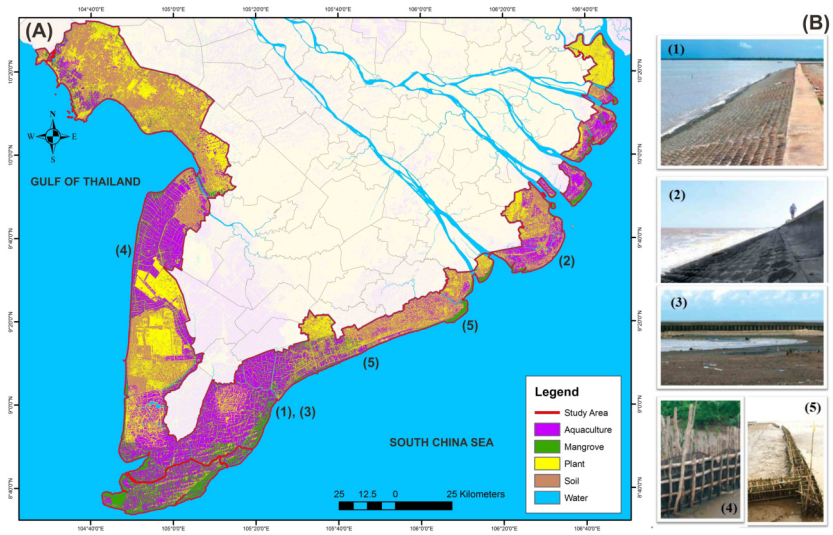

Figure 4.1: Categories of land-use in the Mekong deltaic coast in 2015 (Phan, 2016). (B). Distribution of coastal defences along Mekong Delta Coast. (1) and (2): Revetments at Ganh Hao, Bac Lieu Province (Photo by GIZ Bac Lieu, 2013) and Tra Vinh Province (Photo by Phuong Duong Thuy), respectively. (3): Seawall at Ganh Hao, Bac Lieu Province (Photo by GIZ Bac Lieu). (4) Melaleuca barriers in Kien Giang province (Brown et al., 2012) (Photo by GIZ Kien Giang). (5) Bamboo fence at Nha Mat in Bac Lieu Province and Vinh Tan Commune, Soc Trang Province (Photo by Hoang Tung Dao, 2016).

Unfortunately, a significant reduction of mangrove area has been observed in Southern Vietnam, causing severe erosion along the Mekong Delta Coast. During the Vietnam War (1962-1971), 40% of mangrove forests were eradicated (Hong and San, 1993), of which nearly 120,000 ha of about 600,000 ha of entire mangrove-forest regions were lost due to defoliant use. With both natural regeneration and manual planning, mangrove forests had recovered gradually in 1975. However, timber over exploitation for charcoal and construction, and conversion of forest into land-use and aquaculture shrimp ponds again destroyed almost 50% of mangrove forests during the period 1980 to 2006, e.g., Christensen et al. (2008); Hong and San (1993); Joffre and Schmitt (2010); Nguyen et al. (2013). For example, the majority of original mangrove lands was transformed into aquaculture land in 2015 along Mekong Delta coast (Figure 4.1A). According to Duke et al. (2010), total 30 km of the mainland coast in Kien Giang province was active and severe erosion from 2009 to 2010 leading to serious issues such that around 25 m of coastline in Hon Dat district retreated and 8 km of earthen dikes partially eroded.

In order to protect valuable land from erosion, many coastal protection projects have been undertaken along the Mekong Delta Coast (Figure 4.1B). A conventional Vietnamese approach to prevent storm surge, storm erosion as well as chronic erosion, has long been to build solid structures, such as revetments (Figure 4.1B: 1, 2), and seawalls (Figure 4.1B: 3). However, from a coastal engineering perspective, it is not only technically challenging and cost-intensive to apply such structures (Schmitt and Albers, 2014), but they might also negatively impact on the sediment budget of the coast. Alternatively, salt marshes combined with soft protection elements, such as brushwood and wooden poles (Figure 4.1B: 4, 5), could be considered instead of, or complementary to hard structures to protect erosive coastlines. Soft coastal defences, for example, have been applied since the 13^{th} century along European estuarine and lagoon coasts. During the 13^{th} and 14^{th} century, severe storm surges caused massive land losses, but farmers living along the coast gradually reclaimed land losses by using accretion techniques such as digging drainage ditches and building small dams in the early 16^{th} century (Bakker et al., 2002). The purpose of land reclamations for agricultural cultivation continued until the 1940s to 1960s (Schmitt and Albers, 2014). After this, both the governments of Germany and Netherlands took responsibility for land accretion promoting sedimentation in brushwood fenced tidal flat areas for safety against flooding (Dijkema, 1983). Present brushwood fencing in mangrove replantation projects is the mangrove counterpart of salt marsh recruitment, like the Dutch *kwelders* where brushwood fences have been used for ages to stimulate sedimentation. To stimulate the implementation of soft protection methods in the context of the Mekong Delta GIZ (Deutsche Gesellschaft $f\ddot{u}r$ Internationale Zusammenarbeit) sponsored two projects in the period 2008-2014, *viz.* "Management of Natural Resources in the Coastal Zone of Soc Trang province, Vietnam" and "Mangrove Rehabilitation in the Mekong Delta".

4.1.1 Hydrodynamics of the Mekong Delta coast

The Mekong Delta coastal environment is historically classified as a tide-dominated environment, however, waves are increasingly becoming more effective than the tide (Ta

et al., 2002). In the region of the South China Sea, also known as the East Sea, the tide has a semidiurnal character ranging from more than 2.0 m at neap tide to 4.0 m at spring tide. Along the coast, the tidal range reduces toward Ca Mau Cape and the number of tidal days as well as the diurnal characteristics increase (Phan et al., 2014). According to Hoang and Nguyen (2006), the northeast monsoon is dominating in the winter (from November to April), and the southwest monsoon is dominant in the summer (from May to October). In the southwest monsoon, the average significant wave heights ($H_{s,av}$), are lower than 5.0 m (Figure 4.2a), and the average wave peak periods ($T_{p,av}$) are 6.0 seconds (Figure 4.2b). Meanwhile, maximum significant wave heights and peak periods ($H_{s,max}$, $T_{p,max}$) correspond to 10.5 m and 11.5 seconds in the northeast monsoon (Figure 4.2).

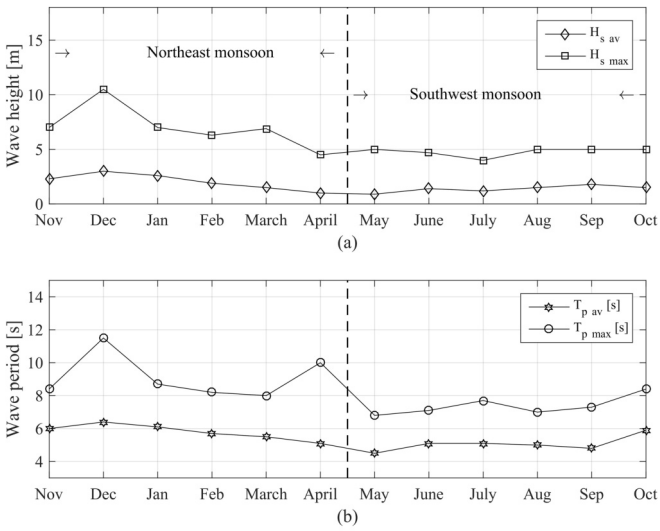

Figure 4.2: Monthly offshore wave characteristics at Bach Ho station (150 km offshore from East side of Mekong Delta coast, Figure 4.1A). Wave heights and periods were collected from 1986 to 2000 (Hoang and Nguyen, 2006).

The east of Mekong Delta coast, Soc Trang coast, in particular, is a special coast with extremely gentle sloping foreshores (1/30,000) (Phan et al., 2014). Therefore, even though waves from offshore can be large, this particular gentle and shallow foreshore causes a strong dissipation of the wave heights during wave propagation towards the shore due to breaking processes. Short waves with a frequency related to the primary wind waves lose substantial energy, while longer waves, such as swells and infra-gravity waves, are dissipated more slowly and can even exceed the short wave heights in the nearshore (Phan et al., 2014).

4.1.2 Literature review

Many studies have been carried out to investigate wave interaction with porous structures using numerical and physical models (Harada et al., 2002; Sollitt and Cross, 1972). The initial waves seaward of a porous structure are composed of incident and reflected waves due to the interaction with the structure face. A small amount of wave energy will be lost because of breaking and dissipation inside the structure, and the remaining energy will be transmitted beyond the porous structure (Sollitt and Cross, 1972). Karim et al. (2004) conclude for vertical structures that the amount of reflected and transmitted wave height depends on structure width and porosity, respectively. However, above studies consider small scale experiments and a vertical orientation of the branches in the fence structure. The following will focus on studies of wave reduction due to porous fences using a particular material, such as melaleuca and bamboo, which is applied with a horizontal orientation.

Halide et al. (2004) studied wave attenuation in vertical bamboo cylinder fields with widths varying from 15 to 90 m, as wave attenuator to protect mangrove forests. These authors used a numerical model to demonstrate the degree of wave dissipation within bamboo fields having of a spatial density of 1, 2, and 4 cylinders per m^2 and a bamboo diameter of 2, 4, and 8 cm resulting in a porosity ranging from 90% to 96%. Their numerical model results confirmed the physical expectation that the larger the diameter and the denser the bamboo density, the larger the wave attenuation. These authors concluded that a bamboo field of 90 m with a spatial density of one pole of 4 cm diameter per one m^2 was needed to achieve 50% incident wave attenuation. Interestingly, these authors scaled the spatial wave attenuation with the wavelength. However, the broader validity of this scaling was not explored.

Van Cuong et al. (2015) proposed applying a local wooden material melaleuca, used for housing and furniture, in fences as soft wave barriers. The purpose of these fences is to protect and increase sedimentation for young mangrove replantation along erosive shorelines in Kien Giang Province (Figure 4.1B: 4). The fences are assumed to decrease wave energy and thereby promote sedimentation of finer sediments and mud. Two designs were studied in situ. The basic design used a wave barrier fence 60 m offshore from the shoreline, consisting of two rows of Melaleuca poles and bunches of tree branches and small diameter poles in between a 0.5 m gap. The other extended design used additional silt traps 20 m offshore the coastline, which consisted of bamboo mats and fine fishing nets overlying the seabed to increase sediment accretion rates. Whereas the impact of the melaleuca fences on sedimentation and survival of mangroves was indicated in detail, Van Cuong et al. (2015) only mentioned that the Melaleuca fence immediately damped 56% of the incoming wave height. Three years observation from 2009 to 2012 revealed significant mud accumulation in newly established mangrove seedling fields. The mud deposition inside the fenced areas increased significantly by 0.44 m and 0.42 m in the basic design and the extended design, respectively. Unfortunately, there was no convincing evidence of wave data-sets presented for wave reduction findings.

Interestingly, the strength and flexibility of bamboo and melaleuca differ distinc-

tively. In developing countries bamboo is used for household items, and transport structures such as housing and bridges. From a coastal engineering point of view, the relatively cheap material bamboo has been shown to have superior strength and durability under strong wave conditions (Okubo et al., 2004), while melaleuca can be destroyed easily under the same conditions. Research by Schmitt et al. (2013) and Albers et al. (2013) describes a site-specific approach for mangrove rehabilitation and replantation in combination with bamboo breakwaters (bamboo T−fences) at erosive coasts in the Soc Trang Province, Vietnam (Figure 4.1B: 5). The following discussions will concentrate on their study of wave damping through bamboo fences.

Using structures similar to the melaleuca fences, bamboo fences of two rows of vertical bamboo poles were investigated earlier in a wave flume with three main porosities of 4%, 16%, and 76% at a scale of 1 : 20 (Albers and Von Lieberman, 2011) to select the best design before deploying this at active erosion areas in the Vinh Tan Commune in Soc Trang Province. The selected design consisted of two rows of vertical 8 cm diameter bamboo poles with the flexible and stiff brushwood inserted in between the 40 to 50 cm gap of the pole rows to decrease the porosity (Figure 4.3).

Figure 4.3: Fence in the field (taken by Hoang Tung Dao, 2016), the brushwood was filled up to top of the fence at the beginning but eventually washed out because of waves and currents.

In order to investigate wave transmission through bamboo fences, wave measurements were collected in a cross-shore profile section where incident waves propagated perpendicularly to the fence in both laboratory and field experiments. Significant wave heights were collected at a distance approximately 5.0 m from the bamboo fence on both the landward and seaward side. Following the literature on wave transmission through porous breakwaters a transmission coefficient and a freeboard parameter were used to present the results. The transmission coefficient (K_T) is the ratio of transmitted wave height (H_T) and total (incoming and reflected) initial wave height (H_I):

$$K_T = \frac{H_T}{H_I} \tag{4.1}$$

The difference between incident wave height and initial wave height is discussed later in the Results section. The freeboard R_c is the distance between still water level and fence crest (see Figure. 4.4). Fences can be submerged or emerged represented by a negative or positive value of the relative freeboard respectively.

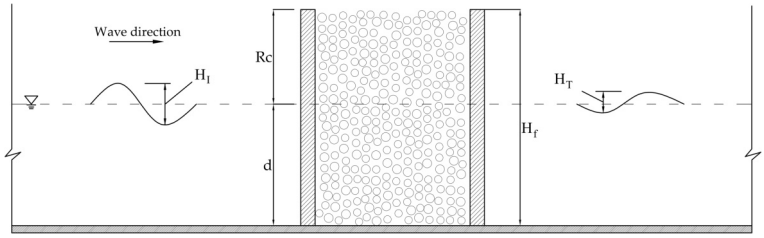

Figure 4.4: Physical modelling set-up. Where, H_T and H_I are transmitted and initial wave heights, respectively. H_f is fence height, and d is water depth.

Schmitt et al. (2013) plotted the transmission coefficient (K_T) against the relative freeboard R_c/H_I in Figure 4.5. When the fences were well submerged, with the ratio R_c/H_I ranging from −2.5 to −1.0, wave heights reduced by 25% with stiff brushwood (blue lines) and by 30% with flexible brushwood (red lines). When the fence height increased, with the ratio R_c/H_I ranging from −1.0 to 6.0, wave transmission rates decreased. For stiff brushwood the transmission coefficient decreased linearly from 0.75 to 0.55 in the range of R_c/H_I from −1.0 to 1.0. For well emerged fences ($R_c/H_I > 1$) the mean transmission coefficient was 0.55 and 0.3 for the stiff and flexible brushwood respectively. In the range R_c/H_I of 1.5 to 3.0, the wave reduction has a scatter between 35% to 55% in the case of stiff brushwood. Also, the physical modelling data (magenta diamonds) showed a larger reduction of wave height behind the fences. In the range R_c/H_I from −1.5 to −1.0, wave heights reduced almost 0% ($K_T = 1.0$). In contrast, wave heights reduced by 80% to 90% in the range R_c/H_I from 1.0 to 4.5. This is due to the relatively high density of the fences in comparison with the field (Albers et al., 2013).

Whereas a first-order representation of wave damping due to wooden fences was described by presenting wave transmission as a function of relative freeboard and brushwood density, an explanation of second order effects as suggested by the scatter clusters remained intriguingly unknown. In Figure 4.5, the scatter clusters of stiff brushwood of K_T varies over small ranges of relative freeboard, and this variation is more clearly present than in other data sets, *e.g.* flexible brushwood, and physical experiments. We hypothesize there must be other parameters such as wave nonlinearity, represented by a combination of wave steepness and relative water depth (the Ursell number, see Results section) and fence thicknesses that play a role. Although a snap-shot of the significant wave heights time series on the seaward and landward sides of the bamboo fence is presented, additional required such as wave periods are not available.

In this study, therefore, we validate and apply a numerical time-domain wave model to test the hypotheses. The hypotheses are that nonlinear waves are decreased more

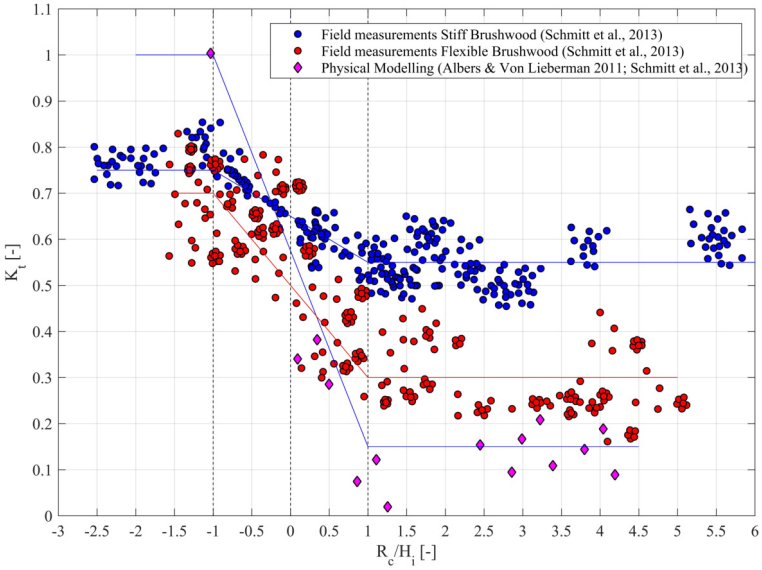

Figure 4.5: Wave transmission coefficient against relative freeboard; replotted after Schmitt et al. (2013)

effectively, and moreover, that wave transmission depends on non-dimensional fence thickness and increases with increasing relative thickness. The parameters were used to investigate these hypotheses are wave nonlinearity and fence thickness made non-dimensional by wavelength.

4.2 Methods

After the description of the study site, and the wooden fences in their local and international context, a numerical wave model is applied to investigate in more details the wave reduction due to the fences. Particularly, open source model SWASH, various input parameters and scenarios are introduced.

4.2.1 SWASH Model

SWASH is an advanced numerical, multidimensional time-domain model for simulating non-hydrostatic free-surface flow based on the nonlinear shallow water equations (Zijlema et al., 2011). SWASH can accurately account for breaking processes in the nearshore (Smit et al., 2013).

The SWASH model is used for studying wave propagation in a cross-shore profile. Hence, the governing equations are:

$$\frac{\delta u}{\delta x} + \frac{\delta w}{\delta z} = 0 \tag{4.2}$$

$$\frac{\delta \eta}{\delta t} + \frac{\delta}{\delta x}\int_{-d}^{\eta} u dz = 0 \tag{4.3}$$

$$\frac{\delta w}{\delta t} + \frac{\delta uw}{\delta x} + \frac{\delta ww}{\delta z} + \frac{1}{\rho}\frac{\delta (P_{nh})}{\delta z} + \frac{\delta \tau_{zz}}{\delta z} + \frac{\delta \tau_{zx}}{\delta x} = 0 \tag{4.4}$$

$$\frac{\delta u}{\delta t} + \frac{\delta uu}{\delta x} + \frac{\delta wu}{\delta z} + \frac{1}{\rho}\frac{\delta (P_h + P_{nh})}{\delta x} + \frac{\delta \tau_{xz}}{\delta z} + \frac{\delta \tau_{xz}}{\delta x} = 0 \tag{4.5}$$

where x is horizontal coordinate and z upward coordinate relative to the still water level. u and w are horizontal and vertical velocities, respectively. η is the surface elevation relative to the still water level, t is time. The pressure contribution P is separated into the hydrostatic pressure P_h and non-hydrostatic pressure P_{nh}. The turbulent stresses τ are calculated from a constant turbulent viscosity.

At the bottom boundary, a bottom stress is applied, following a quadratic friction law, as:

$$\tau_b = c_f \frac{U|U|}{\eta + d} \tag{4.6}$$

with U is the depth-averaged velocity; c_f is friction coefficient which is based on Manning's roughness coefficient n (Zijlema et al., 2011), presenting as

$$c_f = \frac{n^2 g}{d^{1/3}} \tag{4.7}$$

In the horizontal direction, a spatial resolution (Δx) of 0.02 m was applied, which is about 1/100 of the peak wavelength L_p. Similar to cross−shore direction, the vertical grid was set to three layers along with the Keller−box scheme (as a default setting) to increase wave dispersion accuracy (Zijlema and Stelling, 2005). A time step of 0.0001 s was employed (corresponding to a Courant number of approximately 0.3). In this study, the background viscosity was set to 3.10^{-4} m^2/s with in total three layers that accounted for all forms of resolved vertical mixing. A constant bottom friction coefficient of 0.002 was applied. Other default settings in SWASH were used as much as possible.

For fencing set-up, vegetation settings using for wave energy attenuation due to vegetation were applied. Wave energy attenuation by vegetation area is included as a drag force:

$$C_D = \frac{1}{K_v} - 1\frac{m\sqrt{\pi}}{(K_s - 1)N_v b_v \alpha H_{0,rms}} \tag{4.8}$$

where C_D, b_v, and N_v are the vegetation drag coefficient, diameter, and spatial density, respectively; σ is the wave frequency; α is the mean relative vegetation height coefficient; H_{rms} is the root-mean-square wave height (m). m is foreshore slope. K_v and K_s, presenting as Eq. 4.9 and Eq. 4.10, are the dissipation coefficient of vegetation and the shoaling coefficient following Green Law, respectively.

$$K_s = d_0^{1/4} d^{1/4} \tag{4.9}$$

$$K_v = \frac{1}{1 + \frac{2\beta H_{0,rms}}{m}(d_0^{1/4} d^{1/4} - 1}} \tag{4.10}$$

$$\beta = \frac{\alpha C_D b_v N_v}{2\sqrt{\pi}} \tag{4.11}$$

Assuming that to first order we can consider wooden fences having a similarity to rather rigid vegetation settings, representing the fence properties through three main parameters, *viz.* the mean vegetation height as fence height (H_f), vegetation diameter (D_f) and a spatial density (N_v) as a number of cylinders per m^2. Albers and Von Lieberman (2011) experiments informed the idea of using porosity in realistic fence design, but importantly, the supported data of the fences is not available, we can only assume a cross-sectional porosity of 60%, in order to receive higher ratio of wave transmission as well as avoid too much reflection. Since the porosity is applied, as the chosen density is at 1600 cylinders per m^2 and a cylinder diameter D_f of 0.01 m, we can apply various fence thicknesses (B) in the simulation from 0.4 m to 0.64 m (Table 4.1). Fence height was applied at 0.25 m to define mean vegetation height that originally described with three layers (crow, stem and root). Other parameters were set as default.

4.2.2 Input Parameters and Scenarios

The study by Phan et al. (2014) teaches that very gentle foreshore slopes create unique conditions when reaching shallow water depths at the entrance of coastal mangrove fields. The gentle slopes dissipate the short wave energy and increase the long-wave energy, such that at the entrance to the mangrove forest these energies are of the same order-of-magnitude and their negative correlation changes into a positive one (Roelvink and Stive, 1989). Unfortunately, it is virtually impossible to scale extremely gentle slopes of Mekong Delta in a wave flume, such as the one available in Delft University of Technology in which experiments are being prepared for physical tests of wave attenuation through fences. The generation of free long waves which is important on very gentle slopes is mimicked by forcing a wave train with bound long waves to break at a steep slope (Buckley et al., 2015; Smit et al., 2013; Tsai et al., 2005). Figure 4.6 describes the profile applied in SWASH at laboratory scale dimensions. At the left side, wave generation boundary condition is applied to utilizing second-order of wave theory in order to generate low-frequency waves. At the right side, a sponge layer is set to absorb all incoming waves and to avoid reflection of waves back to the fence.

Three water levels, including emerged and submerged cases, are considered. While the fence height (H_f) was held constant at 0.25 m, the different water levels create both emerged and submerged fences. Total seven fence thicknesses (B) were used. Wave periods with the range from 1.4 to 2.3 seconds are based on JONSWAP spectrum as default settings, then for each scenario, the wave height (H_{m0}) and still water level are kept constant. The input parameters are presented in Table 1, hence there are total 63 scenarios simulated.

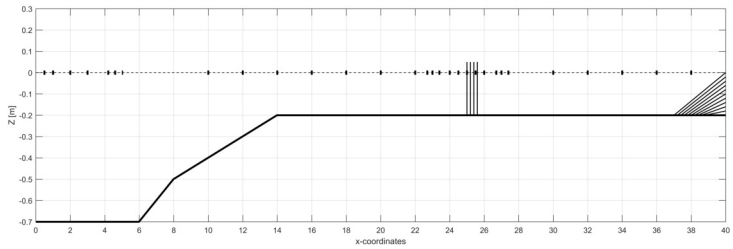

Figure 4.6: The SWASH profile presented at laboratory scale dimensions. The wave maker and wave absorber are located at $x = 0$m and $x = 37$m, respectively. The fence is located at $x = 25$m from seaward. The water level is at 0.7 m corresponding to emerged fences in deep part and is at 0.2 m in the shallow part. The crosses mark the 30 output points along the profile.

Table 4.1: Input parameters for SWASH

Deep water depth, (d) [m]			Fence thicknesses, (B_f) [m]						
0.70	0.75	0.90	0.40	0.44	0.48	0.52	0.56	0.60	0.64
Initial wave heights, H_{m0} [m]			Wave periods, (T_p) [s]						
0.03	0.06	0.08	1.4	1.6	1.7	1.8	2.0	2.1	2.3

4.3 Results

In the analysis of the simulation results, a cut-off frequency ($f_{cut-off}$) was used at 0.03 Hz to distinguish short wave frequency as $f_{sw} \geq f_{cut-off}$ and long wave frequency as $0.005 \leq f_{lw} < f_{cut-off}$. Input parameter were chosen as $H_{m0} = 0.08$ m, $T_p = 2.1$ s, $B_f = 0.6$ m for the comparison with and without a fence and for the comparison short waves and long waves. Subsequently, the effect of fences on the damping of nonlinear wave is discussed.

4.3.1 Wave damping for different freeboard

Fig. 4.7 describes the short-wave attenuation through a fence compared with the attenuation in the absence of a fence for three water levels, representing three freeboards. In general, waves start to break at $x = 15$m after shoaling in both two cases. In the case of the absence of a fence (solid line), incident short-waves heights ($H_{sw,I}$) gradually attenuate and completely dissipate at the sponge layer. With the appearance of the fences at $x = 25$ m, slights reflections occurs in front of the fence. Following Yoshimi and Yasumasa (2018) the reflection coefficient is calculated in Ep. 4.12:

$$K_R = \sqrt{(\frac{H_{s,I}}{H_{s,I0}} - 1)^2} \tag{4.12}$$

Here the incident short-wave height ($H_{sw,I}$) was calculated from the case without a fence and the (total) initial wave height ($H_{sw,I0}$), consisting both incident and reflected wave heights were calculated from the case with a fence at $x = 20$ m (so outside of the standing wave pattern). K_R was subsequently calculated for the chosen case. Reflected

wave heights were 0.013, 0.027, and 0.02 m calculating in water depth of 0.2, 0.25, and 0.4 m, respectively. Subsequently, reflection coefficients were 0.16, 0.32, and 0.24.

The evolution of the short-wave wave heights is shown in Figure 4.7. The transmitted wave height $H_{sw,T}$ decrease with the increase of water depth, for example, $H_{sw,T}$ reduces by roughly 30%, 20%, and 10% for water depths of 0.2, 0.25, and 0.4 m, respectively.

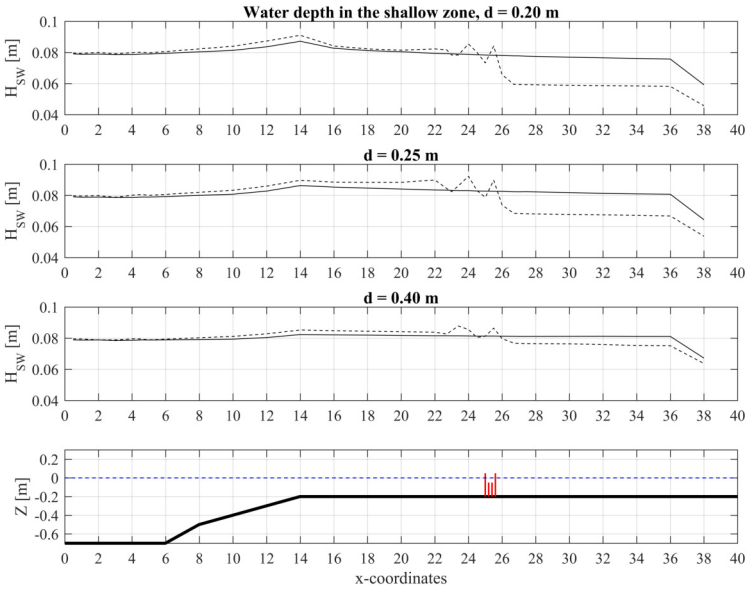

Figure 4.7: Short-wave heights attenuation without a fence (solid line) and with a fence (dash line) along the profile for three different water levels for case: $H_{m0} = 0.08$ m, $T_p = 2.1$ s, $B = 0.6$ m.

4.3.2 Effects of wave nonlinearity and fence thickness on the damping of waves

The impact of a fence on reducing short waves is most simply indicated by the transmission coefficient (K_T) as defined by Eq. 4.1. To calculate this coefficient, initial wave heights and transmitted wave heights were chosen at a location 5.0 m in front and behind the fence following Schmitt et al. (2013). It is hypothesized that the more nonlinear the waves are, the stronger the damping is. To estimate the degree of nonlinearity of the waves, the combination of wave steepness and relative water depth (Doering and Bowen, 1995) is chosen as embedded in the Ursell number as:

$$U_R = \frac{H_{m0} L_p^2}{d^3} \tag{4.13}$$

Where H_{mo} is initial significant wave height calculating by $H_{m0} = 4\sqrt{m_0}$ where m_0 is the zeroth order of moments. L_p and d are peak wavelength and water depth, respectively.

The transmission coefficient of short-waves (K_{tSW}) in different water depths is plotted against the Ursell number in Figure 4.8. As can be seen, the transmission coefficient of short−waves decreases linearly with the increase of Ursell number and relative fence thickness (B_f/L). Particularly, wave heights reduce up to 10% in the submerged case ($d = 0.4m$) with range of Ursell from 2 to 14 corresponding to B_f/L from 0.15 to 0.2. Larger wave reduction appears in emerged cases ($d = 0.2$, and $0.25m$) within higher range of Ursell number from 6 to 30 and B_f/L from 0.2 to 0.32. In general, it can be said that the wave height reduces with the increase of the Ursell number and B_f/L, for example, the highest short-wave reduction of almost 30% is reached at the highest Ursell number of 30 and at the highest range of B_f/L from 0.28 to 0.32.

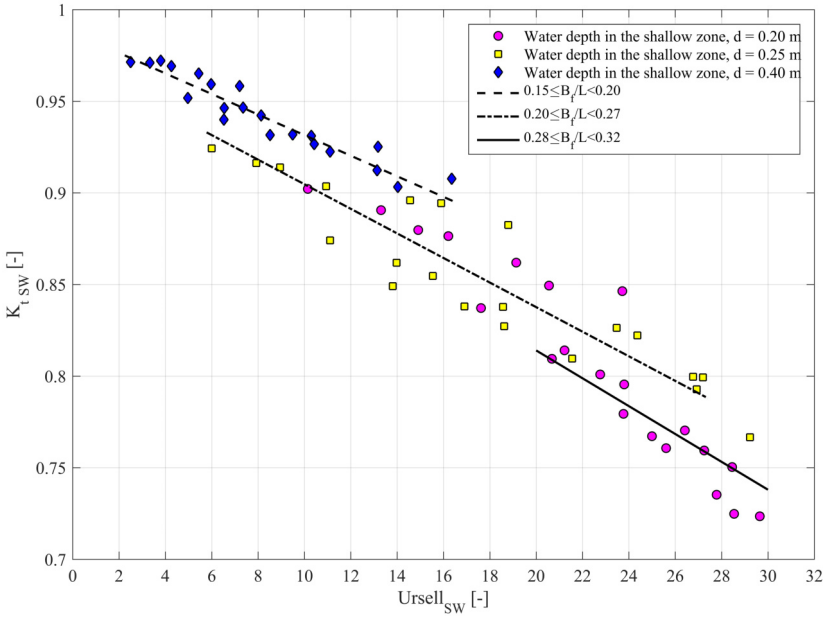

Figure 4.8: The relation of shortwave transmission coefficient and Ursell number for various classes of relative fence thickness.

A second hypothesis is that the larger the ratio of relative fence thickness B_f/L the stronger the wave damping. This hypothesis is strengthened by the grouping of the data in Figure 4.8 for B_f/L ratio ranges. By plotting the transmission coefficient against the product of Ursell Number and dimensionless fence thickness, the joint effect of both the fence thickness and nonlinearity on wave damping is revealed, suggesting a near linear correlation (Figure 4.9).

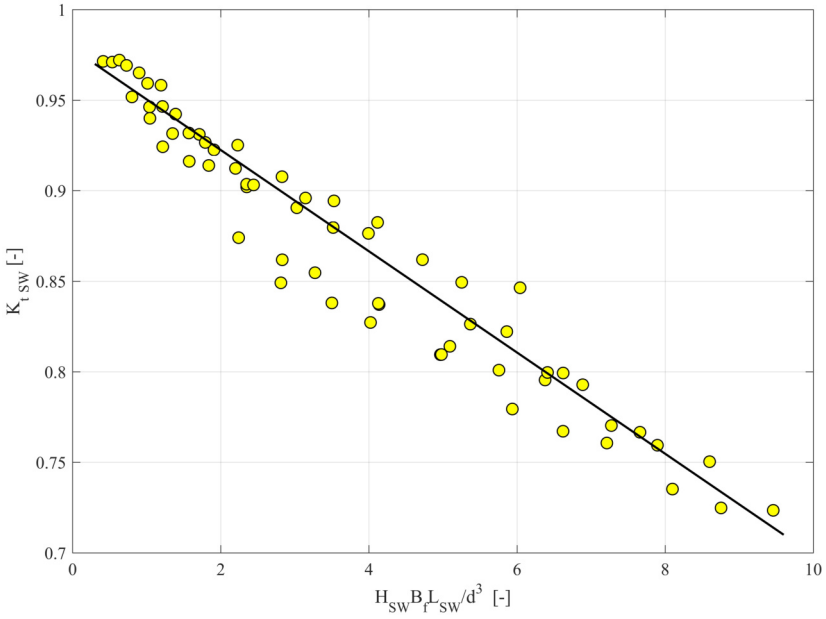

Figure 4.9: Relation of shortwave transmission coefficient and the product of Ursell number and fence thickness.

4.3.3 High-frequency and low-frequency waves transformation

Significant short-wave heights ($H_{m0,SW}$) and long-wave heights ($H_{m0,LW}$) along the profile are presented for three different water levels in Figure 4.10. In general, short waves and wave groups mostly dissipate and release free long waves from incident bound long waves after breaking (Longuet-Higgins and Stewart, 1962). Up to the breaking point at $x = 14$ m, both short waves and long waves are increasing due to shoaling and are reflected slightly in front of the fence (at $x = 25$ m). While short waves reduce 30%, 20%, and 10% corresponding to the increase of water levels from 0.20 to 0.40 m in the shallow zone, the standing long-wave height pattern increases after passing through the fence.

In conclusion, the results show that the amount of transmitted wave energy is not only affected by fence thicknesses but also by wave characteristics representing the nonlinearity degree. The more nonlinear the waves are and the larger the ratio of B_f is the higher the short-wave reduction. For example, the maximum dissipation rate is 30% corresponding to the highest degree of Ursell number and the largest ratio of $B = 0.32$. Interestingly, while the fence considerably impacts the short waves, it shows very minor effects on the long waves.

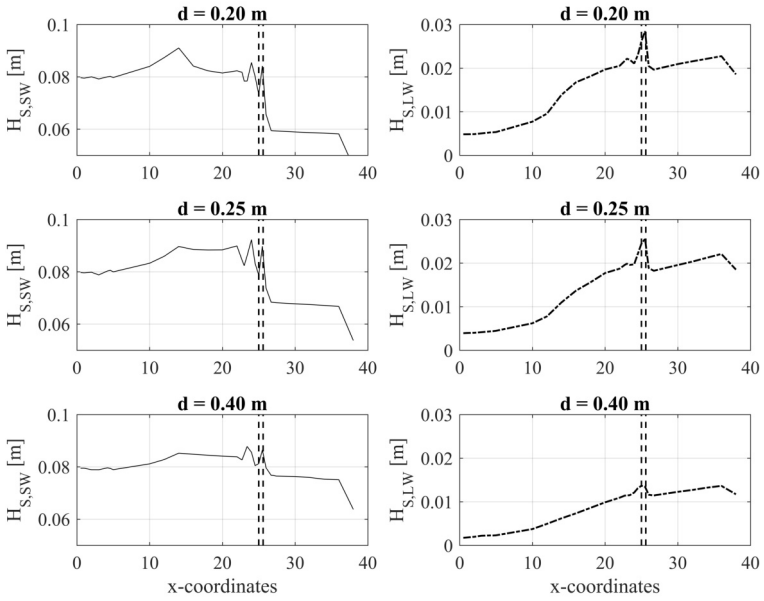

Figure 4.10: Significant short-wave heights $H_{m0,SW}$ (solid line) and long-wave heights $H_{m0,LW}$ (dash-dotted line) along the profile for three different water levels. The fence located at $x = 25$ m is presented by the dash line for the case: $H_{m0} = 0.08$ m, $T_p = 2.1$ s, $B_f = 0.6$ m

4.4 Discussion

The freeboard (R_c) was used as a main parameter to explain wave reduction behind a fence by Schmitt et al. (2013). However, the reason for the rather large scatter of the transmission coefficient remained unknown. Therefore, the computation outputs were compared to their results in Figure 4.11 in which transmission coefficients are plotted against the relative freeboards. From the simulation results (black-yellow circles), it appears that the reduction of short-wave heights increases proportionally with the decrease of water levels. Short-wave heights reduce 10% in the range of R_c/H_I of -5.5 to -1.5, in which the fence is greatly submerged. In contrast, when water levels are lower than the fence crest, the waves are more nonlinear due to shallow water effects, leading to an increase of wave reduction. This reduction increases from 5% to 30% in the range of R_c/H_I from -0.5 to 0.5, with maximum 30% wave reduction for the largest nonlinear degree with the R_c/H_I approximate 0.5. However, there is an increase of transmission coefficient from 0.75 to 0.90 in the range of R_c/H_I from 0.5 to 1.5. This is due to the fact that in the case of positive value of the freeboard smaller wave heights becomes less nonlinear leading to small reduction, i.e. $K_T = 0.7$ at $R_c/H_I = 0.5$ compares with $K_T = 0.9$ at $R_c/H_I = 1.5$.

There are matching trends between the simulation results and the Schmitt et al.

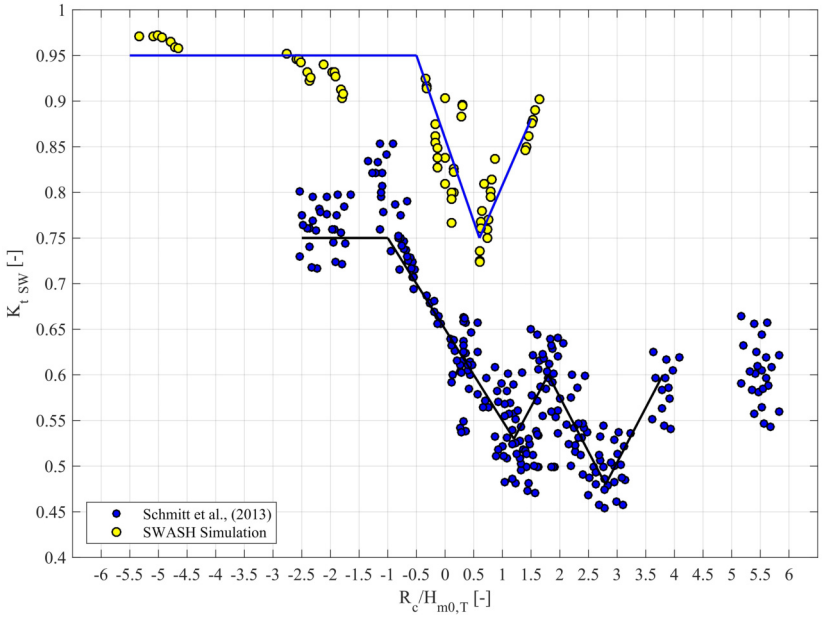

Figure 4.11: Simulation data (black−yellow circles) compared to field data for stiff brushwood (black−blue circles).

(2013) results. When the fence is greatly submerged corresponding to the range of R_c/H_I under −0.5, wave heights decrease slightly by about 10% for both the simulations and Schmitt et al. (2013) results. In the range of R_c/H_I of −1.0 to 1.0, wave reduction from both simulation and field measurement reduces steeply about 25%, *e.g.* the reduction is from 95% to 70% for the simulations and from 75% to 50% for the stiff brushwood. Then, an increase of transmission coefficient of 0.1 in the range of R_c/H_I from 0.5 to 1.5, e.g. K_T increases from 0.75 to 0.85 for the simulations and from 0.5 to 0.6 for the stiff brushwood. However, the amounts of wave reduction from the simulations are nearly 30% higher than those of Schmitt et al. (2013) most likely due to the bottom friction effect. The applied bottom friction in SWASH is much smaller than a realistic friction in the Mekong Delta. In fact, when fences are greatly submerged, the wave reduction for wave measurement is 20% more than in the simulation. It is obvious that for the emerged fence case, wave reduction in reality is still higher than in the simulation.

As mentioned in the literature review, both Van Cuong et al. (2015) and Schmitt et al. (2013) attempted to formulate a site-specific managerment approach for mangrove replantation at erosional sites. However, the role of sediment transport is not discussed. Long waves have been recognised as an important controlling factor for net sediment transport (Baldock et al., 2010). This net transport is proportional to the odd moment $\langle u|u|^2 \rangle$ (Bosboom and Stive, 2012), where u is the velocity close to the bed consisting a time-averaged velocity ($\overline{u}$), a short wave averaged oscillatory motion of short waves (u_{SW}), and low-frequency motion at wave-group scale (u_{LW}). The term u^2 is related

to the sediment concentration stirred up by the oscillatory wave motion and is proportional to the wave height in the shallow water. In the photo taken at Nha Mat in Bac Lieu Province coast during the flood (Figure 4.12), shorter waves, appearing at further offshore, were mostly obstructed by the bamboo fence placed just inshore of, while longer waves continued passing through until reaching the coast. These long waves may play a major role for a net import of sediment into the fence sited. Future work will focus on this mechanism and the role of long waves.

Figure 4.12: Wave patterns behind fence at Nha Mat in Bac Lieu Province (taken by Tung Dao, 2016). The bamboo fence is located parallel to the coast and just inshore of the building.

4.5 Conclusion

In the Mekong Delta, as in many other mangrove settings, wooden fences are considered as beneficial coastal structures to provide sheltering for mangrove replantation efforts by reducing waves and currents and promoting sedimentation. The study from Schmitt et al. (2013) reveals a wave reduction behind fences as much as 50%. Their analysis introduces the freeboard parameter R_c as a prime parameter to explain fence-induced wave reduction. However, the degree of wave nonlinearity and non-dimensional fence thickness are more important parameters for dimensionless freeboard.

The transmitted wave height decreases with the increase of the Ursell number and the relative fence thickness (B_f/L). When the Ursell number is below 16, the wave transmission coefficient varies from 0.95 to 0.90 for the range of B_f/L from 0.15 to 0.20 for submerged cases. With higher Ursell number from 16 to 30, K_T varies from 0.85 to 0.70 for the emerged cases.

Schmitt et al. (2013) use only the freeboard (R_c), as an important parameter, inspired by wave transmission over permeable structures. The present results also reveal the importance of other parameters, *i.e.* the wave nonlinearity and the relative fence thickness. In addition, fence porosity may contribute important role for wave damping. Future

work will focus on this parameter.

Fence can reduce short waves effectively, whereas they only yield a minor effect on long waves. Even though it is hypothesized that highly nonlinear waves are damped effectively, long waves are still the exception and this will be studied in future work.

References

Albers, T., San, D. C., and Schmitt, K. (2013). Shoreline Management Guidelines: Coastal Protection in the Lower Mekong Delta. *Deutsche Gesellschaft für Internationale Zusammenarbeit (GiZ) GmbH Management of Natural Resources in the Coastal Zone of Soc Trang Province*, 1:1–124.

Albers, T. and Von Lieberman, N. (2011). Current and Erosion Modelling Survey. *Deutsche Gesellschaft für Internationale Zusammenarbeit (GiZ) GmbH Management of Natural Resources in the Coastal Zone of Soc Trang Province*, 1:1–61.

Alongi, D. M. (2008). Mangrove forests: resilience, protection from tsunamis, and responses to global climate change. *Estuarine, Coastal and Shelf Science*, 76(1):1–13.

Bakker, J. P., Esselink, P., Dijkema, K. S., Van Duin, W. E., and De Jong, D. J. (2002). Restoration of salt marshes in the Netherlands. *Hydrobiologia*, 478(1-3):29–51.

Baldock, T. E., Manoonvoravong, P., and Pham, K. S. (2010). Sediment transport and beach morphodynamics induced by free long waves, bound long waves and wave groups. *Coastal Engineering*, 57(10):898–916.

Bosboom, J. and Stive, M. J. F. (2012). *Coastal Dynamics I: Lectures Notes CIE4305*. VSSD.

Brown, S., Michael, R., and Chu, C. (2012). Coastal rehabilitation and Mangrove restoration using Melaleuca fences: Practical experience from Kien Giang province. *Deutsche Gesellschaft für Internationale Zusammenarbeit (GiZ) GmbH Management of Natural Resources in the Coastal Zone of Soc Trang Province*, 1(1):1–26.

Buckley, M. L., Lowe, R. J., Hansen, J. E., and Van Dongeren, A. R. (2015). Dynamics of wave setup over a steeply sloping fringing reef. *Journal of Physical Oceanography*, 45(12):3005–3023.

Christensen, S. M., Tarp, P., and Hjortso, C. N. (2008). Mangrove forest management planning in coastal buffer and conservation zones, Vietnam: A multimethodological approach incorporating multiple stakeholders. *Ocean and Coastal Management*, 51(10):712–726.

Danielsen, F., Sorensen, M. K., Olwig, M. F., Selvam, V., Parish, F., Burgess, N. D., Hiraishi, T., Karunagaran, V. M., Rasmussen, M. S., and Hansen, L. B. (2005). The Asian tsunami: a protective role for coastal vegetation. *Science(Washington)*, 310(5748):643.

Dijkema, K. S. (1983). Use and management of mainland salt marshes and Halligen. *Flora and vegetation of the Wadden Sea islands and coastal areas. Balkema, Rotterdam*, pages 302–312.

Doering, J. C. and Bowen, A. J. (1995). Parametrization of orbital velocity asymmetries of shoaling and breaking waves using bispectral analysis. *Coastal Engineering*, 26(1-2):15–33.

Duke, N., Wilson, N., Mackenzie, J., Nguyen, H. H., and Puller, D. (2010). Assessment of Mangrove Forests, shoreline condition and feasibility for REDD in Kien Giang Province, Vietnam. *Deutsche Gesellschaft für Internationale Zusammenarbeit (GiZ) GmbH Management of Natural Resources in the Coastal Zone of Soc Trang Province*, pages 1–128.

Halide, H., Brinkman, R., and Ridd, P. (2004). Designing bamboo wave attenuators for mangrove plantations. *Indian Journal of Marine Sciences*, 33(3):220–225.

Harada, K., Imamura, F., and Hiraishi, T. (2002). Experimental Study on the Effect in Reducing Tsunami by the Coastal Permeable Structures. In *Proceedings of the International Offshore and Polar Engineering Conference*, volume 12, pages 652–658. International Society of Offshore and Polar Engineers.

Hoang, V. H. and Nguyen, H. N. (2006). Result on study of wave field on Dong Nai, Sai Gon estuaries and suggestion of sea bank and river mouth protection methods. In *Vietnam-Japan Estuary Workshop in collaboration between Tohoku University and Water Resources University*, pages 140–150.

Hong, P. N. and San, H. T. (1993). *Mangroves of Vietnam*, volume 7. Iucn.

Joffre, O. M. and Schmitt, K. (2010). Community livelihood and patterns of natural resources uses in the shrimp-farm impacted Mekong Delta. *Aquaculture Research*, 41(12):1855–1866.

Karim, M. F., Tanimoto, K., and Hieu, P. D. (2004). Simulation of wave transformation in vertical permeable structure. *International Journal of Offshore and Polar Engineering*, 14(2):89–96.

Longuet-Higgins, M. S. and Stewart, R. W. (1962). Radiation stress and mass transport in gravity waves, with application to 'surf beats'. *Journal of Fluid Mechanics*, 13(04):481–504.

Nguyen, H.-H., McAlpine, C., Pullar, D., Johansen, K., and Duke, N. C. (2013). The relationship of spatial–temporal changes in fringe mangrove extent and adjacent land-use: Case study of Kien Giang coast, Vietnam. *Ocean & coastal management*, 76:12–22.

Okubo, K., Fujii, T., and Yamamoto, Y. (2004). Development of bamboo-based polymer composites and their mechanical properties. *Composites Part A: Applied Science and Manufacturing*, 35(3):377–383.

Othman, M. A. (1994). Value of mangroves in coastal protection. *Hydrobiologia*, 285(1-3):277–282.

Phan, L. K., van Thiel de Vries, J. S. M., and Stive, M. J. F. (2014). Coastal Mangrove Squeeze in the Mekong Delta. *Journal of Coastal Research*, pages 233–243.

Phan, M. H. H. (2016). Dynamics of mangrove in lower Mekong delta.

Roelvink, J. A. and Stive, M. J. F. (1989). Bar-generating cross-shore flow mechanisms on a beach. *Journal of Geophysical Research: Oceans*, 94(C4):4785–4800.

Schmitt, K. and Albers, T. (2014). *Area Coastal Protection and the Use of Bamboo Breakwaters in the Mekong Delta*. Elsevier Inc.

Schmitt, K., Albers, T., Pham, T. T., and Dinh, S. C. (2013). Site-specific and integrated adaptation to climate change in the coastal mangrove zone of Soc Trang Province, Viet Nam. *Journal of Coastal Conservation*, 17(3):545–558.

Smit, P., Zijlema, M., and Stelling, G. (2013). Depth-induced wave breaking in a non-hydrostatic, near-shore wave model. *Coastal Engineering*, 76:1–16.

Sollitt, C. K. and Cross, R. H. (1972). Wave transmission through permeable breakwaters. *Proceedings of 13th Conference on Coastal Engineering, Vancouver, Canada, 1972*, 13.

Ta, T. K. O., Nguyen, V. L., Tateishi, M., Kobayashi, I., Saito, Y., and Nakamura, T. (2002). Sediment facies and Late Holocene progradation of the Mekong River Delta in Bentre Province, southern Vietnam: an example of evolution from a tide-dominated to a tide- and wave-dominated delta. *Sedimentary Geology*, 152(3):313–325.

Truong, S. H., Ye, Q., and Stive, M. J. F. (2017). Estuarine Mangrove Squeeze in the Mekong Delta, Vietnam. *Journal of Coastal Research*, 33(4):747–763.

Tsai, C.-P., Chen, H.-B., Hwung, H.-H., and Huang, M.-J. (2005). Examination of empirical formulas for wave shoaling and breaking on steep slopes. *Ocean Engineering*, 32(3-4):469–483.

Van Cuong, C., Brown, S., To, H. H., and Hockings, M. (2015). Using Melaleuca fences as soft coastal engineering for mangrove restoration in Kien Giang, Vietnam. *Ecological Engineering*, 81:256–265.

Wattayakorn, G., Wolanski, E., and Kjerfve, B. (1990). Mixing, trapping and outwelling in the Klong Ngao mangrove swamp, Thailand. *Estuarine, Coastal and Shelf Science*, 31(5):667–688.

Yoshimi, G. and Yasumasa, S. (2018). Estimation of Incident and Reflected Waves in Random Wave Experiments.

Zijlema, M., Stelling, G., and Smit, P. (2011). SWASH: An operational public domain code for simulating wave fields and rapidly varied flows in coastal waters. *Coastal Engineering*, 58(10):992–1012.

Zijlema, M. and Stelling, G. S. (2005). Further experiences with computing non-hydrostatic free-surface flows involving water waves. *International journal for numerical methods in fluids*, 48(2):169–197.

Chapter 5

Design consideration for brushwood fences concerning bathymetry and fence locations

The value of an idea lies in the using of it.

Thomas Edison

Wooden fences are nature-based supporting structures to restore mangroves in the Mekong Delta. The hydraulic functioning of wooden fences was studied in previous studies. However, the role of bathymetry in the evolution of waves through wooden fences has not been studied yet. Thus, in this study a numerical approach is used to find the effect of the position of fences and the foreshore bathymetry, including two particular slopes of 1/200 and 1/500, and a convex and concave shape on wave damping due to wooden fences. The results show that the bottom slope significantly influences the dissipation of incoming waves, so-called pre-dissipation, before damping by the wooden fences. Differences in pre-dissipation occur between fence locations along the cross-shore slopes. The higher pre-dissipation occurs for wooden fences closer to the land, as the depth-limited wave height at the fence reduces. The efficiency in wave damping of wooden fences is also increased as the freeboard of a fence of equal height is becoming larger for the fence located further landward. Moreover, the pre-dissipation of high and low-frequency waves is highly influenced by the bottom slope, especially on the slope of 1/500. Furthermore, the drag force on wooden fences is influenced by the bottom slopes, and is larger for the fence at the offshore side and decreases as it is moving landward. Between two slopes, the pre-dissipation of both short- and long-waves is greater on the gentler slope than on the steeper slope. Additionally, the force on the wooden fence is calculated to be higher on the steeper slope than on the gentler one. Finally, the simulations for mangroves behind the fence, introduce a highly favourable insight into possible areas for mangrove settlements, i.e. at the lee-side of the wooden fence.

Parts of this chapter was accepted in Vietnam Symposium on Advances in Offshore Engineering conference. Hoang Tung Dao, Bas Hofland, Marcel J.F. Stive, Tri Mai, and Ngo Anh (2021). Design consideration for brushwood fences concerning bathymetry and fence locations.

5.1 Introduction

Mangrove forests are the first line of coastal defence given their capacity to reduce wave heights and flow velocities in the intertidal zone between the Mean Sea water Level (MSL) and Mean High water Level (MHL) (Alongi, 2008; Duke et al., 2010). This function of mangroves increases the window of opportunity for trapping sediments and nutrients, which improves the stability of the coast and leads to a reduction of coastal erosion. However, many mangrove areas are squeezed at the nearshore due to side effects of economic development (Phan et al., 2014), such as timber exploitation for charcoal and construction, land conversion for aquaculture shrimp ponds (Christensen et al., 2008; Hong and San, 1993; Joffre and Schmitt, 2010; Nguyen et al., 2013). Also, this coastal squeeze is aggravated by sea-level rise and subsidence. Consequently, the loss of mangroves leads to severe erosion in the coastal areas, especially along the Mekong deltaic coastline. It is reported that about 30 km of coastline eroded in the period from 2009 to 2010, including the destruction of 8.0 km of earthen dikes (Duke et al., 2010). Thus, coastal structures have been constructed to protect valuable land, including hard structures, i.e., sea dikes and/or revetments, as well as nature-based solutions, such as wooden fences. Even though solid structures can surely protect the land from storm surges and inundation, they are technically challenging and cost-intensive to apply. Additionally, solid structures negatively impact sediment equilibrium of the coast (Schoonees et al., 2019) and do not easily adapt to changing natural circumstances. Given the side effects of hard structures, the combination of an original solid structure and a nature-based structure, such as a wooden fence, becomes an alternative solution to support the restoration of the coasts and the mangrove forests.

In the Mekong Delta, wooden fences are used to reduce the incoming wave energy and to increase the sedimentation rate inside the downstream basin. The wooden fences contain two to three rows of vertical bamboo poles forming a frame to store horizontal brushwood, such as bamboo branches (Albers et al., 2013; Schmitt et al., 2013; Van Cuong et al., 2015). A 50% to 80% reduction of the incoming wave heights was found at field measurements (Albers et al., 2013; Schmitt et al., 2013; Van Cuong et al., 2015) and from numerical studies (Dao et al., 2018). Due to a lack of understanding of flow over wooden fences, Dao et al. (2020) caried out experiments to indicate the friction coefficients of wooden fences, i.e., the bulk drag coefficient and the Forchheimer coefficients. The bulk coefficient is the most important parameter that is applied in the numerical model. Moreover, the interaction between waves and wooden fences was investigated through the physical and the numerical model (SWASH) mimicking the topography of the Mekong deltaic coast by a horizontal elevated bed in the previous Chapter.

The Mekong deltaic coast is characterized by a very gentle bathymetry with an average slope from 1/500 to 1/1500 (Phan et al., 2014; Tas, 2016), creating a very healthy intertidal area for mangroves to develop up to 1500 m without the presence of sea dikes and/or no human interventions (Phan, 2019, p. 82). In reality, the mangrove width reduces by up to about 100 m, due to a rate of erosion of 10 to 50 $yr.m^{-1}$ (Phan et al., 2014). The erosion also leads to a steeper slope; for example, the slope in Ganh Hao, Bac Lieu is

about 1/200 (Phan, 2019, p. 82). In other locations, such as Nha Mat, Bac Lieu, the slope is about 1/500 (Thieu Quang and Mai Trong, 2020). The context of wave attenuation inside the mangrove area on different slopes is numerically studied by K G and Bhaskaran (2017). This study concludes that a mild slope (1/80 and 1/40) is more effective for wave dissipation than a steep slope (1/20 and 1/10) when waves reach the shoreline. The difference between the two types of slope is caused by the increase of wave height reduction associated with the increase of bottom steepness, shoaling, and wave breaking inside the mangrove area. Additionally, the gentle slope in the Mekong Delta creates a strong dissipation condition for waves when reaching shallow water (Phan et al., 2014). Studies of wave attenuation inside such an extremely gentle slope, i.e., 1/200, 1/600, and 1/1000, are reported in Phan (2019). The results indicate the larger a wave height, the faster the normalized wave energy is dissipated on the steeper slope inside the mangrove forest than the higher gentle slope.

Research on observing the presence of wooden fences in front of the remaining mangroves and the role of wooden fences in damping incoming waves on different slopes before reaching the mangroves, has not yet been found in any publication. The gentle slope creates a dissipative condition for the high-frequency wave (short wave), resulting in the dominance of the low-frequency wave (long wave) (Dao et al., 2018; Phan et al., 2019, 2014). However, the aspect of short- and long-wave damping, due to wooden fences, are considered for horizontal slopes only in Dao et al. (2018). Additionally, the long wave is recognized as an important parameter that controls the net sediment transport (Baldock et al., 2010). The net sediment transport is proportional to the odd moment $\langle u|u|^2 \rangle$, where u (m/s) is the wave orbital velocity, associated to the oscillatory motion of short waves, and the low-frequency motion at a wave-group scale. The term is related to the sediment concentration which is stirred up by the oscillatory wave motion and which is proportional to wave heights in the shallow water.

Furthermore, the front-line mangroves normally suffer from wave attacks that usually force mangroves to retreat during water level variations. In the Mekong Delta, the coasts are protected by hard revetments leading to a reduction of the healthy width of mangroves (Phan et al., 2014). The wooden fences reduce incoming energy and support the front-line mangroves to resist the wave loads. Consequently, favourable conditions can be generated to promote mangrove growth. However, this content has not been considered in the previous studies, i.e., Albers et al. (2013); Ngo et al. (2018); Thieu Quang and Mai Trong (2020).

During the interaction between waves and fences, the water flow pattern is disturbed. The disturbance often leads to flow pattern changes, such as contraction of flow, the formation of lee-wake vortices and turbulence, and/or reflection and diffraction of waves (Sumer, 2002). It is noted that all the flow pattern changes are likely to influence sediment transport around the structure. The depth and width of the scouring depend on the characteristics of sediment, wave, or flow. In Figure 5.1, a local scour occurs along the fence's toes, resulting from one of the changes of flow, such as down-flow, lee-wave vortices, and/or horseshoe vortices.

Figure 5.1: Scour at wooden fence's toes (Courtesy Hoang Tung Dao, 2016).

In this Chapter, the wave damping caused by wooden fences on different slopes and in different locations is studied. Typical conditions resembling the Mekong deltaic coast are used. Besides a general wave damping, the wave-induced forces on the fence are studied. Additionally, several considerations related to wave damping function of fences due to scour, wave evolution through a fence on concave and convex profiles, and simulation for mangroves behind the fence, are evaluated. The numerical model SWASH, which is validated for wave damping in the physical model in Chapter 3, is applied for this Chapter's contents. The outline of this Chapter is as follows. Section 1 is the introduction. The methodology is presented in section 2. The results and conclusions are presented in sections 3 and 4, respectively.

5.2 Methodology

In this section, the bathymetry and wave conditions in the Mekong Delta, based on designed scenarios in the numerical model, are described. The wooden fence location impacted by bottom slopes is considered. Next, the model description and wooden fence implementation in the numerical model are presented.

5.2.1 Bathymetry and wave conditions in the Mekong Delta

The intertidal zone of the Mekong Delta is dominated by a tidal range of about 4.0 m with the MSL = 1.95 m, and MHL = 3.95 m (Gagliano and McIntire, 1968; Wolanski et al., 1996). With the gentle slope varying from 1/200 to 1/1500, the intertidal width can be increased up to 1500 m, which provides an area where healthy mangroves are able to grow. In this Chapter, two bottom slopes are used to represent the Mekong deltaic coast. The slopes of 1/200 and 1/500 are found at Nha Mat, Bac Lieu (Thieu Quang and Mai Trong, 2020), and Ganh Hao, Bac Lieu (Phan, 2019, p. 82), respectively.

Wave characteristics are obtained from the study of Tas (2016), based on the wind data at Con Dao station (Tran et al., 2004) and wave-data from the NOAA wave model (National Oceanic and Atmospheric Administration, 2014). In Table 5.1, wave conditions at a water depth of 65 m (deep water) with a return period varying from 10 to 50 years are presented. As can be seen, the wave period and the wave height increase by about 10% and 30%, respectively, for the highest return period of 50 years. Moreover, the wind set-up occurs up to 0.9 m during a storm, which increases with the decrease of the bottom slope. For the gentle slope of 1/1500, the wind set-up at the coastline increases from 0.6 to 0.9 m with the increase of a return period from 10 to 50 years (Tas, 2016). The wave height and wind set-up are obtained from their marginal distributions, but the high correlation that can be expected provides a reasonable and (slightly) safe assumption. From an engineering perspective, the higher return period for a wave condition is normally chosen for a highly safe scenario, directly related to the strength and lifetime of a structure. In this study, the wave condition with a return period of 10 year, as given in Table 5.1, is chosen as wave boundary for the numerical model. The water level is taken as MHL and with a 10-year wind set-up, which amount to assumed to be five years of this field structure. When designing for a wave condition with a 10-year return period, the probability that this situation will occur during the lifetime is 41% according to the Poisson equation. Hence, this is a condition with a high probability of occurrence, such that the fence should be able to withstand this situation.

Table 5.1: Extreme wave conditions at a water depth of 65 m obtained at Con Dao and Bach Ho station (Tas, 2016)

Return period (y)	Wave period, T_p (s)	Wave height, H_s (m)	Wind speed U_{10} (m/s)	Wind set-up (m)
10	**9.4**	**5.1**	**19.7**	**0.6**
20	9.7	5.7	21.9	0.7
25	10.0	5.9	22.6	0.8
40	10.1	6.3	24.1	0.9
50	10.4	6.5	24.8	0.9

5.2.2 Scenarios design for wooden fence

Figure 5.2 presents a particular application of wooden fences in the Mekong deltaic coast for mangrove restoration. In Figure 5.2b, wooden fences were built in parallel and in an oblique orientation to the shoreline. The parallel orientation reduces the wave energy perpendicular to the shore while the oblique fence decreases longshore flow velocity (Albers et al., 2013; Schmitt et al., 2013). Even though this combination of fences is meant to increase the sedimentation rate from the cross-shore and longshore flow, the location of fences in relation to mangroves is not mentioned in previous studies, e.g., Albers et al. (2013); Ngo et al. (2018).

In this study, an only cross-shore section is considered, where the wooden fences are installed parallel to the shore. Figure 5.3 presents a schematic profile with a wooden

Figure 5.2: Study location in Nha Mat, Bac Lieu, Can Tho, Vietnam (Google Earth, 2018).

fence installed in front of mangrove bushes/trees and in front of sea dikes. As can be seen in Figure 5.3a, if the wooden fence moves from location 1 (Fence 1) to location 2 (Fence 2), which is closer to the land, the fence height is closer to the water surface (MHL) due to the bottom slope. On the steep slope, such as 1/100 or 1/50, the wooden fence is even more visible under a high water level. In this Chapter, the wave transformation and damping at different wooden fence locations on two slopes (i.e. 1/200 and 1/500) are investigated and presented in the next section. In Figure 5.3b, concave and convex profiles are introduced which are associated to the cases with accretion and erosion, respectively. The wave transformations through wooden fences on those profile are then simulated in this Chapter.

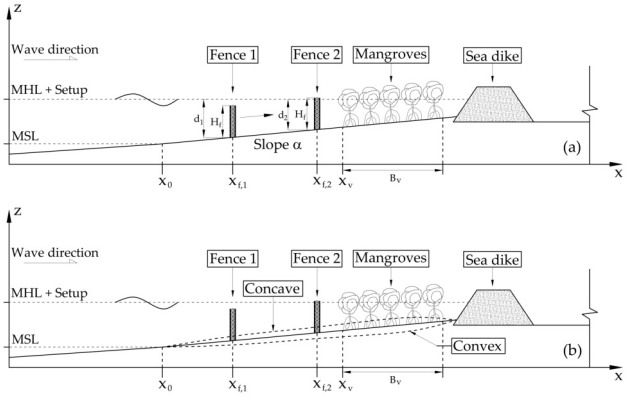

Figure 5.3: Schematic bottom slope and orientation of wooden fences and mangroves of the study case with a sea dike. (a): Wooden fences are installed further (Fence 1) and closer (Fence 2) to mangrove forests. The water depth at the fence toe is d, the subscript denotes the fence location; H_f is the fence height; B_v is the mangrove width, and α is slope parameter. (b): concave and convex profiles are presented.

5.2.3 Model description

The numerical models, SWAN and SWASH, are applied to simulate wave propagation and wave interaction with wooden fences on the Mekong deltaic coast. SWAN is a third-generation wave model and is applied for simulating wave parameters in coastal regions. This model is developed by Delft University of Technology based on the action balance equation (Booij et al., 1997, 1999). On the other hand, SWASH is a time-domain model applied for simulating non-hydrostatic and free-surface, based on non-linear shallow water equations (Zijlema et al., 2011).

Due to the lack of offshore bathymetry in the Mekong Delta, the numerical model profile is assumed to be useful from a distance from the coast about 100 km to a water depth of 50 m. In SWASH, the time consuming computational requirements for such a long distance are very high, leading to an inconvenient computation of the entire domain in SWASH. Thus, the combination of SWAN and SWASH is needed to calculate wave propagation from the offshore. Additionally, both the SWAN and SWASH model are validated and efficient to produce wave propagation from the offshore to the nearshore region (Zijlema et al., 2011). The validation of wave damping due to wooden fences, as discussed in Chapter 3, permits a confident reproduction to simulate wave-fence interaction in SWASH.

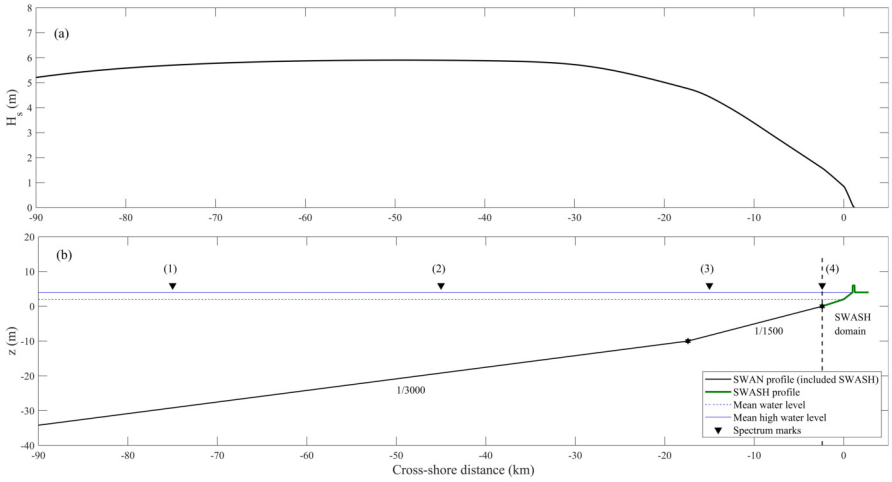

Figure 5.4: Wave transformation (top panel) and the computational domain in the SWAN model (bottom panel). The SWASH profile (green line) is defined on the right side of the dashed line in the bottom panel.

The domain of both the SWAN and SWASH models is studied in one-dimensional mode (1D) for which one cross-section perpendicular to the coastline is defined in Figure 5.4b. The length of the computational domain depends on the bottom slope. In the SWAN model, the computation domain is from z = -45.0 m to z = +6.0 m (Figure 5.4b) with a total of 108 km long. In Figure 5.4b, the cross-shore profile in the SWAN model

is separated into several bottom slopes with a cell grid of 10.0 m. Note that the profile is assumed to be fixed in every simulation. A standard JONSWAP (JOint North Sea Wave Observation Project) shape spectrum with a wave height and peak period with a return period of 10 years (see, section 5.2.1) is imposed at the left side of the profile at z = -45.0 m. The model is run with the third-generation wave model with wind input, quadruplet interaction, and linear growth (white-capping). A triad wave-wave interaction is also activated. The default bottom friction of 0.0038 is included. Figure 5.4a presents the transformation of significant wave heights from the offshore to the nearshore in the SWAN model. It is noted that offshore waves have slightly grown offshore, due to wind set-up (x = -90 km to x = -70 km). Wave heights dissipate fast, from x = -30 km to nearshore, corresponding to a water depth from about -10 to -4 m due to the bottom and shallow effects. In Figure 5.5, wave spectral densities of several locations (spectrum marks in Figure 5.4b) also show wave energy dissipation during the wave propagation to the shallow water.

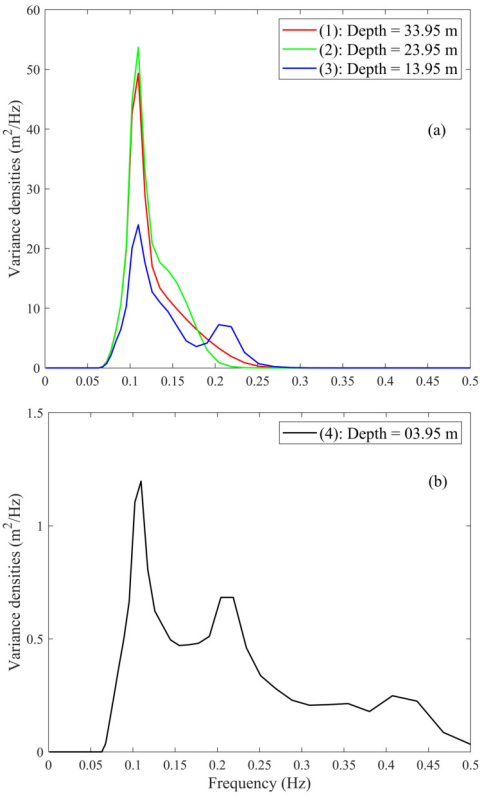

Figure 5.5: Wave spectrum at locations from offshore (location 1 to 3, top panel) to nearshore (location 4, bottom panel) as computed by SWAN. Note that water depths are included water level above MSL

The computational domain of the SWASH model is much smaller, but has a much

higher resolution than the SWAN model. The domain of SWASH is located from bottom level, MSL-2 m (x = -2.4 km) to z = +5.0 m (x = +3.0 km) with the grid size of 0.25 m. From MSL (x = 0.0 km), the bottom slopes of 1/500 as the base slope is presented in Figure 5.6. All scenarios are tested with a sea dike. The wave boundary is imposed at the offshore boundary, using the spectrum output from the SWAN model at x = -2.4 km (see Figure 5.4, bottom panel) at a water depth of 3.95 m under the MHL (blue dashed line, Figure 5.5). The wave characteristics are calculated from variance densities, including H_s = 1.45 m, T_p = 9.4 s, and d = 3.95 m. For all simulations, the vertical turbulent mixing of viscosity is set as 3×10^{-4} (m^2/s), and the bottom friction as Manning's roughness is kept as the same as in the SWAN model as 0.038. The further application and boundary conditions are described in Zijlema et al. (2011).

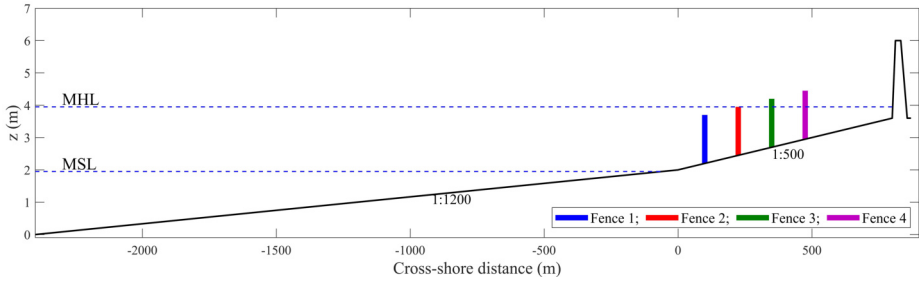

Figure 5.6: Computational domain of SWASH in the base slope of 1/500. Wooden fences are located at x_f from 100 m to 500 m.

The vegetation model in SWASH (version 6.01) is applied to simulate wooden fences. In this model, wave reduction due to an array of stiff cylinders, including horizontal and vertical cylinders, is implemented (Suzuki et al., 2019). For the fence, the brushwood is modelled by horizontal cylinders. The characteristics of a wooden fence are based on Dao et al. (2020), with a branch density (N) of 603 cylinders/m^2, a mean branch diameter (D) of 0.02 m, and a bulk drag coefficient ($\overline{C_D}$) of 2.0. One fence height (H_f) of 1.5 m is used for all simulations. One thickness (B_f) of 1.2 m is tested at each location. In Figure 5.6, several cross-shore locations of the wooden fence from the coastline (at MSL), x_f, are considered from x_f = 100 m to x_f = 475 m corresponding to water depth at the fence toe (d) that decrease from 1.75 m to 1.00 m. Moreover, a steeper slope of 1/200 is chosen to compare the wave damping with the base slopes. The wooden fences are set at the same water depth as the base slopes. As a result, the fence locations are changed due to shorter profile of steeper slope. The design cases for wooden fences of both slopes are presented in Table 5.2. The water depth at each location is remained constant resulting the constant freeboard ($R_c = H_f - d$) for two slopes.

The total body force on the fence F_D is the summary of the drag term in horizontal and vertical direction, and the inertial term applied for horizontal cylinders. Then, the local force per unit width and per cross-sectional fence area can be expressed as

$$F_D = \frac{1}{2}\rho D N \overline{C_{D,f}}(|u| + |w|) + \rho C_M A N a_u (N/m^3) \tag{5.1}$$

Table 5.2: Design scenarios for wave damping due to wooden fences

Case	x_f (m) slope 1/500	slope 1/200	water depth, d (m)	Freeboard, R_c (m)	Bottom level, z_b
1	100	40	1.75	-0.25	2.20
2	225	90	1.50	+0.00	2.45
3	350	140	1.25	+0.25	2.70
4	475	190	1.00	+0.50	2.90

where N (m^{-2}) and D (m) are the number of cylinders per area of a wooden fence and the cylinder diameter, respectively; $\overline{C_D}$ is the bulk drag coefficient, C_M is the inertia coefficient set as always as 2.0; ρ (kg/m^3) is the fluid density; A ($= \pi D^2/4$) is the area of a single-cylinder; u and w (m/s) are the depth-averaged horizontal and vertical wave orbital velocity, respectively; and a_u is the acceleration of horizontal wave orbital velocity. Note that the acceleration of the vertical wave orbital velocity can be neglected due to a small contribution to the total acceleration of wave velocity. The force on a single branch will be

$$F_{D,Branch} = \frac{F_D}{N}(N/m^3) \tag{5.2}$$

Then, the force on the total fence will be

$$F_{D,Fence} = \int_B \int_{z_b}^{R_c} F_D dz dx (N/m) \tag{5.3}$$

Figure 5.7 presents the drag force acting inside the brushwood of the wooden fence. It should be noted that only the brushwood (the inner part) is considered for simulations. In SWASH, the depth-averaged wave velocities in horizontal and vertical directions are extracted at several points within the wooden fence thickness with the horizontal resolution (Δx_f) as 0.25 m. In order to solve Equation 5.1, at each Δx_f, the velocity is used to calculate the force ΔF_D, then the total force F_D is the summary of ΔF_D from all output points.

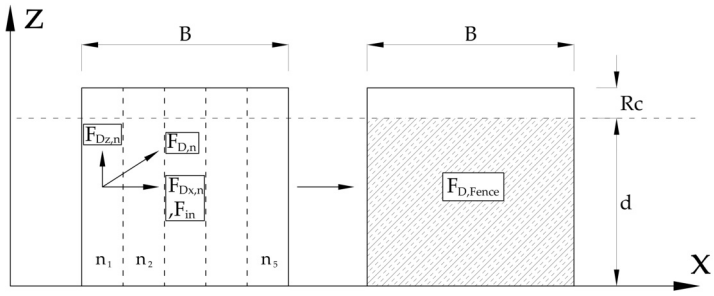

Figure 5.7: Schematic sketch of wave force on a wooden fence.

In this Chapter, the wave transformation through a wooden fence at each location is simulated for various possible configurations and for both slopes. An overview of considered cases is given in Table 5.2. The effect of bottom slopes on wave dissipation and damping due to slopes and fences then is investigated. Additionally, the effect of bottom slopes on the total drag force of wooden fences (Equation 5.1) is investigated. Furthermore, the base slope (Figure 5.6) is used for further simulations, including waves transformation through both wooden fences and vegetation (mimic mangroves) and comparison wave damping in cases with and without scours. For the combination test, a constant mangroves width (B_v) of 50 m is constructed at x_v = 225 m behind the fences. The characteristics of mangroves are the density N_v = 150 cylinders/m^2, a average diameter D_v = 0.05 m, and a bulk drag coefficient $\overline{C_{D,v}}$ = 1.0, with subscript "v" for vegetation. Only one mangrove height of 2.0 m is used. Only the horizontal force component is used in the wave damping formulation. For the scour test, a profile with a fixed scour at two fence locations, $x_{f,1}$ = 100 m and $x_{f,4}$ = 475 m, is created with a width of 0.5 m to each side of the fence and a depth of 0.3 m. A scour depth in this order of magnitude was observed in the field by the author (see Figure 5.1). Last but not least, the wave transformation through a brushwood fence on concave and convex slopes is simulated.

5.3 Results

This section presents the effect of bottom slopes on wave dissipation and damping by slopes and fences, including High-Frequency (HF) and Low-Frequency (LF) waves. Next, the total drag forces of the wooden fence at all locations and both slopes are compared and analyzed. The combination of a fence and mangrove area then is tested and analyzed. Next, the influence of the scour on fence efficiency is quantified. Also, the effect of concave and convex slopes are evaluated.

5.3.1 Effect of bottom slopes on wave damping by wooden fences

The development of the significant wave height on the cross-shore profile in relation to wooden fences at all locations on the 1:200 and 1:500 slopes is presented in Figure 5.8. Generally, the incoming wave is more dissipated on the 1:200 slope (Figure 5.8b) than on the 1:500 slope (Figure 5.8a). In Figure 5.8a, the significant wave height (H_s) at x = 95 m for the first fence position is reduced from 1.03 m to 0.91 m, to 0.78 m, and to 0.66 m on the 1:500 slope for every 125 m. The highest reduction is found at the fence that is located further landwards, mainly due to the effect of depth-induced breaking. For the steeper slopes (1/200) in Figure 5.8b, the H_s is dissipated by about 0.12 m for every 50 m, corresponding to locations of wooden fences. It is noted that the dissipation of on the steeper slope is also faster than on the gentler slope. For example, the H_s at x = 95 m reduces to 0.90 m after 135 m for the 1:200 slope (Figure 5.8b), while it needs about 300 m to have a similar value for H_s for the 1:500 slope (Figure 5.8a). Due to the fast dissipation of incoming waves, the wave damping at all locations is also different for both slopes. The higher dissipation before contacting the fence, the so-call pre-dissipation, leads to lower transmission waves for all slopes. For the 1:500 slope in Figure 5.8a, the transmitted wave heights ($H_{s,t}$) are 0.44 m (x = 110, blue line), 0.38 m (x = 265 m, red line),

0.31 m (x = 360 m, green line) and 0.26 m (x = 485 m, purple line). The $H_{s,t}$ for the 1:200 slope are slightly higher corresponding to four locations (Figure 5.8b). Interestingly, the bottom slope significantly impacts the pre-dissipation rather than the transmitted wave heights. It is due to the $H_{s,t}$ being much smaller than the water depth leading to the lower dispersion rate of transmission waves. The results indicate that the closer to wooden fences, the higher the pre-dissipation of waves.

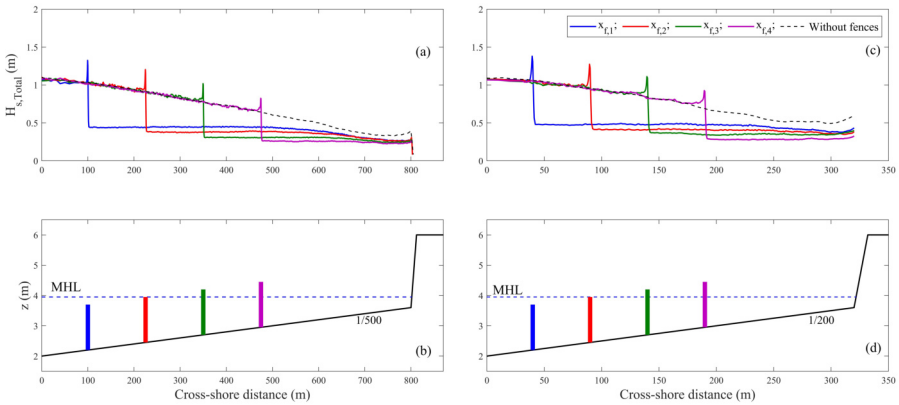

Figure 5.8: Wave evolution over wooden fences on the 1:500 (left side) and 1:200 (right side) slopes at all locations. Wave dissipation without fences (dashed line) is indicated as a reference. Wooden fences at three locations are indicated as the same color as wave heights in the bottom panel.

As wooden fences move toward the landward side, the fences have a larger freeboard (R_c) due to the bottom slopes (Figure 5.6). The increase of freeboard leads to an increase in the wave damping because less wave overtopping occurs. In Figure 5.9, the relationship between the transmission coefficient ($K_t = H_{s,t}/H_{s,i}$) and the relative freeboard ($R_c/H_{s,i}$) is presented for every fence location and all slopes. As can be seen, the K_t value decreases with the increase of $R_c/H_{s,i}$ for all slopes which reaches the lowest value, 0.37 (1:200 slope, green diamond) and 0.39 (1:500 slope, blue circle), at $R_c/H_{s,i}$ of 0.65 and 0.73, respectively. In detail, about 60% wave height can be damped by wooden fences at two last locations, x_f = 140 m and 190 m for the steeper slope (Figure 5.8c), and x_f = 350 m and 475 m for the gentler slope (Figure 5.8d). Figure 5.9 also points out that the transmission wave on the steeper slope (green diamond) is higher when fences are submerged, but it is similar to the gentler slope (blue circle) under emerged conditions. The results suggest that for the fence of a constant height, in this case, the steeper slope, the larger the wave damping. This adds to the fact that wave height at the seaward side of the fences that are placed more landward is already lower due to the larger depth-induced wave damping.

To separate HF- and LF-waves from the total waves, a cut-off frequency ($f_{cut-off}$) of 0.05 Hz was used such that the calculation of HF waves frequency was as $f_{HF} \geq f_{cut-off}$) and LF waves was $0.005 \leq f_{LF} \leq f_{cut-off}$. By moving fences on two slopes into the new

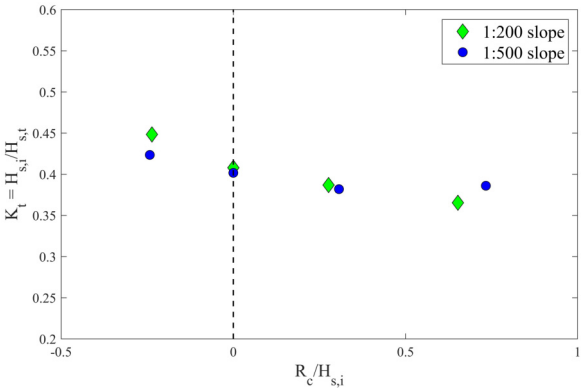

Figure 5.9: The relationship between the transmission coefficient (K_t) and relative freeboard ($R_c/H_{s,i}$) at two bottom slopes.

coordinate, the comparison of HF-waves that are transformed through wooden fences between bottom slopes 1/500 of (black solid line) and slope of 1/200 (blue dashed line) at all locations is introduced in Figure 5.10. The similar plots for LF-waves are also presented in Figure 5.11.

In Figure 5.10, the bottom slopes have significant effects on the pre-dissipation of HF-waves more than on the transmission of waves. Note that the comparison of pre-dissipation occurs at the same water depth and freeboard for each location. At the first location (Figure 5.10a), the pre-dissipation of HF-waves at a slope of 1/500 is slightly lower than at a slope of 1/200. The difference of pre-dissipation between two slopes becomes larger when fences are moved towards the landward side (Cases 4, Figure 5.10d). It is due to the fact that HF-waves propagate a longer distance on gentler slopes. As a result, a the higher dissipation of HF-waves occurs on the gentler slope than on the steeper slope. Furthermore, the lower pre-dissipation of the HF-waves leads to a larger reduction of HF-waves due to the wooden fence on the steeper slope than on the gentler slope.

On the other hand, the bottom slopes are effective on the evolution of LF-waves on the 1:500 slope (black solid line), but surprisingly hardly seem to influence the LF-waves on the 1:200 slopes (blue dashed line), as shown in Figure 5.11. The LF-wave heights are nearly matched for all slopes at the first location (Case 1, see Table 5.2), including a slight overtopping before significant reduction by the wooden fence (Figure 5.11a). However, at the last location (Figure 5.11d), the incoming LF-wave heights are reduced by about 20% compared to the first location on the 1:500 slope (black solid line) while they remain the same on the 1:200 slope (blue dashed line). Likewise, the LF-waves are reduced by over 50% of the wave heights, the same as HF-waves for both slopes. Note that the transmitted wave heights are included the reflection. The pre-dissipation and damping in Figure 5.10 and Figure 5.11 could be related to the sediment concentration that is stirred and transported by HF- and LF-waves, respectively. The stirred sediment by HF-waves was then reduced due to the reduction of pre-dissipation. At the same time, the sedi-

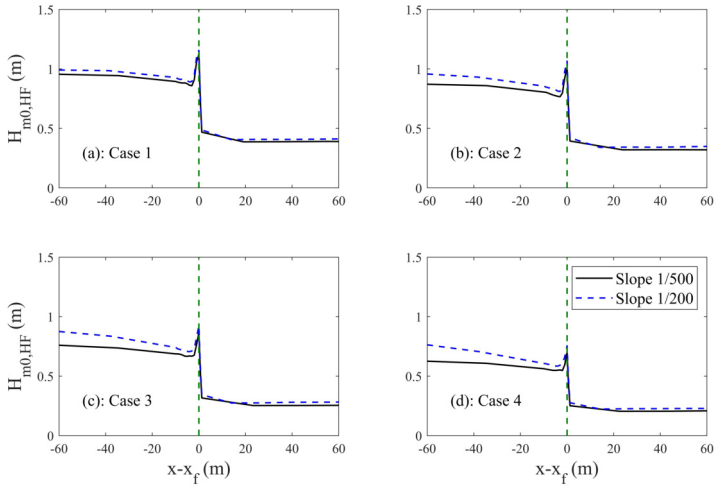

Figure 5.10: HF-wave damping by wooden fences on the slope of 1/500 (black solid line) and 1/200 (blue dashed line) at all locations. The fence location is chosen as the new coordinate. The fences are indicated as a green dashed line.

5

ment transport-associated to LF-wave motions could be settled after being significantly reduced by wooden fences. However, a location closest to the shore is considered the best location of the wooden fence to receive proper sediment transport by LF-waves that are influenced by the bottom slopes, especially the gentler slopes.

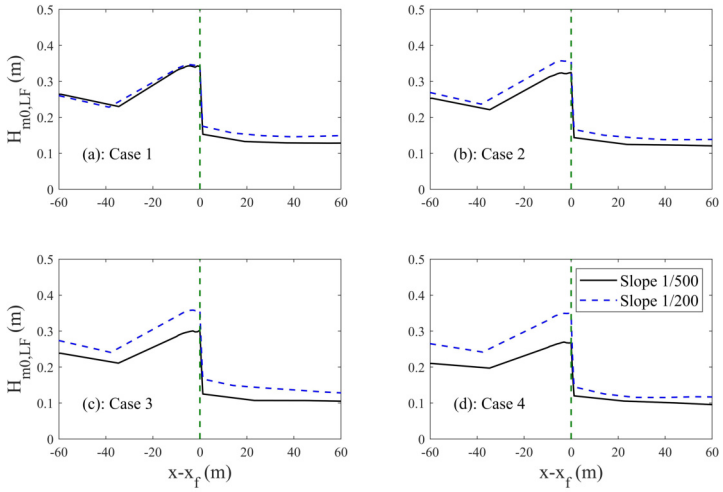

Figure 5.11: LF-wave damping by wooden fences in the slope of 1/500 (black solid line) and 1/200 (blue dashed line) at all locations. The fence location is chosen as the new coordinate. The fences are indicated as a green dashed line.

5.3.2 Effect of bottom slopes on drag forces due to wooden fences

The pre-dissipation increases with the decrease of bottom slopes resulting in a lower wave height dissipation inside the fence that is closer to the land (Figure 5.8). Therefore, the orbital wave velocity inside the fence that is located further to the land is much higher than the closer fence. Figure 5.12 compares wave heights and maximum wave velocity at all locations for slopes of 1/500 and 1/200. The maximum wave velocity is defined as the maximum amplitude of the horizontal wave orbital velocity based on the linear wave theory for a wave with significant heights. It is shown that wave velocities inside the wooden fence (between the green dashed lines) reduce with the increase of the fence's distance for all locations (Figure 5.12b and 5.12d). As the fence is moving toward the land, the difference of velocity at each location becomes larger. For instance, velocities at the end of the fence's domain reduce from about 0.8 m/s (blue circle) to 0.5 m/s (purple circle) for a slope of 1/500 (Figure 5.12c), while these values for a slope of 1/200 (Figure 5.12d) decrease by 0.15 m/s from about 0.77 m/s (blue circle) to 0.62 m/s (purple circle). Because all terms of drag form are proportional to $|u|^2$ (Equation 5.1), the decrease of u eventually leads to a reduction of total drag force.

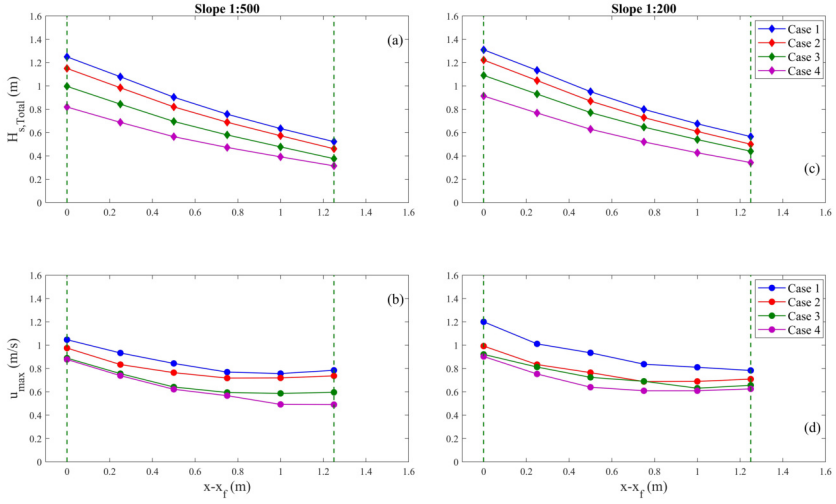

Figure 5.12: Comparison of significant wave heights (a, b) and maximum wave velocity (c, d) at all locations for slopes of 1/500 (left panel) and 1/200 (right panel).

Table 5.3 presents the maximum drag force (F_D), drag (F_d) and inertial ($F_i n$) forces of wooden fences at the seaward side of the fence for all fence locations and both slopes. Moreover, it shows the maximum force per branch, also at the seaward side of the fence ($F_{D,Branch}$), and the maximum total force on the entire fence ($F_{D,Fence}$). Generally, the maximum drag force (F_D) mainly depends on the drag term (F_d) while the inertial term (F_{in}) is significantly small compared to the drag term. In Table 5.3, the total F_D decreases with the increase of the fence's distance toward the sea for all slopes. For example, max-

imum F_D decreases from about 45.6 to 25.4 (kN/m^3) and from 54.0 to 29.5 (kN/m^3) for a slope of 1/500 and 1/200, respectively. At the same water depth and freeboard (same case), the maximum F_D of the fence on the gentler slope is smaller than on the steeper slopes. The steeper the slopes, the higher the velocity and drag force under the same wave conditions. Because the larger freeboard of a fence closer to the land leads to the less force of the fence, the total $F_{D,Fence}$ is also smaller than the further landward fence. In Table 5.3, the $F_{D,Fence}$ of submerged fences (case 1) reduced to almost half of maximum F_D to 24.4 and 28.8 (kN/m) for the slope of 1/500 and 1/200, respectively, while the $F_{D,Fence}$ of emerged fences slightly decreased for the largest freeboard (case 4). Additionally, the $F_{D,Branch}$ at the seaward side of the fence, give a suggestion for future design in choosing material and orientation of branches. The results also indicate that the lower force, especially for gentler slopes of 1/500, occurs at the wooden fences located closer to the land/mangrove. From this perspective, the wooden fence can create a favourable environment for mangroves on the leeward side by reducing the wave load on the front-line mangrove. It might lead to less damaged and to more healthy mangroves.

Table 5.3: Total drag force of wooden fences in different bottom slopes under the same wave conditions

Forces	Slope 1/500				Slope 1/200			
	Case 1	2	3	4	Case 1	2	3	4
Maximum F_D (kN/m^3)	45.6	38.8	28.6	25.4	54.0	37.7	34.3	29.5
Drag term F_d (kN/m^3)	44.5	37.8	27.8	24.6	52.8	36.7	33.3	28.6
Inerial term F_{in} (kN/m^3)	1.1	1.0	0.9	0.8	1.2	1.0	0.9	0.9
Total $F_{D,Fence}$ (kN/m)	24.3	20.7	18.3	20.4	28.8	20.1	21.9	23.6
$F_{D,Branch}$ (N/m)	75.6	64.3	47.5	42.2	89.5	62.4	56.8	48.9

5.3.3 Simulations for different scenarios on base slope

Wave transformation through fence and vegetation

The previous results show the significant wave height reduction of simulations with a fence only, creating a favourable area for mangrove resettlement. Next, the combination of a fence and mangrove area is simulated to observe wave dissipation by mangroves behind the fence. This combination simulation shows a difference in the incoming wave height at the seaward side, which is the most attacked and vulnerable side of the mangrove forest, and it confirms that the presence of a fence adds to the wave damping at the mangrove area. Figure 5.13 presents the reduction of significant wave heights due to mangroves (blue dashed line), a fence (solid black line), and in the case of a combination of fence and vegetation (solid red line). In Figure 5.13a and 5.13b, the total wave heights greatly reduce through the mangrove width (B_v = 50 m), which decrease from about 1.2 m to nearly 0.1 m (green dashed line). This result and several previous studies, e.g., Phan et al. (2019, 2014) indicate that vegetation can dissipate a large amount of wave energy within its width.

However, the front line of the mangroves, as much as the first 10 m, might be suffering from the direct wave attack, potentially resulting in a progressive destruction of the entire width of mangroves. With the installation of wooden fences in front of the mangroves, the mangroves now only has to dissipate about half of the incoming wave heights (solid blue line) compared to the case without a fence. For instance, the incoming wave height for cases without fences (green dashed line) is about 1.0 m, while it is about 0.44 m at $x_{f,1} = 100$ m (Figure 5.13a) and about 0.40 at $x_{f,2} = 235$ m (Figure 5.13b) for the case with fences (solid blue line). The higher pre-dissipation at the fence closer to the land produces the lower incoming waves for the mangroves. Even though there is a slight difference in incoming waves towards the mangroves between the two locations, wave heights are similarly dissipated to about 0.05 m by mangroves. The result indicates that the wooden fence creates a comfortable area for mangroves, and the closer fence produces the more favorable zone for mangrove/vegetation.

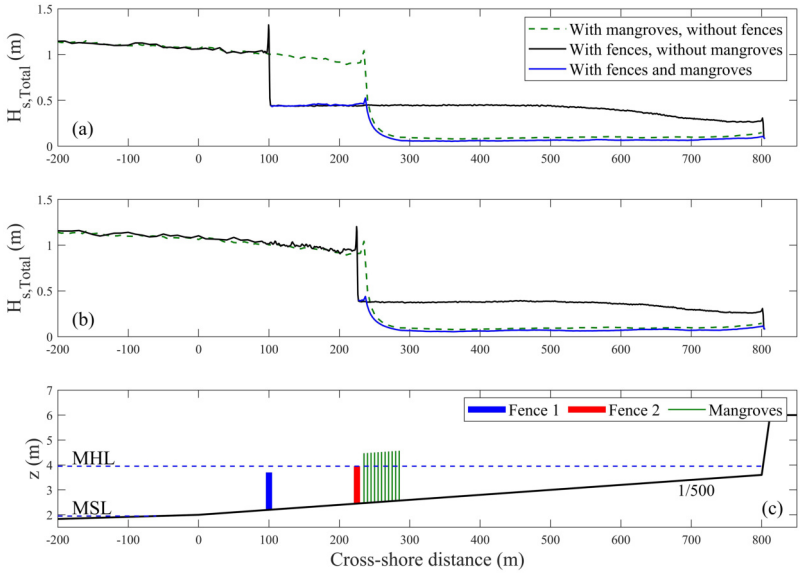

Figure 5.13: Wave transformation through mangroves only (green dashed line), through fence only (solid black line), and in a combination of fence and mangroves (solid blue line) at two locations $x_{f,1} = 100$ m (a) and $x_{f,2} = 235$ m (b). The profile with fences (thick blue and red line) and vegetation (solid green line) is in (c). Wave conditions are $H_s = 1.45$ m, $T_p = 9.4$ s, $d = 3.95$ m, $B = 1.2$ m, and $B_v = 50$ m.

Wave transformation over concave and convex profiles

In reality, the bottom slope has often evolved due to sediment transport, which is associated with the concave and convex scenarios. The concave profile normally is associated with situations of accretion, while the convex profile is related to erosion. Figure 5.14 presents the wave transformation through wooden fences at two locations, i.e.,

$x_{f,2}$ = 225 m and $x_{f,4}$ = 475 m (see Table 5.2), and on three different profiles, including concave (blue line), convex (green line) profiles, and a base slope 1/500 as a reference (black line). In Figure 5.14c, the concave and convex profiles are the ideal choice of the author from the observations in the field. As can be seen, both profiles highly influence pre-dissipation due to depth-induced breaking as well as wave damping by wooden fences. Obviously, the depth at the fence decreases on the concave profile but increases on the convex one. Between two locations, the pre-dissipation at the fence located closer to the land ($x_{f,2}$ = 225 m, Figure 5.14a) is much higher than at the more distant location ($x_{f,4}$ = 475 m, Figure 5.14b) on the concave profile (blue line). However, the pre-dissipation on the convex profile (green line) slightly reduces from the first to the second location. The transmission of waves is also influenced by the concave and convex profiles. At both fence locations, the transmitted wave heights are lower at the convex profile and higher at the concave profile as the depth at the fence is lower.

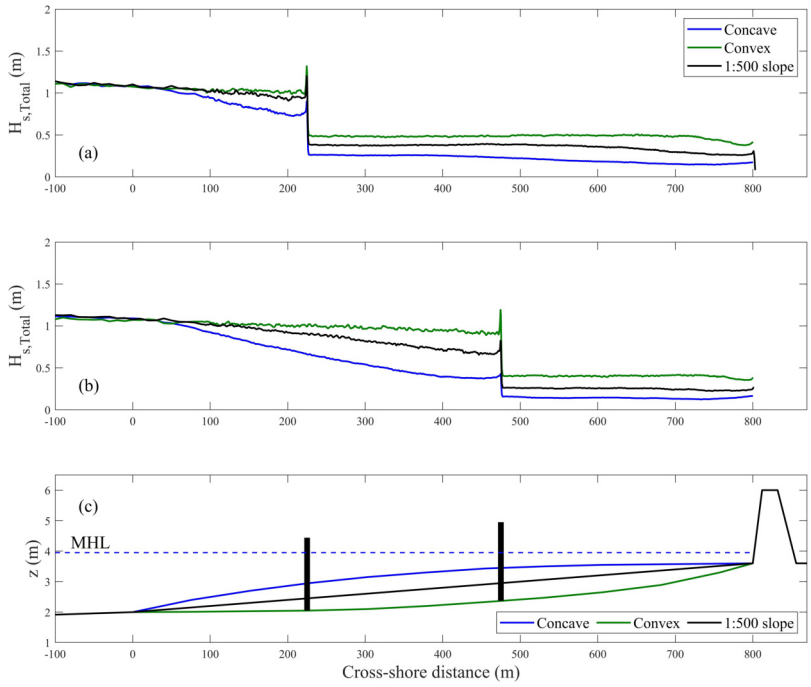

Figure 5.14: Wave transformation through the fences on concave (blue line) and convex (green line) profile. The base slope 1/500 is chosen for comparison.

The results suggest the use of wooden fences on either an erosion or nourishment coast. In the Mekong deltaic coast, some erosion coasts often have steeper slopes than coasts that have already been nourished. Even though a minimal pre-dissipation occurs between $x_{f,2}$ and $x_{f,4}$ on the convex profile (green line) as shown in Figure 5.14a and 5.14b, respectively, the fence ideally endures less wave load and promotes more sedi-

ment nourishment, based on the findings in the previous sections. Moreover, the wave transformation on the concave profile suggests a vital role of wooden fences in reducing wave heights, promoting sediments, and protecting mangroves or other intertidal vegetation species. In reality, the sediments probably increase after the installation of wooden fences. However, due to a lack of field measurements, future studies need to focus on this issue.

Wave transformation through fences with scours

During wave-fence interactions, scours at the fence's toes will eventually occur, which is simply a sediment transport at the upstream and the downstream sides of the fence. Thus, wave transformation through a fence with a scour that is simply a fixed bed is simulated in Figure 5.15. In reality, the brushwood inside the fence is always pulled down during wave-fence interaction resulting in a reduction of the brushwood elevation. Because the wooden fence is assumed to have a fixed height of 1.5 m, the fence can be assumed to sink with the scour depth without losing brushwood. As a result, the freeboard is increased with the increase in water depth. Figure 5.15c and 5.15d present the fence after sinking (thick blue line) and before sinking (dot line). It is noticed that the freeboard decreases with the scour depth. For example, the R_c value decreases from 0.55 to 0.25 m at $x_{f,1} = 100$ m (Figure 5.15c) and decreases from 0.35 to 0.05 m at $x_{f,4} = 475$ m (Figure 5.15d).

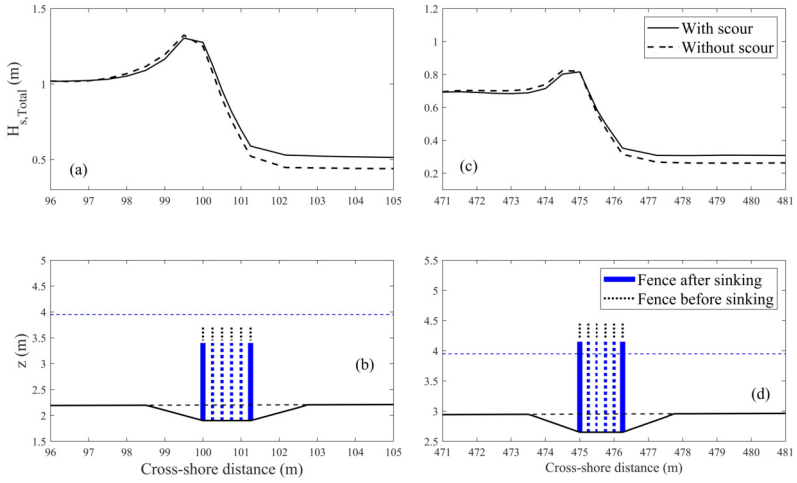

Figure 5.15: Wave transformation through wooden fences in cases with and without scour at $x_f = 100$ m (a) and $x_f = 475$ m (b) for the slope of 1/500. Profiles with (black solid line) and without scour (black dotted) are in (c) and (d).

Figure 5.15a and 5.15b present the wave transformation over wooden fences without (black dotted line) and with (black solid line) a scour at two locations. Generally, incoming wave heights at two locations seem to be similar, but the transmitted wave heights

($H_{s,t}$) in the case without scours are slightly lower than the case with scour. The increase of water depth in front of a wooden fence leads to a larger freeboard, resulting in the more overtopping and less transmission energy, for example, the $H_{s,t}$ decrease from 0.52 to 0.44 m at x = 103 m (Figure 5.15a) and from 0.30 to 0.26 m at x = 478 m (Figure 5.15b). It should be noted that this simulation simply focuses on the wave behavior between the case with and without scour and is not linked to sediment transport. Therefore, the result suggests that the effect of a wooden fence on damping waves will be reduced after a long-time use. The order of magnitude is 10% less wave reduction.

5.4 Conclusion

This study shows how the applied numerical wave model can be used in the practical design of brushwood fences. It investigates the effects of fence position and foreshore bathymetry (1:200 and 1:500 slopes) on wave damping due to wooden fences and forces on the fence using the characteristics from previous studies, e.g., Dao et al. (2020, 2018); Ngo et al. (2018); Thieu Quang and Mai Trong (2020).

Wave transformation through fences at several locations was simulated and analyzed. The results show that the bottom slopes significantly influence the pre-dissipation of incoming waves. The higher pre-dissipation occurs for wooden fences closer to the land, as the depth-limited wave height at the fence reduces. Moreover, the fence freeboard becomes larger for the fence located closer to the land, which increases its efficiency in wave damping. The higher HF- and LF-wave dissipation is found at the fence located closer to the land, especially on the gentler slope (1/500). The sediment transport, which corresponds to sediment stirring in front and settling behind the wooden fence, can also be linked to high- and low-frequency wave damping.

The effect of location and bottom slope on the forces on the wooden fences is also calculated. Among all locations, the total F_D at the offshore side are higher than the landside location for all slopes. The increase in total F_D is seen with the increase of wooden fence distance to the MSL due to the decrease of wave velocity. The results suggest that construction of wooden fences as close to the land/mangroves as possible, aids to reduce the wave load on the front-line mangroves. This idea is also shown by the result of a fence and mangroves combination, namely that the mangroves dissipate half of the incoming energy if wooden fences are installed in front of the mangrove area. It means that wooden fences reduce the wave load on the front-line mangroves and create a more favourable area for restoring mangrove growth.

The wave height damped by the fence is similar on both a steeper slope (1/200) and a gentler slope (1/500), except for the submerged fence. At the same water depth, the incoming HF- and LF-waves are dissipated more on the gentler slope than on the steeper slope. Furthermore, the maximum force on the fence on the steeper slope is higher than on, the gentler slope. As a result, the total force on the fence and the force on a branch are higher in steeper slopes.

In the field, wave-fence interaction can change the flow pattern, eventually leading to erosion at the fence's toe after a long period of time. As a result, the wave transmission might be higher and reduce the wooden fence's wave damping function. The wave transformation through a wooden fence with scour is a useful approach; yet the stability of the wooden fence and its lifetime duration need to be further investigated in the future. Finally, the wave damping through wooden fences on the concave profile is much lower than on the convex one. However, in reality, a concave profile often appears after installing wooden fences, therefore, the future study will need to consider this issue.

References

Albers, T., San, D. C., and Schmitt, K. (2013). Shoreline Management Guidelines: Coastal Protection in the Lower Mekong Delta. 1:1–124.

Alongi, D. M. (2008). Mangrove forests: resilience, protection from tsunamis, and responses to global climate change. *Estuarine, Coastal and Shelf Science*, 76(1):1–13.

Baldock, T. E., Manoonvoravong, P., and Pham, K. S. (2010). Sediment transport and beach morphodynamics induced by free long waves, bound long waves and wave groups. *Coastal Engineering*, 57(10):898–916.

Booij, N., Holthuijsen, L. H., and Ris, R. C. (1997). The" SWAN" wave model for shallow water. In *Coastal Engineering 1996*, pages 668–676.

Booij, N., Ris, R. C., and Holthuijsen, L. H. (1999). A third-generation wave model for coastal regions: 1. Model description and validation. *Journal of geophysical research: Oceans*, 104(C4):7649–7666.

Christensen, S. M., Tarp, P., and Hjortso, C. N. (2008). Mangrove forest management planning in coastal buffer and conservation zones, Vietnam: A multimethodological approach incorporating multiple stakeholders. *Ocean and Coastal Management*, 51(10):712–726.

Dao, H. T., Hofland, B., Stive, M. J. F., and Mai, T. (2020). Experimental Assessment of the Flow Resistance of Coastal Wooden Fences.

Dao, T., Stive, M. J. F., Hofland, B., and Mai, T. (2018). Wave Damping due to Wooden Fences along Mangrove Coasts. *Journal of Coastal Research*, 34:1317–1327.

Duke, N., Wilson, N., Mackenzie, J., Nguyen, H. H., and Puller, D. (2010). Assessment of Mangrove Forests, shoreline condition and feasibility for REDD in Kien Giang Province, Vietnam. *Deutsche Gesellschaft für Internationale Zusammenarbeit (GiZ) GmbH Management of Natural Resources in the Coastal Zone of Soc Trang Province*, pages 1–128.

Gagliano, S. M. and McIntire, W. G. (1968). Reports on the Mekong river Delta. Technical report.

Hong, P. N. and San, H. T. (1993). *Mangroves of Vietnam*, volume 7. Iucn.

Joffre, O. M. and Schmitt, K. (2010). Community livelihood and patterns of natural resources uses in the shrimp-farm impacted Mekong Delta. *Aquaculture Research*, 41(12):1855–1866.

K G, P. and Bhaskaran, P. K. (2017). Wave attenuation in presence of mangroves: A sensitivity study for varying bottom slopes. *The International Journal of Ocean and Climate Systems*, 8(3):126–134.

Ngo, A., Mai, T., and Mai, C. (2018). Wave reduction by a bamboo fence. In *International Symposium on Lowland Technology (ISLT 2018)*, Hanoi, Vietnam.

Nguyen, H.-H., McAlpine, C., Pullar, D., Johansen, K., and Duke, N. C. (2013). The relationship of spatial–temporal changes in fringe mangrove extent and adjacent land-use: Case study of Kien Giang coast, Vietnam. *Ocean & coastal management*, 76:12–22.

Phan, K. L., Stive, M. J. F., Zijlema, M., Truong, H. S., and Aarninkhof, S. G. J. (2019). The effects of wave non-linearity on wave attenuation by vegetation. *Coastal Engineering*, 147:63–74.

Phan, L. K. (2019). *Wave attenuation in coastal mangroves: Mangrove squeeze in the mekong delta*. Doctoral thesis, Delft University of Technology.

Phan, L. K., van Thiel de Vries, J. S. M., and Stive, M. J. F. (2014). Coastal Mangrove Squeeze in the Mekong Delta. *Journal of Coastal Research*, pages 233–243.

Read, L. K. and Vogel, R. M. (2015). Reliability, return periods, and risk under nonstationarity. *Water Resources Research*, 51(8):6381–6398.

Schmitt, K., Albers, T., Pham, T. T., and Dinh, S. C. (2013). Site-specific and integrated adaptation to climate change in the coastal mangrove zone of Soc Trang Province, Viet Nam. *Journal of Coastal Conservation*, 17(3):545–558.

Schoonees, T., Gijón Mancheño, A., Scheres, B., Bouma, T. J., Silva, R., Schlurmann, T., and Schüttrumpf, H. (2019). Hard Structures for Coastal Protection, Towards Greener Designs. *Estuaries and Coasts*, 42(7):1709–1729.

Sumer, B. M. (2002). *The mechanics of scour in the marine environment*. World Scientific.

Suzuki, T., Hu, Z., Kumada, K., Phan, L. K., and Zijlema, M. (2019). Non-hydrostatic modeling of drag, inertia and porous effects in wave propagation over dense vegetation fields. *Coastal Engineering*.

Tas, S. (2016). *Coastal protection in the Mekong Delta: Wave load and overtopping of sea dikes as function of their location in the cross-section, for different foreshore geometries*. PhD thesis, Delft University of Technology.

Thieu Quang, T. and Mai Trong, L. (2020). Monsoon wave transmission at bamboo fences protecting mangroves in the lower mekong delta. *Applied Ocean Research*, 101:102259.

Tran, V. L., Nguyen, D. B., and Nguyen, V. T. (2004). On the wind pressure zone map of the Vietnam territory. In *Workshop on Regional Harmonization of Wind Loading and Wind environmental Specifications in Asia-Pacific Economies (APEC-WW)*, pages 1–7, Tokyo. Tokyo Polytechnic University.

Van Cuong, C., Brown, S., To, H. H., and Hockings, M. (2015). Using Melaleuca fences as soft coastal engineering for mangrove restoration in Kien Giang, Vietnam. *Ecological Engineering*, 81:256–265.

Wolanski, E., Huan, N. N., Nhan, N. H., and Thuy, N. N. (1996). Fine-sediment dynamics in the Mekong River estuary, Vietnam. *Estuarine, Coastal and Shelf Science*, 43(5):565–582.

Zijlema, M., Stelling, G., and Smit, P. (2011). SWASH: An operational public domain code for simulating wave fields and rapidly varied flows in coastal waters. *Coastal Engineering*, 58(10):992–1012.

Chapter 6

Conclusion and recommendations

The journey is never ending. There's always gonna be growth, improvement, adversity...

Antonio Brown

This final chapter aims to assist in better understanding the resistance of wooden fences under the wave and flow actions. Firstly, the experimental bulk drag and Forchheimer coefficients, representing the resistance parameters of the wooden fence, are carried out in the Hydraulic Engineering Laboratory at Delft University of Technology (Chapter 2). Next, the numerical model is validated with the measurement data from a 1D physical model in the same laboratory (Chapter 3). The further understanding of the possible scale-effect of wave-fence interactions was also investigated based on the findings of the bulk drag coefficient of wooden fences (Chapter 4). Finally, the knowledge gained from previous findings was applied to the real bathymetry for the purpose of practical application (Chapter 5). The following sections present the answers to the research questions and observe several remarkable findings in this research.

6.1 Flow resistance of wooden fences

The concept of 'volume average' for a porous structure made of granular material, such as gravel, coarse sand, or fine sand, has been commonly applied to describe the form of hydraulic gradient that is to calculate the friction term under viscous and turbulent flow by Darcy-Forchheimer equations. This concept's understanding was then applied in both model- and full-scale wooden fences formed by bamboo cylinders into an inhomogeneous and staggered arrangement. The flow resistance of the wooden fence was obtained by determining the pressure gradient over a sample under stationary flows.

The pressure gradient observation gives the first impression of how a wooden fence can resist the hydraulic forces. In each fence sample, including both the model- and the full-scale, the pressure gradient increases with the increase of flow velocities represented by the flow conditions, i.e., viscosity and turbulent flows. The pressure gradient can be translated into resistance coefficients, including the bulk drag $\overline{C_D}$ and Forchheimer (β) coefficients, by applying the Darcy-Forchheimer equations. Besides the Reynolds number, as the common influencing and flow-dependency parameter, two more parameters particularly impact the bulk drag coefficient, such as the ratio of the gap between cylinders and the diameter (s/D) and the porosity (n). The bulk drag coefficient decreases with the increase of Reynolds numbers from 150 to 1000 and becomes stable at a Reynolds number above 1000. Moreover, the bulk drag coefficient decreases with reducing the s/D values directly linked to the porosity. As a result, the lowest porosity fence has the smallest bulk drag coefficient values.

The bulk drag and Forchheimer coefficient can be linked together by applying Forchheimer's law and Ergun's equation since they have acted similarly during different flow conditions. As a result, a new method for shifting between two coefficients is advised in future use. Thus, the use of the bulk drag coefficient is most effective for an array of cylinders, while the Forchheimer coefficient is applied for rock and soil materials. In reality, the wooden fences have an inhomogeneous arrangement, usually causing the space between bamboo branches to be irregular, leading to an unpredictable flow reduction inside the structure. Thus, the link between the bulk drag and the Forchheimer coefficient for a high Reynolds number, high turbulence flow is determined to be $\overline{C_D} = \beta\pi/2n$.

6.2 Numerical application for wave-fences interaction

The consideration of using a numerical model in studying wave dissipation over an array of cylinders mimicking vegetation or mangroves has been widely applied. For most numerical modelling studies, the parameters commonly required in numerical modelling are the diameter, density (porosity), and bulk drag coefficient. The bulk drag coefficient characterizes the flow; wave resistance is always dependent on the cylinder arrangement in a group in addition to porosity and diameter. For a random configuration, similar to brushwood fences, the bulk drag coefficient is even more important for the numerical model, independent of cylinder configuration.

With the bulk drag coefficient obtained from the previous experiments, an empirical model from Mendez and Losada (2004) and Suzuki et al. (2019) in the non-hydrostatic free-surface model SWASH is validated by using the data from physical model results. The validation results show a good agreement with the physical results without model calibration or fine-tuning, indicating that the bulk coefficient is the key parameter to simulate wave damping due to the wooden fence in the SWASH model.

The wave-fence interaction, expressed by the reflection, dissipation, and transmission coefficients, is then confidently studied in the SWASH model with staggered fences for both model- and full-scale. Firstly, the scale effect occurs between two scales, even though the Froude scale factor of 5.0 is relatively smaller than the scale suggested in the literature. The reflection and transmission coefficient of the model-scale is 0.05 lower than the full-scale results occurring at the relative fence thickness (B/H_I) below 5.5. The scale effect decreases with the increase of fence thickness and the increase of wave conditions, including wave height, peak wave period, and water depth. Besides the scale effect, the water depth and the incoming wave height of the model-scale should be larger than 0.3 m and 0.15 m, respectively, to disregard the effects of bed friction and viscosity inside the fence. Furthermore, the transmission coefficient is dependent on the dimensionless parameter, H_I/d and B/H_I, which indicates by the decrease of transmission coefficient with the increase of the B/H_I for $H_i/d > 0.3$. Meanwhile, the reflection coefficient is around 0.4 to 0.5 for all groups of H_I/d and B/H_I. The simulation results of transmission and reflection are also in the same range as the literature findings.

6.3 Wave non-linearity and wooden fence function

In the mangrove forest coasts, particularly along the Mekong deltaic coasts, wooden fences have been applied for mangrove restoration by reducing wave energy and by increasing the sedimentation rate. The fences of Melaleuca species and bamboo, installed in Kien Giang and Soc Trang province, showed a result of about 50% to 70% wave height reduction over the fences (Albers et al., 2013; Schmitt et al., 2013; Van Cuong et al., 2015). Their findings suggest that the freeboard (the height of the crest of a brushwood fence above or below still water level) is the prime parameter influencing wave reduction due to fences, translating it into the transmission coefficient. However, the degree of wave non-linearity, as represented by the Ursell number, as well as non-dimensional fence

thickness, becomes an important parameter to describe fence-induced wave reduction.

The relation between the Ursell number and the transmission coefficient is numerically investigated by the SWASH model. With the increase of relative fence thickness (B/L_p with L_p is the peak wavelength) from 0.15 to 0.32, the transmission coefficient decreases with the increase of the Ursell number. The more dense the fence thickness and the higher the Ursell number, the greater the wave reduction. In comparison with earlier literature, a lower wave reduction is mostly found when a lower freeboard as presented in the case of the submerged condition of the wooden fences relating to lower Ursell number. It is noted that the submerged condition is due to higher water depths than the fence heights resulting in the lower Ursell number. The decrease of water depth leads to the increase of the Ursell number and, thus, the higher wave reduction, leading to the proof that the highest wave reduction is found at higher freeboards.

6.4 Synthesis

The understanding of wave damping due to wooden fences in the full-scale is finally evaluated in the bathymetry found in the Mekong deltaic coasts. The practical design of brushwood fences, including fence positions and foreshore slope of 1/200 and 1/500, is considered in the SWASH model. Firstly, the wave transformation through fences at several locations showed the influences of bottom slopes in dissipating incoming waves, the so-called pre-dissipation. A higher pre-dissipation is found for a wooden fence closer to the land, as the depth-limited wave height at the fence is reduced. The pre-dissipation of high- and low-frequency waves is highly influenced by the bottom slopes, especially on the 1:500 slope. The sediment transport, which relates to sediment stirring in front and settling behind the wooden fence, also corresponded with high- and low-frequency waves.

Moreover, the fence locations and bottom slopes also affected the drag force caused by a wooden fence. The higher force from a wooden fence was found at the offshore location than at the nearshore one. The suggestion of constructing wooden fences closer to the land/mangroves should be taken into account due to the possible reduction of wave load from the wooden fences on the front-line mangroves. As a result, a more favourable area for restoring mangroves can be created by building brushwood fences, as proven by the consideration of fence-mangroves simulations.

At the same water depth, the wave damping by a fence is found similarly on both a steeper slope (1/200) and a gentler slope (1/500) for most of the emerged cases. The pre-dissipation of both high- and low-frequency waves is also higher on the steeper slope (1/200) than on the gentler slope (1/500). As a result, the high- and low-frequency waves are reduced more on the gentler slope than on the steeper slope. The drag forces, including the total force and the force per branch, created by the fence are found higher on the steeper slope than on the gentler slope.

Several considerations, such as the damping function of a fence reduced by the scouring and the concave and convex profile, are concerned in the practical engineering aspect. The reduction of wave damping through a wooden fence with scour shows the concern of the stability of the wooden fence and its lifetime duration. Moreover, the wave damping by wooden fences on the convex profile is much higher than on the concave one introducing sediment transport as before and after installing the wooden fence.

6.5 Recommendations

At the conclusion of this dissertation, it is noticed that certain knowledge gaps still remain. The full-scale simulation regarding stirred and suspended sediments due to wood fences remains the most challenging research question, yet, it is also essential to continue the application sequel for the restoration and the health of the mangroves. Indeed, there are several recommendations in regard to the future work:

- The bulk drag coefficient can be shifted to the Forchheimer coefficient in order to replace brushwood with other materials, such as rocks or stones, inside a wooden fence. The future study should carry out this replacement to optimistic design as well as increase the lifetime duration of a wooden fence;
- Several empirical design for wooden fence should be considered such as the optimistic thicknesses and heights. Moreover, the setting of horizontal branches formed the inner parts should be taken into account with the optimistic porosity/density as well as branch arrangements.
- A 2D/3D numerical simulation, validated with field and/or laboratory measurements linking wave conditions and sediment transports through wooden fences, should be taken into account.

Acknowledgements

Doing a PhD in the Netherlands is an unforgettable journey that I cannot walk alone in the entire time. Thankfully, I always have family members, friends, supervisors, and colleagues who support me all along.

First and foremost, I am extremely grateful to my promotor, Marcel Stive, who accepted my scholarship and assisted me in coming to TU Delft and Netherlands. He is such a brilliant promotor who gives the first and ultimate idea for my thesis. He gives me time to adapt to the new culture, education environment in TU Delft and slowly guides me so that I can gain the needed knowledge to moving toward the end. He is such a great friend who always cares and supports me within his ability.

Secondly, I would like to express my sincere gratitude to Bas Hofland for his most valuable assistance and contribution to my research. He is a truly brilliant guy who always pump up new ideas to help me filling up knowledge gaps. We sometime have unnecessary argument but his knowledge, criticism, and enthusiasm always encourage me to try doing the best for my research.

Next, I would like to send my appreciation to all committee members. I want to extend my sincere thanks to Tomohiro Suzuki and Mai Cao Tri for their technical supports, insightful comments, and suggestions for my research. I also want to thank Le Xuan Tuan for his mental support and contribution to the final stage of my thesis. I want to offer my special thank to Sander De Vree, Jaap van Duin, Frank Kalkman, and Anno Doorn for their incredible support during my experiments in the Hydraulic Engineering Laboratory. I am also grateful to Mariette van Tilburg for her assistance of proof-readers to my article and thesis. I am deeply grateful to Inge van Rooij for her assistance, support and joyful moments during my Ph.D. time. I want to thank all assistants in VIED and HUNRE who support my current job in Vietnam and finance for living in the Netherlands.

I want to thank Anastasia Yunika for her regard during my Ph.D. time. And I am grateful to have Duoc as a good friend who shared with me many experiences and grateful memories during my stay in the Netherlands. I would like offer my grateful attitude to Marjan Kreijns, Lindsey Schwidder, Juliette Eulderink for spending cheerful moments with me. And a special thank to Veronique van de Vast for her mentally and finacially support.

I want to express my special thanks to all my friends and foes for their insightful comments, and financial support during my Ph.D. time. Finally, I am extremely grateful to my parents who encourage me to do a Ph.D. abroad, my wife who is always cheerful, and my daughter who once again make me how nice of being a child. And their supports make me be a better son, husband, and father.

Delft, 2021
Hoàng Tùng Dào

Curriculum Vitæ

Hoàng Tùng DÀO

05-10-1988	Born in Hanoi, Vietnam.

Education

2006 – 2011	B. Sc. Coastal Engineering Thuy Loi University, Vietnam
Thesis:	Research on estuary sedimentation of My A estuary, Quang Ngai province, Vietnam and design construction solutions
2011 – 2013	M. Sc. Coastal Engineering Thuy Loi University, Vietnam
Thesis:	Research on sedimentation phenomenon of Sa Huynh estruary, Quang Ngai province, Vienam and recommend solutions
2016 – 2021	PhD. Coastal Engineering Delft University of Technology
Thesis:	Hydraulic performance of brushwood fences for mangrove replantation in the Mekong Delta
Promotor:	Prof.dr.ir M.J.F. Stive
Co-promotor:	Dr.ir. B. Hofland

Professional Training

2017	NCK Summer School: Estuarine and Coastal Processes in realation to Coastal Zone Management
2018	PAO - Techniek en Management, TU Delft: SWASH model
2018	Deltares Academy: Delft3D Flexible Mesh - Coastal Morphodynamic Modelling
2018	DelftX Program: Building with Nature
2019	DelftX Program: Introduction to Water and Climate

Awards

2015	Fellowship by Vietnam International Education Development (VIED) Ministry of Education and Training, Vietnam
2020	Editor's Choice Article in Water 2020: "Experimental Assessment of the Flow Resistance of Coastal Wooden Fences"

List of Publications

1. **Dao, T.**,Stive, M.J.F, Hofland, B. and Mai, T.,. Wave damping due to wooden fences along mangrove coasts, *Journal of Coastal Research*, 34(6), pp.1317-1327, 2018.

2. **Dao, H.T.**, Hofland, B., Stive, M.J.F., and Mai, T., Experimental assessment of the flow resistance of coastal wooden fences, *Water*, 12(7),p 1910, 2020, Editor's choice.

3. **Dao, H.T.**, Hofland, B., Suzuki T., Stive, M.J.F., Mai, T. and Le T.X., Numerical and small-scale physical modelling of wave transmission by wooden fences, *Journal of Coastal and Hydraulic Structures*, 1, 2021.

4. **Dao, H.T.**, Hofland, B., Stive, M.J.F., Mai, T. and Ngo A., Design consideration for brushwood fences concerning bathymetry and fence locations, *Vietnam Symposium on Advances in Offshore Engineering conference*, accepted, 2021.

5. Stive, M.J.F., Phan, L.K., Truong, S.H., Phan, H.M. and **Dao, H.T.**, Innovative Vietnamese Research on Mekong Deltaic Coastal Processes, *International Conference on Asian and Pacific Coasts*, pp. 1377-1381, 2019, Springer, Singapore.

6. Mai, T., **Dao, T.**, Ngo, A. and Mai, C., Porosity Effects on Wave Transmission Through a Bamboo Fence, *International Conference on Asian and Pacific Coasts*, pp. 1413-1418, 2019, Springer, Singapore.

7. Mai, T., Nguyen, V., Ho, D., Ngo, A., **Dao, T.**, Numerical simulation of wave transmitting through a bamboo fence, *Tap Chi Khoa Hoc Cong Nghe Xay Dung (KHCNXD) - ĐHXD*, 13(1V), 75-83, 2019

8. Stive, M.J.F., Phan L.K., Truong S.H, Phan H.M., **Dao, H.T.**, and Silke T., Mekong mangroves: Science, Engineering and Management.

About the author

Hoàng Tùng Dào was born on the 5 October, 1988, in Hanoi, Vietnam. At his 15 years, he helped cooking, delivering and being a bartender at his family business during studying in high school. In 2006, he went to Thuy Loi University (named once Water Resources University) in Coastal Engineering. In 2011, he graduated and started to work as a cashier and manager in a book store in Hanoi in a half year before attempting to a master programme in Thuy Loi University in Coastal Engineering. He continued to work there as a part-time job during the master program. In 2013, he graduated from the master program and started to work in a private construction company.

In 2014, he moved to work as a lecturer at Hanoi University of Natural Resources and Environment (HUNRE) after the faculty of Marine Science and Island was found. He taught General Oceanography and many subjects related to what he had learnt. In late 2015, he earned the fellowship for high education funded by Vietnam International Education Development (VIED), Ministry of Education and Training, Vietnam, and immediately applied to Delft University of Technology, the Netherlands.

In over five years studying as PhD in TU Delft, under the guidance of promotor Prof. M. J. F. Stive and co-promotor Dr. B. Hofland, he managed to earn a PhD degree including many achievements in skills and educational training. He published three journal publications, especially, his second paper had earned the Editor's choice title for a publication in Journal of Water, 2020. Besides all credits and skills learnt from TU Delft programs, he successfully finished the special DelftX programs, including two courses: Building with Nature and Introduction to Water and Climate from 2018 to 2019. Also, in 2018, he participated the Deltares programs for the SWASH model and Delft3D flexible meshes. Last but not least, he has many experiences in collecting/recording and analysing data and has particular knowledge of laboratory equipment.